

Control of coupled transport in Tokamak plasmas

Bojan Mavkov

▶ **To cite this version:**

Bojan Mavkov. Control of coupled transport in Tokamak plasmas. Automatic. Université Grenoble Alpes, 2017. English. NNT : 2017GREAT004 . tel-01483998v2

HAL Id: tel-01483998

https://theses.hal.science/tel-01483998v2

Submitted on 14 Nov 2017

HAL is a multi-disciplinary open access archive for the deposit and dissemination of scientific research documents, whether they are published or not. The documents may come from teaching and research institutions in France or abroad, or from public or private research centers.

L'archive ouverte pluridisciplinaire **HAL**, est destinée au dépôt et à la diffusion de documents scientifiques de niveau recherche, publiés ou non, émanant des établissements d'enseignement et de recherche français ou étrangers, des laboratoires publics ou privés.

Communauté
UNIVERSITÉ Grenoble Alpes

THÈSE

pour obtenir le grade de

DOCTEUR DE LA COMMUNAUTÉ UNIVERSITÉ GRENOBLE ALPES

Spécialité : **Automatique et Productique**

Arrêté ministériel : 7 août 2006

Présentée par
Bojan MAVKOV

Thèse dirigée par **Christophe PRIEUR** et
Emmanuel WITRANT
préparée au sein du laboratoire
GIPSA-Lab,
dans **l'école doctorale Electronique, Electrotechnique, Automatique, Traitement du Signal (EEATS)**

Control of Coupled Transport in Tokamak Plasmas

Thèse soutenue publiquement le **24 janvier 2017**,
devant le jury composé de:

Mazen ALAMIR
Directeur de Recherche CNRS, Université Grenoble Alpes, Examinateur, Président du jury
Olivier SAUTER
Maître d'enseignement et de recherche, Ecole Polytechnique Fédérale de Lausanne, Rapporteur
Laurent AUTRIQUE
Professeur, Université d'Angers, Rapporteur
Eduardo CERPA
Professeur associé, Universidad Técnica Federico Santa María, Examinateur
Christophe PRIEUR
Directeur de Recherche CNRS, Université Grenoble Alpes, Directeur de thèse
Emmanuel WITRANT
Maître de conférences, Université Grenoble Alpes, Directeur de thèse
Didier MOREAU
Ingénieur de Recherche HDR, CEA Cadarache, Invité
Federico BRIBIESCA ARGOMEDO
Maître de Conférences, INSA Lyon, Invité

Contents

Introduction **1**

Introduction **13**

1 Transport equations and control problem formulation **21**

1.1 Poloidal Magnetic Flux in a tokamak 23

1.2 Electron temperature equation 25

1.3 Model outputs 27

1.4 Model inputs 29

1.5 Control problem formulation 31

2 Linear models for control **33**

2.1 First-principle linearized model for control 34

2.2 Data-driven model for control 36

2.3 Subspace identification 44

2.4 Output-error identification 49

2.5 Identification results 52

2.6 Conclusion on the identification approach 56

2.7 Conclusion of the chapter 57

3 Distributed control of safety factor and electron temperature **61**

3.1 Stability analysis and control of the coupled system 63

3.2 System decoupling using singular perturbation theory 68

3.3 Composite control 70

3.4 Control implementation 73
3.5 Results 77
3.6 Conclusion of the chapter 83

4 Simultaneous control of the safety factor and the plasma β 87

4.1 Control problem and experimental settings 89
4.2 Distributed control 92
4.3 Control of β 96
4.4 Anti-windup implementation 97
4.5 Control implementation 100
4.6 Results from the simulations 100
4.7 Conclusion on the chapter 110

Conclusion 111

Bibliography 120

List of Figures

1 La vue intérieure de TCV (Tokamak à Configuration Variable) à l'École polytechnique fédérale de Lausanne 3

2 Représentation des bobines et champs magnétiques dans un tokamak . . . 4

3 Code rapide d'évolution du profil plasma RAPTOR. 12

4 The inner view of TCV in Swiss Plasma Centre 15

5 Representation of the coils and magnetic fields in a tokamak 16

1.1 Plasma coordinates and surface S_{pol} used to define the poloidal magnetic flux 23

1.2 Ohmic and external heating in tokamak 29

2.1 Cubic splines $a_k(x)$ used for the expansion of Ψ_r, and $b_k(x)$ used for the expansion of T_e. 38

2.2 Overview of the method. 42

2.3 First 10 singular values of Σ that indicate the order of the model. 47

2.4 Comparison between the measured values of the simulated system and the outputs of the identified system for the MOESP and the output-error methods for simulation # 22. 51

2.5 Plot of $\Psi_r(t)$ vs time for the simulation # 22. The black dashed traces represent the outputs of the simulation of the identified system and the red traces represent the outputs of the original METIS simulation. The fit parameter defined in (2.18) is indicated in each frame. 53

2.6 Plot of $T_e(t)$ vs time for the simulation # 22. The black dashed traces represent the outputs of the simulation of the identified system and the red traces represent the outputs of the original METIS simulation. The fit parameter defined in (2.18) is indicated in each frame. 54

2.7 Plot of $\Psi_r(t)$ vs time for the simulation # 19. The black dashed traces represent the outputs of the simulation of the identified system and the red traces represent the outputs of the original METIS simulation. The fit parameter defined in (2.18) is indicated in each frame. 55

2.8 Plot of $T_e(t)$ vs time for the simulation # 19. The black dashed traces represent the outputs of the simulation of the identified system and the red traces represent the outputs of the original METIS simulation. The fit parameter defined in (2.18) is indicated in each frame. 56

2.9 Plot of the four inputs (P and V_{ext}) and the total plasma current (I_p) vs time for simulation # 22. 57

2.10 Plot of the four inputs (P and V_{ext}) and the total plasma current (I_p) vs time for simulation # 19. 58

2.11 Plot of the inputs (P and V_{ext}) and the total plasma current (I_p) vs time for simulation # 20. 58

2.12 Plot of $T_e(t)$ vs time for the simulation # 20. The black dashed lines represent the outputs of the simulation of the identified system and the red traces represent the outputs of the original METIS simulation. The fit parameter defined in (2.18) is indicated in each frame. In this simulation at 11.6 s, the total power drops down to 2.5 MW. 59

2.13 Plot of $T_e(t)$ vs time for the simulation # 20. The black dashed lines represent the outputs of the simulation of the identified system and the red traces represent the outputs of the original METIS simulation. The fit parameter defined in (2.18) is indicated in each frame. At 11.6 s the total power drops down to 2.5 MW. 60

3.1 Normalized auxiliary electron cyclotron current-drive j_{dis} ($10^{20}\frac{m^{-5}A}{keVW}$) and Normalized auxiliary electron cyclotron power density Q_{dis} (m^{-3}) for the TCV configuration. 75

3.2 Normalized auxiliary electron cyclotron current-drive j_{dis} ($10^{20}\frac{m^{-5}A}{keVW}$) and Normalized auxiliary electron cyclotron power density Q_{dis} (m^{-3}) for the ITER configuration. 76

3.3 Numerical solution of $p_1(x)$ and $p_2(x)$ for TCV. 78

3.4 Time evolution of the normalized Lyapunov function in TCV simulations. . 78

3.5 Evolution of ι on the TCV simulation. A disturbance is added at $t = 0.3$. 79

3.6 Evolution of T_e on the TCV simulation. A disturbance is added at $t = 0.3$. 80

3.7 Comparison of the final values of ι and T_e obtained by open loop and using feedback control. 81

3.8 Evolution of the actual $j_{aux}(x,t)$ $[A/m^2]$ (top left) and $Q_{aux}(x,t)$ $[W/m^3]$ (top right) and $P_{aux}(t)$ (below) applied to the system in TCV. 82

3.9 Evolution ι (top) and T_e (bottom) in the ITER simulation with the coupled controller and with convergence priority given to $\tilde{z}$ (Case 1, small γ) or $\tilde{T}_e$ (Case 2, large γ). 83

3.10 Evolution of T_e and ι in the ITER simulation (control case 1). 84

3.11 Evolution of T_e and ι in the ITER simulation (control case 2). 84

3.12 Numerical solution of p_s and $p_f(x)$. 85

3.13 Time evolution of the two normalized Lyapunov functions V_s and V_f. . . . 85

3.14 Evolution of the actual $j_{aux}(x,t)$ $[A/m^2]$ (top left) and $Q_{aux}(x,t)$ $[W/m^3]$ (top right) and $P_{aux}(t)$ (below) applied to the ITER configuration (Control case 1). 86

3.15 Evolution of the actual $j_{aux}(x,t)$ $[A/m^2]$ (top left) and $Q_{aux}(x,t)$ $[W/m^3]$ (top right) and $P_{aux}(t)$ (below) applied to the ITER confguration (Control case 2). 86

4.1 Fast control oriented plasma profile evolution code RAPTOR. 89

4.2 $\eta_{||}$ parameter ranges with the minimum value (red dash line) and the maximum value (blue dash line) 91

4.3 Comparison of the performance of the control of β without (blue dash line) and with (red line) the application of an anti-windup scheme. 99

4.4 Comparison of the performance of the control of ι with (blue dash line) and without (red line) the application of an anti-windup scheme. 99

4.5 Control scheme 101

4.6 Plot of the numerical solutions of the optimization problem presented in subsection 4.2.2 as polynomial functions $p_z(x), p_I(x), k_z(x)$ and $k_I(x)$ using an LMI solver. 102

4.7 Response of ι with a pure integrator (red line) compared with the response when a forgetting factor $\lambda(t)$ is added to the integral action (blue dashed line) at several discretized locations. 103

4.8 ι tracking evolution is presence of a time delay in the feedback loop. 104

4.9 β tracking evolution with a time delay in the feedback loop. 105

4.10 ι tracking with changed deposition location and width for P_{ec2}. 106

4.11 β tracking with changed deposition location and width for P_{ec2}. 106

4.12 Applied ECCD power evolution with changed deposition location and width for P_{ec2}. 107

4.13 ι profile evolution with external disturbance added with $\omega_{dep} = 0.4$ and $x_{dep} = 0.2$. 108

4.14 β evolution with added external disturbance at $t = 0.4\ s$. 109

4.15 Applied ECCD power evolution with added external disturbance at $t = 0.4\ s$.109

List of Tables

1.1 Most relevant physical variables and units 22

2.1 Table of the nonlinear METIS simulations used for the system identification showing the minimum and maximum values of the square-wave modulated inputs 52

Résumé détaillé en français

Fusion Thermonucléaire

Les réactions de fusion sont des réactions énergétiques élevées dans lesquelles deux noyaux atomiques légers se fusionne pour former un noyau plus lourd. La réaction de fusion nucléaire alimente le Soleil et les étoiles, émettant une grande quantité de rayonnement. La forme énergétique du Soleil est disponible dans la Terre directement à partir de la lumière du soleil et est indirectement convertie en différentes formes d'énergie, telles que l'énergie hydroélectrique, l'énergie du combustible, l'énergie éolienne, etc., qui sont d'importantes sources d'énergie dans la terre. L'augmentation de la demande énergétique et la forte dépendance vis-à-vis des combustibles fossiles rendent la situation énergétique actuelle insoutenable, et les recherches sur les nouvelles sources d'énergie renouvelables se multiplient. La fission nucléaire est utilisée comme source de production d'électricité depuis de nombreuses années. Mais ce type d'énergie est lié à un risque élevé de stabilité des centrales nucléaires et des déchets nucléaires dangereux pour l'environnement. Dans la recherche de sources d'énergie propres et sûres, un grand effort a été consacré au développement de la fusion thermonucléaire contrôlée. L'énergie de fusion nucléaire contrôlée a le potentiel de fournir une énergie durable et suffisante, avec un impact relativement faible sur l'environnement. Cependant, la construction d'un réacteur de fusion nucléaire capable de maintenir la réaction de fusion et d'assurer la durabilité n'est pas une tâche simple. La réaction de fusion la plus prometteuse à l'énergie la plus basse est celle dans laquelle le noyau des atomes de Deutérium (D) et de Tritium (T) se fusionne en un seul Hélium (He) et un neutron (n) (Wesson and Campbell, 2011):

$$^{2}_{1}\mathrm{D} + ^{3}_{1}\mathrm{T} \rightarrow ^{4}_{2}\mathrm{He} + ^{1}_{0}\mathrm{n} + E \tag{1}$$

Où la fraction du déficit massif total (δm) est libérée sous forme d'énergie cinétique $E = \delta m c^2 = 17,6$ MeV. Le deutérium est l'un des deux isotopes stables de l'hydrogène et peut être facilement extrait de l' eau de tous les jours. Le tritium n'apparaît pas naturellement, mais il peut être produit dans des réacteurs nucléaires par activation neutronique du lithium, dont il existe de grandes réserves naturelles. Cela signifie qu'il existe des réserves de carburant facilement disponibles pour ce type de production d'énergie.
Pour atteindre une énergie de fusion thermonucléaire, il doit y avoir une quantité suffisante d'énergie pour obtenir la réaction (1). Pour surmonter la barrière coulombienne (répulsion mutuelle des particules), les noyaux chargés positivement du combustible nucléaire doivent être suffisamment chaud. A ces températures, tous les atomes sont ionisés, créant des particules positives et négatives non liées appelées plasma. Dans les réacteurs à fusion, le

plasma est chauffé pour maintenir le processus de fusion: on parle d'ignition. Les exigences d'ignition ont été présentées formellement par le critère de Lawson (Lawson, 1957). Le seul paramètre du critère utilisé pour la mesure de l'efficacité du réacteur de fusion de densité (n), de température (T) et de temps de confinement d'énergie (τ_E) est présenté par le triple produit $nT\tau_E \geq 31021 m^{-3} keV s$. Cela implique que les combustibles doivent être chauffés à des températures extrêmes pour que ce critère dépasse la valeur critique nécessaire pour enflammer le plasma.

Tokamaks

Les Tokamaks sont de grand appareils utilisant le champ magnétique pour confiner et chauffer le plasma sous la forme d'un tore. Le but de la recherche sur les tokamaks est de construire un système de production d'électricité fiable utilisant la fusion thermonucléaire (Wesson and Campbell, 2011). Le Tokamak est le concept de réacteur qui a atteint la valeur la plus élevée de $nT\tau_E$ et est considéré, avec le stellarator, comme l'une des sources les plus prometteuses d'énergie de fusion durable. Le design des Tokamaks a été inspiré par l'idée d'Oleg Lavrentiev et a été développé dans les années 1950 par les physiciens soviétiques Igor Tamm et Andrei Sakharov. Le nom de tokamak vient de l'acronyme russe "ТОроидальная КАмера с МАгнитными Катушками " (toroidal'naya kamera s magnitnymi katushkami) qui signifie la chambre toroïdale avec des bobines magnétiques. Il existe de nombreux tokamaks à travers le monde, comme JET, MAST, Tore supra, DIII-D, JT-60U ou TCV (Fig. 1). Les expériences réalisées à l'aide de ces tokamaks ont fait des progrès significatifs afin d'atteindre l'objectif de l'énergie de fusion. Le réacteur thermonucléaire expérimental international (ITER) est le principal projet de recherche qui vise à prouver la faisabilité de la fusion thermonucléaire. Ce projet est en cours de construction à Cadarache, en France, et devrait présenter la transition des études expérimentales de la physique des plasmas aux centrales à fusion capables de produire de l'énergie durable. Le courant de plasma, qui contribue au chauffage du plasma et génère le champ magnétique poloïdal, est principalement intronisé par la bobine de chauffage ohmique. Le champ magnétique toroïdal B_ϕ, est produit par les bobines de champ toroïdal et le champ poloidal B_ψ est produit par les courants à l'intérieur du plasma. Des courants non inductifs supplémentaires et le chauffage au plasma sont obtenus par l'injection de particules neutres à haute énergie et d'ondes électromagnétiques. Parmi les systèmes de commande de chauffage et de courant les plus couramment utilisés, on trouve l'injection de faisceau neutre, le chauffage par résonance cyclotronique électronique ou le variateur de courant, le chauffage par résonance cyclotronique ionique, Ondes et un variateur hybride inférieur. Un diagramme schématique du champ magnétique principal et de la configuration du courant dans un tokamak est représenté sur la Fig. 2.

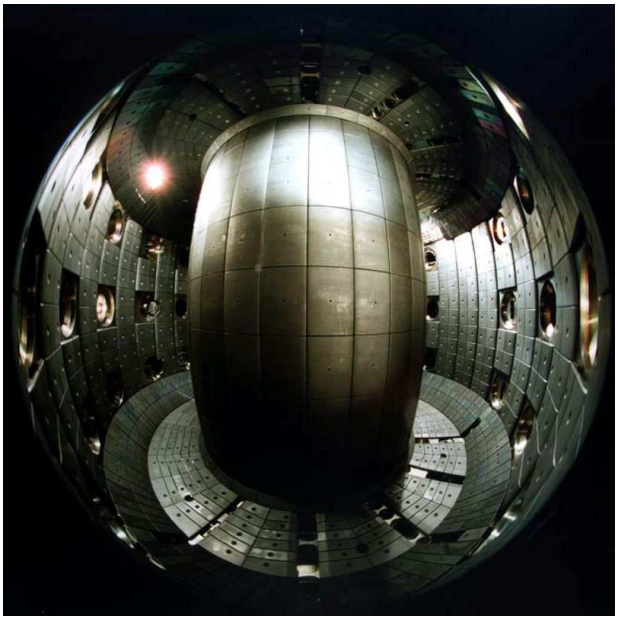


Figure 1: La vue intérieure de TCV (Tokamak à Configuration Variable) à l'École polytechnique fédérale de Lausanne

Formulation du problème et travaux antérieurs

L'un des principaux défis dans le contrôle du plasma tokamak est de réaliser les scénarios d'état stationnaire dits tokamaks avancés qui joueront un rôle important puisqu'ils permettront de reproduire et d'étudier les conditions qui devraient être obtenues dans une usine de fusion, de dimension et coûts réduits (Taylor, 1997). Les scénarios de tokamak avancés se caractérisent par un gain de fusion élevé, un bon confinement plasmatique et une stabilité MagnetoHydroDynamic (MHD) qui sont cruciaux pour la performance et la stabilité du plasma. Une combustion de fusion à haut gain pourrait être obtenue alors qu'une fraction majeure du courant plasmatique est autogénérée par l'effet néo-classique de bootstrap qui réduirait la quantité nécessaire de courant auxiliaire nécessaire pour maintenir le scénario souhaité (Gormezano et al., 2007). Les défis de contrôle sont généralement séparés en deux groupes: contrôle électromagnétique et contrôle cinétique. Les variables d'état apparaissent naturellement dans les évolutions du flux magnétique poloïdal interne qui étant étroitement lié au facteur de sécurité et d'un ensemble de variables fluides/cinétiques telles que la densité du plasma, la vitesse toroïdale et les températures des ions et des électrons. Le contrôle simultané en temps réel de plusieurs paramètres de plasma magnétique et cinétique distribués radialement est l'un des principaux défis dans le contrôle des scénarios de tokamaks avancés. Les profils magnétiques et cinétiques sont connus pour être fortement couplés, et les intégrer dans un seul contrôleur est particulièrement important pour les scénarios de tokamaks avancés dans les futurs dispositifs de fusion tels que l'ITER.

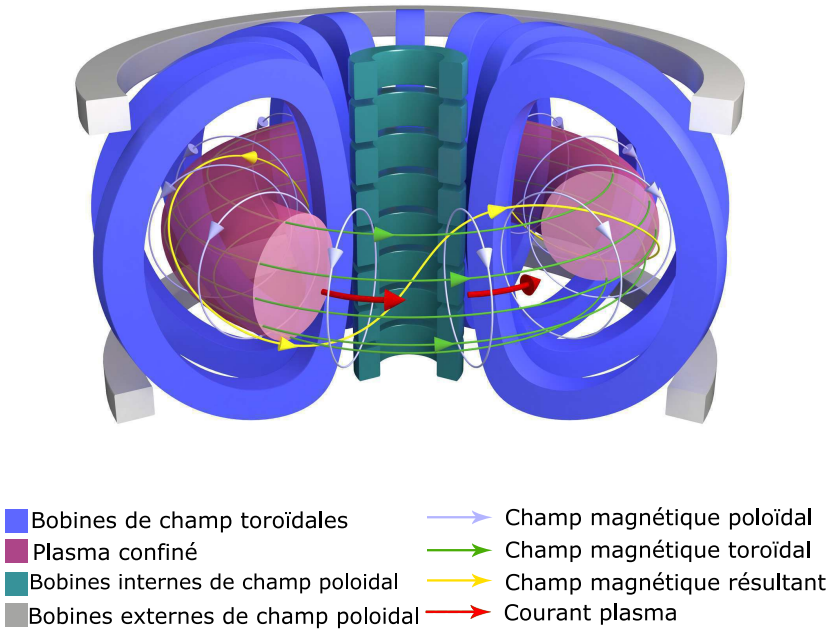


Figure 2: Représentation des bobines et champs magnétiques dans un tokamak

Le contrôle simultané en temps réel des paramètres du plasma magnétique et cinétique, tels que le courant et les profils de gradient de température électronique, a été réalisé pour la première fois au cours des campagnes expérimentales sur JET (Mazon et al., 2003; Laborde et al., 2004; Moreau et al., 2003). Dans ces travaux pionniers, le contrôleur est basé uniquement sur la réponse statique au plasma, et sur un algorithme qui minimise une somme pondérée d'erreurs intégrales à moindres carrés entre les profils demandés et ceux mesurés. Des stratégies de contrôle plus avancées sont développées après cela et appliquées à d'autres dispositifs tokamaks tels que Tore Supra, DIII-D et JT-60U. Les algorithmes de contrôle basés sur des modèles peuvent être développés en utilisant deux types de modèles de contrôle. Le premier est un modèle piloté par données extrait à l'aide de techniques d'identification. Ce modèle est obtenu en utilisant uniquement des données de mesures et des techniques d'identification de systèmes, de sorte que la connaissance exacte de la dynamique du système n'est pas nécessaire. Les algorithmes de contrôle pour le contrôle simultané des paramètres cinétiques couplés et du plasma magnétique, basés sur des modèles dynamiques basés sur des données plasmatiques à deux échelles, sont présentés dans (Moreau et al., 2008; Moreau et al., 2013; Moreau et al., 2011). Le second est un modèle

basé sur le principe premier onvertissant les lois physiques fondamentales qui régissent le comportement du plasma en un modèle de contrôle orienté approprié pour un design de contrôle. Ce modèle simplifie les modèles d'évolution des systèmes en considérant uniquement la physique dominante de la dynamique du plasma qui est pertinente pour l'objectif de contrôle (Witrant et al., 2007; Felici, 2011). Les modèles de contrôle sont basés sur les équations de transport physique qui régissent l'évolution des paramètres du plasma. Ces modèles ne sont pas faciles à obtenir car beaucoup des coefficients de transport ne sont pas bien connus. Pour cette raison, certains modèles empiriques sont développés pour ces coefficients. Par exemple, une méthode d'estimation des paramètres plasma utilisés dans le modèle de transport pour le contrôle est présentée dans (Geelen et al., 2015; Kim et al., 2016). Le profil de facteur de sécurité est un paramètre clé car il joue un rôle important dans la détermination de la stabilité MHD la décharge de plasma. Des modèles orientés sur le contrôle pour l'évolution du facteur de sécurité dans les scénarios avancés de tokamak peuvent être trouvés dans (Witrant et al., 2007). Les algorithmes de contrôle de rétroaction pour le facteur de sécurité peuvent être développés en utilisant la théorie de contrôle de rétroaction dimensionnelle finie ou infinie. Le modèle de contrôle fini-dimensionnel est obtenu par la discrétisation spatiale d'une équation différentielle partielle (EDP) de dimension infinie en employant une méthode de différence finie. Cette approche est appelée approche par agrégation précoce, dans laquelle les EDP sont approximativement agrégées et la conception de contrôle est basée sur ce modèle. Le second est l'approche tardive, ou approche dimensionnelle infinie. Un système de contrôle dimensionnel infini est un système dynamique dont l'état se trouve dans un espace vectoriel à dimensions infinies, typiquement une PDE. Dans cette approche de commande, la nature des paramètres distribués du système est maintenue le plus longtemps possible au cours de la conception de commande. Cette approche de contrôle permet de concevoir des stratégies de contrôle de rétroaction pour le profil complet dans tout le rayon du plasma. Les algorithmes de contrôle pour le profil de facteur de sécurité basés sur une approche MIMO (Multi Input Multi Output), utilisant des modèles à dimensions finies sont été utilisés dans de nombreuses études (Boyer et al., 2013; Boyer et al., 2014; Laborde et al., 2005; Vu et al., 2016; Kim and Lister, 2012). Ces conceptions de contrôle sont déjà testées et mises en œuvre dans des expériences tokamaks réelles.
Plusieurs travaux sont consacrés au contrôle dimensionnel infini du profil de facteur de sécurité (Bribiesca Argomedo et al., 2013a; Gahlawat et al., 2012; Gaye et al., 2013a; Gaye et al., 2013b).

L'objectif principal de cette thèse est d'étendre les algorithmes de contrôle développés à l'aide de la théorie de contrôle dimensionnel infinie à la commande simultanée de plusieurs paramètres plasma magnétique et cinétique. Cette extension nous permet d'avoir un contrôle plus avancé de plusieurs paramètres plasma. Ceci améliore les performances de la commande puisque la dynamique des paramètres magnétiques est connue pour être couplée à la température des électrons par la résistivité du plasma et le courant de bootstrap,

tous deux étant fortement dépendants de la température. Dans les travaux antérieurs qui utilisaient des stratégies de contrôle dimensionnel infinies, ces paramètres ont été simplifiés et leur dépendance à la température était négligée. En particulier, dans cette thèse, l'accent sera mis principalement sur le contrôle simultané du facteur de sécurité (et de son inverse) et des paramètres électroniques température/pression. Les algorithmes de contrôle pour le contrôle simultané des paramètres plasma couplés sont déjà développés en utilisant des modèles basés sur des principes premiers. Les stratégies de contrôle de rétroaction pour le facteur de sécurité couplé et la température électronique sont présentées dans (Kim and Lister, 2012; Barton et al., 2015c) Les modèles orientés sur la commande et le contrôle de rétroaction pour le profil du facteur de sécurité plasmatique et la dynamique de l'énergie stockée sont présentés dans (Barton et al., 2015b; Barton et al., 2015a). Dans tous ces travaux, la stratégie de contrôle est développée sur des modèles réduits par la discrétisation spatiale et en appliquant des stratégies de contrôle par rétroaction dimensionnelle finie. Dans cette thèse, un modèle orienté linéarisé orienté pour le contrôle dimensionnel infini sera présenté et utilisé pour la première fois pour la conception de contrôle PDE. Contrairement aux travaux antérieurs dédiés au contrôle simultané de plusieurs paramètres plasmatiques, les stratégies de contrôle par rétroaction sont basées sur la théorie du contrôle dimensionnel infini.

Les stratégies de contrôle présentées dans cette thèse sont testées à l'aide de simulateurs de plasma avant d'être appliquées dans des expériences tokamak réelles. Au fil des années, différents types de codes informatiques complexes sont développés pour simuler les modèles prédictifs pour l'évolution des profils plasma magnétique et cinétique dans les plasmas toroïdaux, tels que le flux magnétique poloidal et la température des électrons. Des modèles non linéaires approximatifs de l'évolution dynamique du plasma sont utilisés dans plusieurs simulateurs comme CRONOS (Basiuk et al., 2003; Artaud et al., 2010), ASTRA (Pereverzev and Yushmanov, 2002), PTRANSP (Hawryluk, 1980), RAPTOR (Felici et al., 2011; Felici and Sauter, 2012) entre autres. Certains des paramètres au sein de ces simulateurs sont calculés à partir des premiers modèles de principe, mais d'autres, comme la diffusivité de la chaleur, sont empiriquement ou semi-empiriquement estimés.

Les principales contributions de cette thèse peuvent être résumées ainsi:

- Un modèle linéarisé orienté de commande pour le facteur de sécurité couplé et la température électronique qui peut être utilisé pour des méthodes de commande dimensionnelle infinie;
- Une technique d 'identification de système pour le facteur de sécurité couplé et la température d' électrons en utilisant une combinaison d 'identification d' espace d 'état et de méthode d' erreur de sortie;
- Développer des algorithmes de contrôle pour le contrôle simultané du facteur de

sécurité et de la température électronique en utilisant des réglages dimensionnels infinis;

- Désignation d'une fonction de Lyapunov pour les phénomènes de transport hétérogène couplé;
- Déconnexion du problème de contrôle à l'aide de la théorie des perturbations singulières et calcul du contrôle composite;
- Développer des algorithmes de contrôle pour le facteur de sécurité couplé et le plasma β en utilisant le contrôle proportionnel-intégral;
- Test des algorithmes de contrôle utilisant le simulateur non linéaire RAPTOR pour la machine tokamak TCV.

La thèse est organisée comme suit:

Chapitre 1

L'objectif principal de ce chapitre est de présenter les équations de l'évolution de certaines quantités de transport dans des plasmas tokamaks. Ces équations sont la base du développement d'un modèle de contrôle pour le contrôle simultané des paramètres magnétiques et cinétiques couplés dans le plasma tokamak des scénarios avancés de tokamak. Il existe plusieurs paramètres plasma, tels que le facteur de sécurité, le flux magnétique, la température des électrons, le facteur de pression normalisé, etc., qui définissent l'état plasmatique et la performance. Un des principaux paramètres magnétiques que nous souhaitons contrôler dans cette thèse est le facteur de sécurité (ou son inverse). Ce paramètre est étroitement lié à la dérivée spatiale du flux magnétique poloidal, dont l'évolution est régie par une équation parabolique. La forme du profil de facteur de sécurité est importante à la fois pour le transport thermique plasmatique et la stabilité MHD. Le profil de température électronique détermine la résistivité du plasma qui régit l'évolution du profil du facteur de sécurité. Un problème clé pour les scénarios avancés de tokamaks est le contrôle simultané, en temps réel, de plusieurs profils de quantités plasmatiques. Dans ce chapitre, nous présentons un modèle de ces grandeurs.

Chapitre 2

Pour un objectif de conception de contrôle, un modèle linéarisé peut être utilisé avec succès dans la plupart des cas. Les modèles linéaires sont plus faciles à comprendre et nous

permettent d'utiliser un large panel de méthodes de contrôle. La linéarisation implique la création d'une approximation linéaire d'un système non linéaire valide dans une petite région autour d'un point d'équilibre. Le point d'équilibre est extrait d'une condition d'équilibre. Dans ce chapitre, deux types de modèles linéarisés sont présentés. Le premier est un modèle dite de premier principe dérivé de la linéarisation directe du modèle donné analytiquement dans le chapitre précédent. L'autre façon d'obtenir un modèle linéarisé du système est d'utiliser des techniques d'identification de système appliquées aux données de mesure. Cette approche ne nécessite pas une connaissance exacte des équations complexes du système. Les paramètres des modèles pilotés par données sont calculés en ajustant au mieux les sorties du modèle identifié avec les données mesurées.

Afin d'identifier un système MIMO de grand ordre qui pourrait conduire à une meilleure précision par rapport aux travaux précédents, une combinaison d'une méthode d'identification de sous-espace et des méthodes d'identification d'erreur de sortie est utilisée dans cette thèse. L'identification sous-espace est une méthode puissante pour l'identification de l'espace d'état des systèmes MIMO (Katayama, 2006; Ljung, 1998; Verhaegen and Dewilde, 1992; Di Ruscio, 1997).

L'identification est réalisée à l'aide des données fournies par le code METIS, un outil de simulation tokamak intégré rapide pour la suite CRONOS. Le code METIS est conçu comme un simulateur rapide de tokamak implémenté dans MATLAB ®. Ces ensembles de données simulent les décharges plasmatiques et la méthode d'identification peut être testée. Ici, un simulateur non linéaire est utilisé pour simuler l'évolution du plasma dans le tokamak DIII-D.

Chapitre 3

Dans ce chapitre, des algorithmes de contrôle pour le contrôle simultané du facteur de sécurité tokamak et de la température électronique sont présentés. Le système couplé est donné par deux équations de diffusion résistive linéaire 1D couplées dans un domaine circulaire. La conception de commande est basée sur le réglage dimensionnel infini en utilisant les fonctions de contrôle de Lyapunov (CLF). Une CLF est une fonction candidate de Lyapunov dont la dérivée peut être rendue négative par le choix des valeurs de contrôle (Kokotovic and Freeman, 1996). Les algorithmes de contrôle pour les plasmas tokamaks utilisant une approche à dimension infinie ont déjà été utilisés auparavant. Ces travaux sont dédiés au contrôle du facteur de sécurité plasma en utilisant uniquement l'évolution de l'équation de la dynamique du flux magnétique. Dans (Bribiesca Argomedo et al., 2013a) une CLF stricte pour l'équation de diffusion du gradient de flux magnétique poloidal est calculée. Ici, le coefficient de diffusion est considéré comme étant l'espace et le temps variant

et les propriétés de stabilité d'entrée à l'état du système sont examinées. Pour traiter le coefficient de diffusion non constant, la fonction candidate de Lyapunov est proposée sous la forme d'une norme L_2 pondérée. Une approche similaire est utilisée dans (Gahlawat et al., 2012) en employant le cadre des polynômes de somme des carrés pour maximiser le courant de bootstrap. Dans (Gaye et al., 2013a), il a été développé un contrôleur Proportionnel Intégral (PI) pour la stabilisation de la répartition spatiale du profil courant des plasmas tokamaks pour $\mathcal{H}\infty$. Dans ce chapitre, on considèrera le couplage fort entre la dynamique de la température des électrons et l'équation du flux magnétique et on développera la rétroaction simultanée de ces paramètres. Il existe plusieurs travaux dédiés au contrôle simultané de la température électronique et du facteur de sécurité (Kim and Lister, 2012; Barton et al., 2015c) utilisant une approximation de dimension finie du système.

Dans le système couplé, il existe une grande différence entre les échelles de temps des deux paramètres plasmatiques. Cette différence varie avec la taille des dispositifs tokamaks. Ainsi, dans ce chapitre, deux conceptions de contrôle sont proposées. Dans le premier cas, une analyse de stabilité du système à couplage complet est réalisée et une stratégie de contrôle est développée sans diviser les composantes lente et rapide. Dans la deuxième approche, les deux échelles de temps sont découplées. Pour la stratégie de contrôle, un contrôle composite est utilisé. Le contrôle composite est conçu en utilisant la théorie des perturbations singulières, où la composante rapide de la température électronique est découplée de la composante lente qui est gouvernée par l'évolution du gradient de flux magnétique z. La théorie des perturbations singulières est largement utilisée dans la théorie des systèmes de contrôle. Le modèle de perturbation singulier d'un système dynamique est un modèle dans lequel les dérivées de certains états sont multipliées par un petit paramètre positif ε. Les concepts de base et les définitions des systèmes perturbés singuliers de dimension finie peuvent être trouvés dans (Kokotovic, Khalil, and O'reilly, 1999; Khalil and Grizzle, 1996; Gajic, 2001). Il existe plusieurs travaux consacrés à l'analyse de la stabilité et au contrôle des limites des systèmes à dimensions infinies singulièrement perturbés. Un contrôle limite d'une classe de systèmes hyperboliques linéaires de lois de conservation basés sur la méthode de perturbation singulière est présenté dans (Tang, Prieur, and Girard, 2014). L'analyse de stabilité et le contrôle de backstepping des PDE paraboliques singulièrement perturbées sont présentés dans (Vazquez and Krstic, 2008).

La stratégie de contrôle proposée dans ce chapitre est testée sur RAPTOR (simulateur de transport de plasma rapid) (Felici and Sauter, 2012). RAPTOR est un code physique basé sur la commande pour simuler l'équation de diffusion du flux poloidal couplé au plasma 1D et le transport de la température électronique. Les équations de transport utilisées dans ce simulateur sont non linéaires et sont accordées pour correspondre aux données obtenues à partir de l'opération tokamak réelle. Le code est utilisé comme un outil pour la conception des applications de contrôle en temps réel, la simulation de plasma rapide et comme un simulateur en temps réel en parallèle avec la décharge de plasma dans le tokamak TCV. Le

contrôle distribué est effectué en utilisant l'actionnement de chauffage par résonance par cyclotron électronique (ECRH).

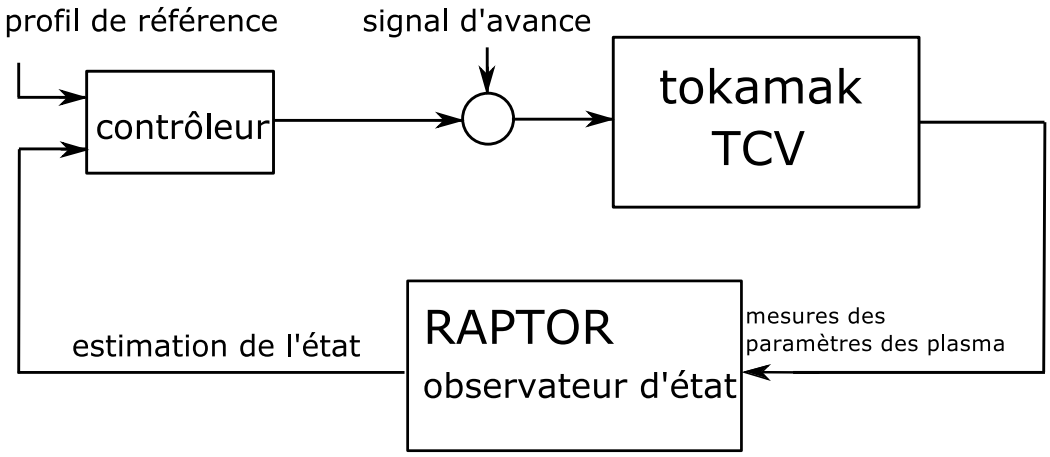
Chapitre 4

Dans ce chapitre, les algorithmes en boucle fermée basés sur le modèle sont dérivés pour contrôler l'inverse du profil du facteur de sécurité et le paramètre de pression β. La stratégie de contrôle présentée dans ce chapitre est appliquée à la configuration de l'installation expérimentale pour le tokamak TCV. Le code RAPTOR est utilisé comme observateur d'état pour estimer en temps réel les quantités de plasma clés. RAPTOR est développé pour fonctionner en parallèle avec le système de contrôle TCV (Fig. 3a). Cela permet d'estimer les profils plasmatiques dans de nombreux points de discrétisation et d'estimer plusieurs quantités non mesurables qui sont cruciales pour la mise en œuvre du contrôle. Comme cela a été démontré dans la section précédente, RAPTOR peut également être utilisé comme simulateur de plasma non linéaire (Fig. 3b). Cela permet de tester les algorithmes de contrôle avant leur mise en œuvre dans les expériences TCV réelles. La robustesse et les performances du contrôleur peuvent être testées dans des simulations en tenant compte de différents scénarios qui peuvent affecter les performances des algorithmes de contrôle lorsqu'ils sont appliqués dans le système de contrôle TCV réel.

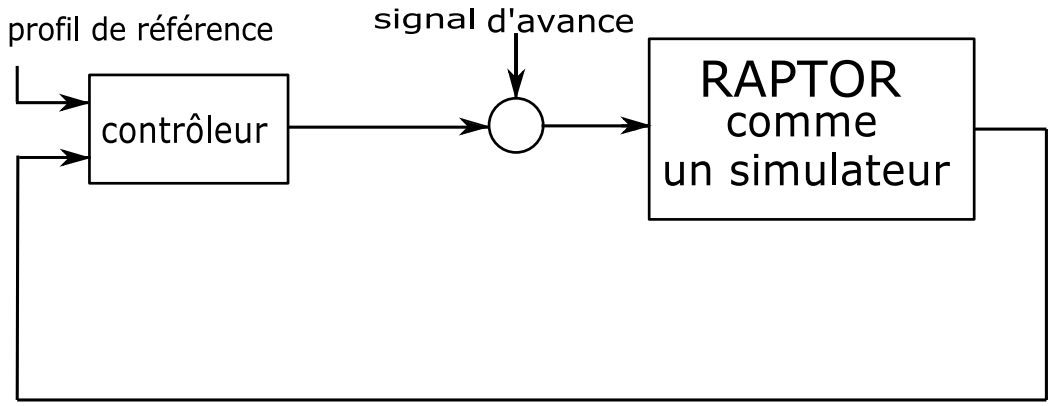
Plusieurs travaux sont déjà dédiés au contrôle simultané du facteur de sécurité et des paramètres de pression pour les scénarios avancés de tokamaks. Dans (Moreau et al., 2013) des expériences en boucle fermée réussies sont effectuées pour le contrôle simultané du profil de flux poloidal interne Ψ_r associé au paramètre de pression normalisé, β_N. Ici, le modèle axé sur le contrôle est obtenu à partir de données expérimentales utilisant une méthode générique à deux échelles de temps. Le contrôle simultané de q profile et β_N en utilisant le modèle physique basé sur les premiers principes est développé pour les scénarios de mode H de DIII-D dans (Barton et al., 2015a) et pour les scénarios de H-mode en plasma de ITER dans (Barton et al., 2013; Barton et al., 2015b). Les modèles dimensionnels infinis utilisés dans ce travail sont discrétisés spatialement en employant une méthode de différence finie. Le contrôle a été développé à l'aide d'algorithmes de contrôle de rétroaction robustes pour les systèmes de dimension finie.

Le modèle utilisé dans ce chapitre est représenté par un système couplé d'une diffusion résistive 1D (ι control) et d'une équation différentielle ordinaire non linéaire (β control). Contrairement aux travaux précédents dédiés à la commande simultanée du facteur de sécurité et des paramètres de pression (Barton et al., 2015b; Barton et al., 2015a), ici le contrôle du profil de facteur de sécurité est basé sur des réglages dimensionnels infinis. En raison des différentes échelles de temps de deux quantités, le contrôle a été synthétisé

en concevant des algorithmes de contrôle distincts pour les composantes rapide et lente. L'algorithme de contrôle de la composante lente représentée par z -profile est similaire au contrôleur proportionnel-intégral proposé dans (Gaye et al., 2013a) où le profil de flux poloïdal interne, Ψ_r, est utilisé pour la conception de contrôle. Lorsque l'action intégrale est présentée dans la commande avec un actionneur saturé, elle peut provoquer le phénomène bien connu de l'enroulement de l'intégrateur. Pour éviter les inconvénients de la saturation de l'actionneur dans le système, un compensateur anti-retour est ajouté à la conception de commande. La stabilité et les techniques anti-liquidation pour les systèmes à actionneurs saturés sont synthétisées comme dans (Tarbouriech et al., 2011; Bohn and Atherton, 1995). Dans la dernière section de ce chapitre, les résultats des simulations de contrôle utilisant RAPTOR sont présentés. La robustesse et la performance des algorithmes de contrôle sont testées en utilisant plusieurs scénarios. Dans ces scénarios, différentes incertitudes et perturbations des paramètres plasmatiques sont envisagées.



(a) Un observateur d'état basé sur RAPTOR est utilisé pour de contrôle de tokamak TCV. L'état du plasma est reconstruit à partir des mesures disponibles.



(b) RAPTOR utilisé comme simulateur de plasma. L'état plasma simulé est obtenu directement à partir de RAPTOR.

Figure 3: Code rapide d'évolution du profil plasma RAPTOR.

Introduction

Thermonuclear fusion

Fusion reactions are high energy reactions in which two light atomic nuclei fuse to form a heavier nucleus. The nuclear fusion reaction powers the Sun and the stars, emitting a vast amount of radiation. The energy from the Sun is available in the Earth directly from the sunlight and is indirectly converted into different forms of energy, such as hydro-power, fuel energy, wind energy etc., that are substantial sources of energy on earth. Increased energy demand and the high reliance on predominantly fossil fuels makes the current energy situation unsustainable, and there is an increased research on the new renewable sources of energy. Nuclear fission has been used as a source of electricity generation for many years. But this kind of energy is related to a high risk of instability of the nuclear power plants and nuclear waste that is dangerous for the environment. In the search for clean and safe energy sources, a great effort has been dedicated to the development of controlled thermonuclear fusion. Controlled nuclear fusion power has the potential to provide sustainably and sufficient energy, with a relatively small impact on the environment.

However, constructing a nuclear fusion reactor that can maintain fusion reaction and provide sustainability is not a simple task. The most promising fusion reaction at the lowest energy is the one in which nucleus of Deuterium (D) and Tritium (T) atoms fuse into a single Helium (He) and a neutron (n) (Wesson and Campbell, 2011):

$$ {}^{2}_{1}\mathrm{D} + {}^{3}_{1}\mathrm{T} \rightarrow {}^{4}_{2}\mathrm{He} + {}^{1}_{0}\mathrm{n} + E \tag{2} $$

where the fraction of the total mas deficit (δm) is released as a form of kinetic energy $E = \delta m c^2 = 17.6$ MeV. Deuterium is one of two stable isotopes of hydrogen and can be easily extracted from ordinary water. The tritium does not appear naturally but it can be produced in nuclear reactors by neutron activation of lithium, of which there are large natural reserves. This means that there are easily available fuel reserves for this kind of energy production.
To reach a thermonuclear fusion energy there should be a sufficient amount of energy to achieve the reaction (2). To overcome the Coulomb barrier (mutual repulsion of the particles), the positively charged nuclei of the nuclear fuel must be sufficiently hot. At these temperatures all atoms are ionized, creating unbound positive and negative particles called plasma state. In the fusion reactors, the plasma is heated to maintain the fusion process: this is referred to as ignition. The requirements of ignition have been presented formally by the Lawson criterion (Lawson, 1957). The single parameter of the criterion that is used for the measurement of the efficiency of the fusion reactor is presented by the triple

product $nT\tau_E \geq 31021 m^3 keV s$, of density ($n$), temperature ($T$) and energy confinement time (τ_E). This implies that the fuels need to be heated to extreme temperatures for this criterion to surpass the critical value necessary to ignite the plasma.

Tokamak device

Tokamaks are large devices using magnetic field to confine and heat plasma in the shape of a torus. The aim of tokamak research is to build a reliable power production system using thermonuclear fusion (Wesson and Campbell, 2011). Tokamak is the reactor concept that has achieved the highest value of $nT\tau_E$ and together with the stellarator is considered as one of the most promising sources of sustainable fusion energy. Tokamaks design was inspired by the idea of Oleg Lavrentiev (Bondarenko, 2001) and developed in the 1950s by Soviet physicists Igor Tamm and Andrei Sakharov. The name tokamak comes from the Russian acronym "ТОроидальная КАмера с МАгнитными Катушками" (toroidal'naya kamera s magnitnymi katushkami) which means toroidal chamber with magnetic coils.

There are many tokamaks around the world, for example JET, MAST, Tore supra, DIII-D, JT-60U and TCV (Fig. 4) that are used for experimental research. The experiments of these tokamaks have made significant progress towards realizing the goal of fusion energy. The International Thermonuclear Experimental Reactor (ITER) is the leading research project that aims to prove the feasibility of the thermonuclear fusion. This project is currently under construction in Cadarache, France and should present the transition from experimental studies of plasma physics to fusion power stations that are capable of producing sustainable energy.
The plasma current, which contributes to heating the plasma and generates the poloidal magnetic field, is primarily inducted by the ohmic heating coil. The toroidal magnetic field B_ϕ, is produced by the toroidal field coils and the poloidal field B_ψ is produced by the currents inside the plasma. Additional non-inductive currents and plasma heating are obtained through the injection of high energy neutral particles and electromagnetic waves. Among the most commonly used heating and current drive systems are the neutral beam injection, electron cyclotron resonance heating or current drive, ion cyclotron resonance heating, fast wave current drive and lower hybrid current drive. A schematic diagram of the main magnetic field and current configuration in a tokamak is shown in Fig. 5.

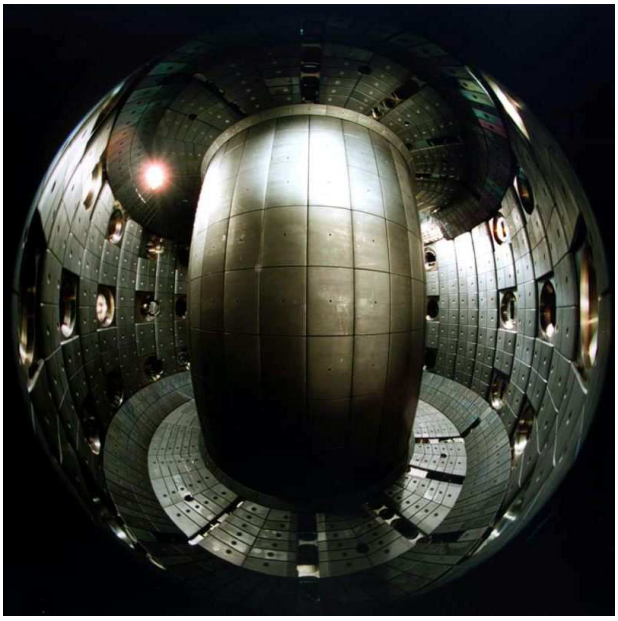


Figure 4: The inner view of TCV in Swiss Plasma Centre

Problem formulation and prior work

One of the main challenges in the tokamak plasma control is to achieve the so-called advanced tokamak steady-state scenarios which will play a significant role, since they will allow to reproduce and study the conditions that are expected to be obtained in a fusion plant of reduced size and costs (Taylor, 1997). The advanced tokamak scenarios are characterized by a high fusion gain, good plasma confinement and MHD stability that are crucial for the plasma performance and stability. A high-gain fusion burn could be achieved while a major fraction of the plasma current is self-generated by the neoclassical bootstrap effect that would reduce the necessary amount of auxiliary current-drive needed to maintain the desired scenario (Gormezano et al., 2007). The control challenges are generally separated into two groups: electromagnetic control and kinetic control. The state variables appear naturally in the evolutions of the internal poloidal magnetic flux that is closely related to the safety factor, and of a set of fluid/kinetic variables such as the plasma density, toroidal velocity, and ion and electron temperatures. Real-time simultaneous control of several radially distributed magnetic and kinetic plasma parameters is one of the main challenges in the control of advanced tokamak scenarios. The magnetic and kinetic profiles are known to be strongly coupled and integrating them into a single controller is particularly important for the advanced tokamak scenarios in future fusion devices such as ITER.

Simultaneous real-time control of magnetic and kinetic plasma parameters, such as the

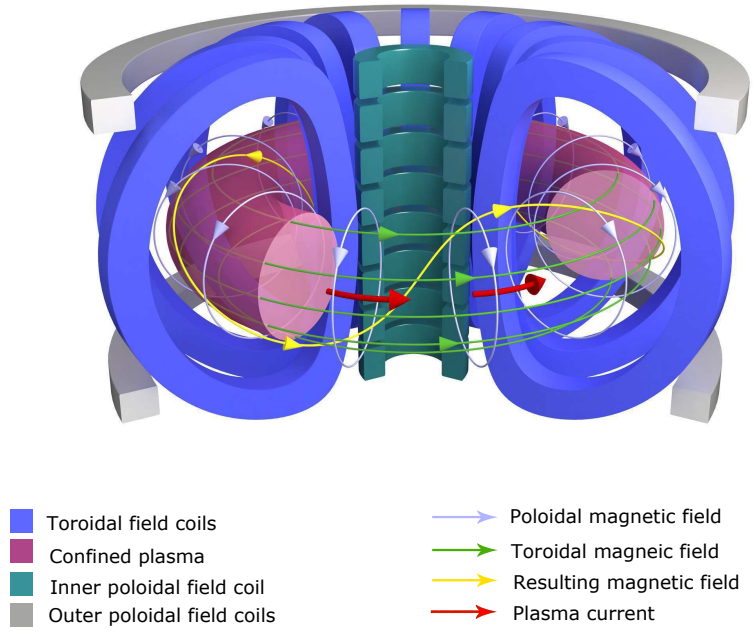


Figure 5: Representation of the coils and magnetic fields in a tokamak

current and electron temperature gradient profiles, was achieved for the first time during the experimental campaigns on JET (Mazon et al., 2003; Laborde et al., 2004; Moreau et al., 2003). In these pioneering works, the controller is based on the static plasma response only, and on an algorithm that minimizes a weighted sum of least-square integral errors between the requested profiles and the measured ones. More advanced control strategies are developed after that, and applied in other tokamak devices such as Tore Supra, DIII-D and JT-60U. Model based control algorithms can be developed by using two kinds of control models. The first one is a data-driven model extracted using identification techniques. This model is obtained using only measurement data and system identification techniques, thus exact knowledge of the system dynamics is not necessary. Control algorithms for simultaneous control of coupled kinetic and magnetic plasma parameters, based on two-time-scales dynamic plasma data-driven models are presented in (Moreau et al., 2008; Moreau et al., 2013; Moreau et al., 2011).

The second one is a first-principle-driven which model converts the fundamental physical laws that govern the behavior of the plasma to a control-oriented model suitable for

a control design. Such model simplifies the evolution models of the systems by considering only the dominant physics of the plasma dynamics that are relevant to the control objective (Witrant et al., 2007; Felici, 2011). The control models are based of the physical transport equations that govern the evolution of the plasma parameters. These models are not easy to be obtained because many of the transport coefficients are not well known. For this reason some empirical models are developed for these coefficients. For example, an estimation method of the plasma parameters used in the transport model for control are presented in (Geelen et al., 2015; Kim et al., 2016).

The safety factor profile is a key parameter as it plays a key role in determining the MagnetoHydroDynamic (MHD) stability of the plasma discharge. Control oriented models for the safety factor evolution in advanced tokamak scenarios can be found in (Witrant et al., 2007). The feedback control algorithms for the safety factor can be developed by using finite or infinite dimensional feedback control theory. The finite-dimensional control model is obtained by spatial discretization of a infinite dimensional Partial differential Equation (PDE) by employing a finite difference method. This approach is called an early lumped approach, in which the PDEs are approximated (lumped) first and the control design is based on this model. The second one is the late lumping approach, or also called infinite dimensional approach. An infinite dimensional control system is a dynamical system whose state lies in an infinite dimensional vector space, typically a PDE. In this control approach the distributed parameter nature of the system is kept as long as possible in the course of the control design. This control approach allows to design feedback control strategies for the full profile throughout the plasma radius.
Control algorithms for the safety factor profile based on a Multi Input Multi Output (MIMO) approach using finite dimensional models are used in many previous works (Boyer et al., 2013; Boyer et al., 2014; Laborde et al., 2005; Vu et al., 2016; Kim and Lister, 2012). These control designs are already tested and implemented into a real tokamak experiments. There are several works that are dedicated to the infinite dimensional control of the safety factor profile (Bribiesca Argomedo et al., 2013a; Gahlawat et al., 2012; Gaye et al., 2013a; Gaye et al., 2013b).

The main goal of this thesis is to extend the control algorithms developed using infinite dimensional control theory to the simultaneous control of several magnetic and kinetic plasma parameters. This extension allows us to have more advanced control of several plasma parameters. This improves the performance of the control since the dynamics of the magnetic parameters is known to be coupled with the temperature of the electrons through the plasma resistivity and the bootstrap current, both being highly dependent on the temperature. In the previous works that were using infinite dimensional control strategies, these parameters were simplified and their dependence on the temperature is neglected. In particular, in this thesis, the main focus will be in simultaneous control of the safety factor (and its inverse) and the electron temperature/pressure parameters. Control

algorithms for simultaneous control of coupled plasma parameters are already developed using first-principles-driven models. Feedback control strategies for the coupled safety factor and electron temperature are presented in (Kim and Lister, 2012; Barton et al., 2015c; Maljaars et al., 2015). Control-oriented models and feedback control for the plasma safety factor profile and stored energy dynamics are presented in (Barton et al., 2015b; Barton et al., 2015a; Felici, 2011). In all these works the control strategy is developed on models reduced by spatially discretization and applying finite dimensional feedback control strategies. In these thesis, a linearized control oriented model for infinite dimensional control will be presented and used for the first time for PDE control design. In contrast of the previous works dedicated to simultaneous control of several plasma parameters, in this thesis, the feedback control strategies are based using infinite dimensional control theory.

The control strategies presented in this thesis are tested using plasma simulators before being applied in real tokamak experiments. Over the years, different types of complex computer codes are developed to simulate the predictive models for the evolution of the magnetic and kinetic plasma profiles in toroidal plasmas, such as poloidal magnetic flux and electron temperature. Approximate nonlinear physics-based models of the plasma dynamic evolution are being used in several simulators like CRONOS (Basiuk et al., 2003; Artaud et al., 2010), ASTRA (Pereverzev and Yushmanov, 2002), PTRANSP (Hawryluk, 1980), RAPTOR (Felici et al., 2011; Felici and Sauter, 2012) and several others. Some of the parameters in these simulators are calculated from first principle models, but others like the heat diffusivity, are empirically or semi-empirically estimated.

The main contributions of this thesis can be summarized as:

- A control-oriented linearized models (data-based and first-principle models) for the coupled safety factor and the electron temperature that can be used for infinite dimensional control methods;
- A system identification technique for the coupled safety factor and electron temperature using a combination of state space identification and output error method;
- Developing control algorithms for simultaneous control of the safety factor and the electron temperature using infinite dimensional settings;
- Designing a Lyapunov function for coupled inhomogeneous transport phenomena;
- Decoupling the control problem using singular perturbation theory and calculating composite control;
- Developing a control algorithms for coupled safety factor and plasma β using proportional-integral control;

- Testing the control algorithms using RAPTOR nonlinear simulator;
- Implementation of the proposed control algorithms in the TCV tokamak device.

Outline

The thesis is organized as follows:

- Chapter 1 presents the physical model of the main plasma quantities that are used in this thesis. The model for these parameters is simplified and is suitable for control design;
- Chapter 2 presents two control-oriented models that can be used for a control design. In this chapter, two kinds of models are developed. The first kind is the first-principles-driven model obtained by linearizing the equations presented in Chapter 1. This control model is expressed in a way that could be used in the infinite dimensional control design. The second kind of model presented in this chapter is the data-driven model. The data-driven model in this chapter is obtained using combination of subspace and output error methods for state-space models. The model is identified and validated using data extracted from the nonlinear METIS simulator using the configuration of DIII-D tokamak;
- Chapter 3 presents control algorithms for the coupled electron temperature and safety factor. The control in this chapter is developed using the models presented in Chapter 2 and the algorithms are based on infinite dimensional control theory. First, the stability and the convergence of the system are investigated using Lyapunov techniques. The control strategy for the coupled plasma quantities is developed using a control Lyapunov function. The control strategy is expanded by decoupling the system using singular perturbation theory, which takes into consideration the time scale difference between the kinetic and the magnetic quantities. The control strategy in this case is calculated as a composite control, calculating separately and combining the control signals for the fast and the slow component of the system. The control strategy presented in this chapter is tested in RAPTOR simulations for ITER;
- Chapter 4 presents control algorithms for the coupled safety factor and plasma β parameters. The control model in this chapter is presented by combining coupled PDE and ODE equations. The composite control is calculated separately for the two components. Proportional-integral actions with anti-windup are implemented for both plasma parameters. The control is tested using RAPTOR simulator, configured for the experimental settings of the TCV tokamak;

- This manuscript is ended by concluding discussion and some future research perspectives.

Chapter 1

Transport equations and control problem formulation

Contents

1.1 Poloidal Magnetic Flux in a tokamak 23

1.1.1 Boundary conditions 25

1.2 Electron temperature equation 25

1.3 Model outputs 27

1.4 Model inputs 29

1.5 Control problem formulation 31

The main goal of this chapter is to present the equations of the evolution of some transport quantities in tokamak plasmas. These equations are the basis for the development of a control model for simultaneous control of the coupled magnetic and kinetic parameters in tokamak plasma of advanced tokamak scenarios. There are several plasma parameters, such as the safety factor, magnetic flux, electron temperature, normalized pressure factor, etc., that define the plasma state and performance. One of the main magnetic parameter in which we are interested to control in this thesis, is the safety factor (or alternatively its inverse). This parameter is closely related to the spatial derivative of the poloidal magnetic flux, whose evolution is governed by a parabolic equation. The shape of the safety factor profile is important both for plasma thermal transport and MHD stability. The electron temperature profile determines the plasma resistivity that governs the evolution of the safety factor profile. A key issue for advanced tokamak scenarios is the simultaneous control, in real time, of several plasma quantities profiles. In this chapter a control oriented model of these quantities is presented. The important variable definitions that are used in this work are given in Table 1.1.

Variable	Symbol	Unit
a	small plasma radius	m
B	magnetic field	T
B_ψ	poloidal magnetic field	T
B_ϕ	toroidal magnetic field	T
B_0	toroidal magnetic field at the center	T
I_p	total plasma current	A
j_{ni}	non inductive effective current density	A/m^2
j_{bs}	bootstrap current density	A/m^2
j_{aux}	auxiliary sources current density	A/m^2
n_e	electron density profile	m^{-3}
p	total pressure profile	eVm^{-3}
p_e	electron pressure profile	eVm^{-3}
P_{tot}	total input power	W
P_{OH}	ohmic power	W
P_{ei}	electron-ion loss power	W
P_{rad}	radiation loss power	W
P_{ec}	electron cyclotron heating power	W
Q_e	electron heating power density	W/m^3
Q_{OH}	ohmic power density	W/m^3
Q_{aux}	auxiliary sources power density	W/m^3
Q_{ei}	electron-ion loss power density	W/m^3
Q_{rad}	radiation loss power density	W/m^3
R	large plasma radius	m
R_0	magnetic center location	m
T_i	ions temperature profile	eV
T_e	electrons temperature profile	eV
V_{loop}	Toroidal loop voltage	V
W_{th}	plasma thermal energy	J
x	normalized spatial variable	
Z_{eff}	effective value of the plasma charge	
z	poloidal magnetic flux gradient	T/m^3
β	ratio of the plasma pressure to the magnetic pressure	
$\eta_{\|\|}$	plasma resistivity	$\Omega \times m$
Ψ	magnetic flux of the poloidal field	T/m^2
Φ	toroidal magnetic flux	T/m^2
q	safety factor	
ι	inverse of the safety factor	
χ_e	electron diffusivity	m^2/s
ρ	spatial variable along the small plasma radius	m
μ_0	permeability of vacuum	H/m
τ_{th}	global energy confinement time	s

Table 1.1: Most relevant physical variables and units

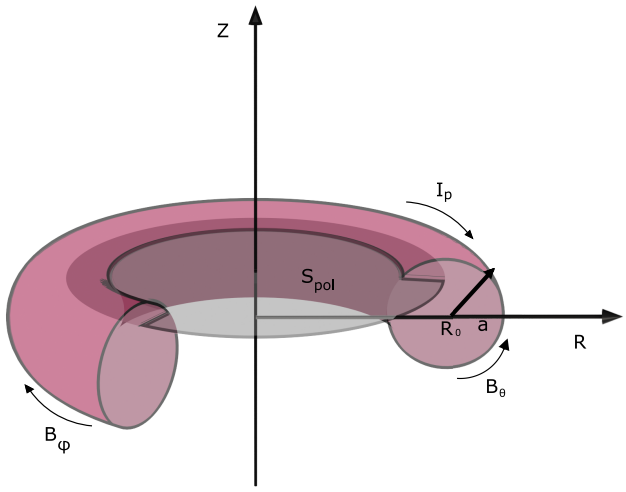


Figure 1.1: Plasma coordinates and surface S_{pol} used to define the poloidal magnetic flux

1.1 Poloidal Magnetic Flux in a tokamak

The poloidal magnetic flux Ψ is denoted as flux per radian of the magnetic field $\vec{B}(R, Z)$ through a disc centered on the toroidal axis at height Z and with a surface S_{pol} as presented in Fig. 1.1:

$$\Psi = \int_{S_{pol}} \vec{B} d\vec{S}_{pol} \tag{1.1}$$

The model for the poloidal magnetic flux dynamics that is going to be used in this work is presented by an approximate 1D diffusion equation of the plasma as in (Blum, 1989):

$$\frac{\partial \Psi}{\partial t} = \frac{\eta_{\parallel} \rho}{\mu_0 C_3^2} \frac{\partial}{\partial \rho} \left(\frac{C_2 C_3}{\rho} \frac{\partial \Psi}{\partial \rho} \right) + \frac{\eta_{\parallel} V' B_0}{F C_3 \rho} j_{ni} \tag{1.2}$$

where ρ is the toroidal flux coefficient indexing the magnetic surfaces, defined as: $\rho = \sqrt{\frac{\Phi}{\pi B_0}}$ (Φ being the toroidal magnetic flux and B_0 the toroidal magnetic field at the center of the

vacuum vessel), μ_0 is the permeability of vacuum, F is the diamagnetic function, V is the plasma volume and $V' = \frac{\partial V}{\partial \rho}$ is the spatial derivative of the plasma volume, $\eta_{\|}$ is the parallel electrical resistivity of the plasma, $j_{ni} = \frac{\langle \vec{j}_{ni} \vec{B} \rangle}{B_0}$ is non-inductive current density where $\langle \cdot \rangle$ denotes a flux-surface average. The coefficients C_2 and C_3 are defined as in (Blum, 1989):

$$C_2(\rho) = V' \left\langle \frac{|\nabla \rho|^2}{R^2} \right\rangle; \quad C_3(\rho) = V' \left\langle \frac{1}{R^2} \right\rangle \tag{1.3}$$

Neglecting the diamagnetic effect caused by the poloidal currents using a cylindrical approximation of the plasma geometry, the coefficients (1.3) can be simplified as in (Witrant et al., 2007):

$$C_2 = C_3 = \frac{4\pi^2 \rho}{R_0}; \quad V(\rho) = 2\pi^2 \rho^2 R_0; \quad V' = 4\pi^2 R_0 \rho; \quad F \approx R_0 B_0 \tag{1.4}$$

where R_0 is the major radius of the plasma (assumed constant in time) and a is the minor plasma radius corresponding to the last closed magnetic surface. The value of $\rho_{edge} = a$ is considered as a constant if the diamagnetic effect is neglected and a normalized variable $x = \frac{\rho}{a}$ can be defined. Using the previous approximations, (1.2) can be simplified as:

$$\frac{\partial \Psi}{\partial t} = \frac{\eta_{||}}{\mu_0 a^2 x} \frac{\partial}{\partial x} (x \frac{\partial \Psi}{\partial x}) + \eta_{||} R_o j_{ni} \tag{1.5}$$

The non-inductive current density j_{ni} is obtained by combining the auxiliary sources current density j_{aux} (heating and current drive external systems) and the bootstrap current density j_{bs}:

$$j_{ni} = j_{aux} + j_{bs} \tag{1.6}$$

The parallel resistivity of the plasma scales inversely with the electron temperature. Neoclassical resistivity models can be found in (Sauter, Angioni, and Lin-Liu, 1999; Sautera, Angioni, and Lin-Liub, 1999; Hirshman, Hawryluk, and Birge, 1977). In this work we are using simplified Spitzer resistivity model expressed as (Spitzer, 2013):

$$\eta_{||} = \frac{k_{sp} Z_{eff}}{T_e^{3/2}} \tag{1.7}$$

where $k_{sp}(\rho)$ is the spatial profile and Z_{eff} is the constant effective value of the plasma charge.

The bootstrap current is a self-generated current due to collisions between trapped particles and passing particles, and may be the main source of non inductive current in specific scenarios (Peeters, 2000). The model of the bootstrap current density can be used in a simplified version of the model presented in (Sauter, Angioni, and Lin-Liu, 1999) under the assumption of a tight coupling between the electron and ion species. In this assumption

the electron and the ion densities are considered to be equal $n_e = n_i$ and $\frac{\partial lnT_i}{\partial \Phi} = \frac{\partial lnT_e}{\partial \Phi}$, where T_i is the ion temperature. The approximated model is considered as in (Felici et al., 2011):

$$j_{bs} = \frac{k_{bs}}{\partial \Psi / \partial x}\left[\mathcal{L}_{31}\frac{\partial n_e}{\partial \rho}T_e + \left(\mathcal{L}_{31} + R_{pe}\mathcal{L}_{32} + (1 - R_{pe})\mathcal{L}_{34}\right)\frac{\partial T_e}{\partial \rho}n_e\right] \tag{1.8}$$

where $k_{bs}, \mathcal{L}_{31}, \mathcal{L}_{32}, \mathcal{L}_{34}$ depend on magnetic configuration of the plasma equilibrium and $R_{pe} = p_e/p$ is the ratio between electron and total pressure.

1.1.1 Boundary conditions

At the center of the plasma, the spatial variation of the flux is zero:

$$\frac{\partial \Psi}{\partial x}(0, t) = 0 \tag{1.9}$$

and on Last Closed Magnetic Surface (LCMS), two exclusive conditions can be considered. The boundary condition at the outer boundary is given by the coupling between the plasma and the externally induced voltage from the Ohmic coils. The first is on the flux variation:

$$\frac{\partial \Psi}{\partial x}(x = 1, t) = -\frac{R_o \mu_0 I_p(t)}{2\pi} \tag{1.10}$$

and second is on the flux rate:

$$\frac{\partial \Psi(1, t)}{\partial t} = -V_{ext}(t) \tag{1.11}$$

the initial condition is given by:

$$\Psi(x, t_0) = \Psi_0(x) \tag{1.12}$$

1.2 Electron temperature equation

In tokamak plasma the transport phenomena of the electron temperature T_e and density n_e are coupled and governed by a diffusion equation. The equation is developed from simplified 1D energy transport equation and is presented as in (Hinton and Hazeltine, 1976):

$$\frac{3}{2V'^{2/3}}\frac{\partial}{\partial t}\left(n_e T_e V'^{5/3}\right) = \frac{\partial}{\partial \rho}\left(n_e \chi_e \frac{\partial T_e}{\partial \rho} V' \left\langle |\nabla \rho|^2 \right\rangle\right) + Q_e \tag{1.13}$$

with boundary conditions:

$$\begin{aligned} \frac{\partial T_e}{\partial \rho}(0,t) &= 0 \\ T_e(\rho = a, t) &= T_{e,edge} \end{aligned} \tag{1.14}$$

and with initial condition:

$$T_e(\rho, t_0) = T_0 \tag{1.15}$$

Using the same cylindrical approximation as in the case of the equation of the magnetic flux, the temperature equation simplifies to:

$$\frac{3}{2}\frac{\partial\left(n_e T_e\right)}{\partial t} = \frac{1}{\rho}\frac{\partial}{\partial \rho}(\rho n_e \chi_e \frac{\partial T_e}{\partial \rho}) + Q_e \tag{1.16}$$

where χ_e is the electron diffusivity, and Q_e is the total electron heating power density. The electron heating energy source (the algebraic difference between the supplied and lost energies) is calculated as a sum of several contributions. In this thesis we simplify it by considering the following contributions:

$$Q_e = Q_{OH} - Q_{ei} - Q_{rad} + Q_{aux} \tag{1.17}$$

where Q_{OH} is ohmic effect power density, Q_{ei} is Electron-Ion heat exchange power density, Q_{rad} is radiation loss power density and Q_{aux} is auxiliary heating power density. The ohmic effect power density Q_{OH} that comes from the heating caused by the induced current is:

$$Q_{OH} = \frac{\eta_{||}}{\mu_0^2 R_0^2 \rho^2}\left(\frac{\partial}{\partial \rho}(\rho \frac{\partial \Psi}{\partial \rho})\right)^2 \tag{1.18}$$

The Electron-Ion heat exchange can be written as $Q_{ei} = n_e \nu_{eq}(T_e - T_i)$, where ν_{eq} neoclassical equipartition rate is given in (Hinton and Hazeltine, 1976).
For the ion temperature, a simplified model is used and it is directly related to T_e by $T_i = f_{Ti}(\rho)T_e(\rho)$, where $f_{Ti}(\rho)$ is a function chosen to best match the experimental results. The electron-Ion heat exchange can be written as a function of T_e as:

$$\begin{aligned} Q_{ei} &= n_e \nu_{eq}(T_e - T_i) \\ &= n_e \nu_{eq}(1 - f_{Ti}(\rho))T_e = f_{ei}(\rho)T_e \end{aligned} \tag{1.19}$$

where ν_{eq} is the neoclassical equipartition rate given in (Hinton and Hazeltine, 1976).
The radiation loss Q_{rad} is calculated as in (Wesson and Campbell, 2011):

$$Q_{rad} = f_{rad}(\rho)T_e^{1/2} \tag{1.20}$$

where $f_{rad} = k_{bem} n_e^2 Z_{eff}$ and $k_{bem} = 5.35 * 10^{-5} W m^3/(keV)^{1/2}$ is the Bremsstrahlung radiation coefficient.

The auxiliary heating power density Q_{aux} comes from the auxiliary heating sources.
The diffusion coefficient in this equation is not well known and there is no consensus about the mathematical formulation. Only some empirical models are developed for this coefficient. Simplified analytical expression for this parameter can be found in (Felici and Sauter, 2012; Polevoi, Medvedev, YU, et al., 2002; Kim et al., 2016), empirically Bohm type model can be found in (Taroni et al., 1994) and gyro-Bohm type transport models in (Erba et al., 1998; Artaud et al., 2005). For the control application in this thesis, a simple empirical local transport model of the Bohm type is used, given as in (Erba et al., 1998):

$$\chi_e = 2.510^{-4}\frac{T_e}{B_0}\frac{\mid \bigtriangledown p_e \mid}{p_e}q^2 \propto 2.510^{-4}\frac{\mid \bigtriangledown p_e \mid}{B_0 n_e}q^2 \tag{1.21}$$

where $p_e = n_e T_e$ is the electron pressure.
Using the normalized radial variable $x = \rho/a$, the transport equation can be simplified as:

$$\frac{3}{2}\frac{\partial\big(n_e T_e\big)}{\partial t} = \frac{1}{a^2}\frac{1}{x}\frac{\partial}{\partial x}(x n_e \chi_e \frac{\partial T_e}{\partial x}) + Q_e \tag{1.22}$$

with boundary conditions:

$$\begin{aligned}\frac{\partial T_e}{\partial x}(0,t) &= 0\\ T_e(x=1,0) &= T_{e,edge}\end{aligned} \tag{1.23}$$

and initial condition:

$$T_e(x,t_0) = T_{e,0}(x) \tag{1.24}$$

1.3 Model outputs

One of the key parameters to analyze the plasma stability and performance is the safety factor q, or its inverse ι. The safety factor denotes the ratio of toroidal to poloidal turns for a given magnetic field surface within a tokamak. The term "safety" refers to the resulting stability of the plasma. The equation that describes the evolution of q is defined as:

$$q = \frac{1}{\iota} = \frac{\partial\Phi}{\partial\Psi} = \frac{\partial\Phi/\partial x}{\partial\Psi/\partial x} = \frac{B_0 a^2 x}{\partial\Psi/\partial x} \tag{1.25}$$

where Φ is the toroidal magnetic flux defined as $\Phi = \int_{S_\Phi}\vec{B}d\vec{S}_\phi \approx \frac{\pi B_0 a^2 x^2}{2}$.
As the variables of main interest for the control (q,ι and current profiles) depend on the magnetic flux gradient $z = \frac{\partial\Psi}{\partial\rho}$, the focus in this thesis is on the evolution of the dynamics of z. Differentiating in space (1.5) gives the equation of evolution of its gradient:

$$\frac{\partial z}{\partial t} = \frac{\partial}{\partial x}\left(\frac{\eta_{||}}{\mu_0 a^2 x}\frac{\partial}{\partial x}(xz)\right) + \frac{\partial}{\partial x}(\eta_{||}R_o j_{ni}) \tag{1.26}$$

with boundary conditions (choosing I_p as input):

$$\begin{aligned} z(0,t) &= 0; \\ z(1,t) &= -\frac{R_o \mu_0 I_p(t)}{2\pi} \end{aligned} \tag{1.27}$$

and the initial condition:

$$z(x,t_0) = z_0 \tag{1.28}$$

Another variable that can be used for state variable for the control of the safety factor is the relative internal poloidal flux, $\Psi_r(x,t)$ that is obtained by the following transformation: $\Psi_r(x,t) = \Psi(x,t) - \Psi(1,t)$. The internal poloidal flux stands for the difference between the total poloidal magnetic flux and the total poloidal flux at the plasma boundary and it has stable dynamics. The state equation for the relative internal poloidal flux is given by:

$$\frac{\partial \Psi_r}{\partial t} = \frac{\eta_\parallel}{\mu_0 a^2}\frac{1}{x}\frac{\partial}{\partial x}\left(x\frac{\partial \Psi_r}{\partial x}\right) + \eta_\parallel R_0 j_{ni} + V_{ext} \tag{1.29}$$

with boundary conditions:

$$\begin{aligned} \frac{\partial \Psi_r}{\partial x}(0,t) &= 0 \\ \Psi_r(1,t) &= 0 \end{aligned} \tag{1.30}$$

The efficiency of the confinement of the plasma pressure by the magnetic field is represented by the plasma β parameter. It is defined as the ratio between the average pressure and the edge poloidal magnetic pressure. There are several measures of this type. Following (Wesson and Campbell, 2011), one commonly used is :

$$\beta = \frac{\langle p \rangle_V}{B_0^2/(2\mu_0)} = \frac{2}{3}\frac{W_{th}/V}{B_0^2/(2\mu_0)} \tag{1.31}$$

where W_{th} is the stored thermal energy in the plasma and $\langle \cdot \rangle_V$ denotes the volume-average operation $1/V \int_V (\cdot) dV$.
The normalized form, β_N, stands for the proximity to tokamak stability limits and is given by (Troyon et al., 1984):

$$\beta_N = \frac{a\beta[\%]B_0}{I_p[MA]} \tag{1.32}$$

The maximum achievable limit for β_N for typical tokamak plasmas but neglecting the effect of a conducting wall is given by the Troyon limit $\beta_N < 3.4$. The stored energy in the plasma, assuming a coupling between the electron and ion species is calculated as:

$$\begin{aligned} W_{th} &= \frac{3}{2}\int_V \big(n_e T_e + n_i T_i\big) dV \\ &= \frac{3}{2}\int_V \big(1 + f_{T_i}(\rho)\big) n_e T_e dV \end{aligned} \tag{1.33}$$

Assuming that the plasma volume does not change in time, the approximate energy balance equation is given by the nonlinear ODE represented by approximate stored energy W_{th}:

$$\frac{dW_{th}}{dt} = -\frac{W_{th}}{\tau_{th}} + P_{tot} \tag{1.34}$$

where τ_{th} is the global energy confinement time calculated using a scaling law, as in (Witrant and Brémond, 2011):

$$\tau_{th} = 0.14 I_p^{0.91} B_0^{-0.13} n_e^{0.77} P_{tot}^{-0.73} \tag{1.35}$$

and P_{tot} is the total input power that is calculated as: $P_{tot} = \int_0^1 Q_e \frac{dV}{dx} dx$.

1.4 Model inputs

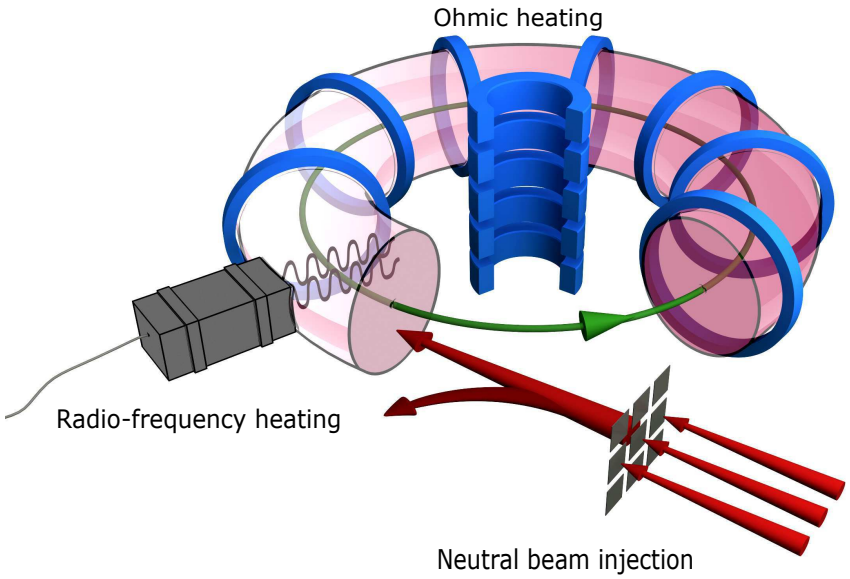


Figure 1.2: Ohmic and external heating in tokamak

The heating of the plasma comes from the electric currents obtained from several sources presented in Fig. 1.2. The main source of current in a tokamak is the one induced in the

plasma by the transformer action caused by the central ohmic coil. Other sources are the external heating sources. In this thesis, the following external heating sources are considered:

- Neutral beam injection (NBI). With the NBI heating systems, a beam of highly energetic neutral particles is injected into the plasma. This provides a source of non-inductive current as well as plasma heating through collisions;
- Radio-Frequency (RF) antennas. The RF heating sources produce electromagnetic waves outside the torus and their energy can be transferred to the charged particles in the plasma. There are several sources of high-frequency electromagnetic waves: Ion Cyclotron Resonance Heating (ICRH), Electron Cyclotron Resonance Heating (ECRH) and Lower Hybrid Heating (LHH).

For the model inputs in this work, the boundary conditions at the plasma edge are written in form of $\frac{\partial \Psi(1,t)}{\partial t}$ or $\frac{\partial \Psi}{\partial \rho}(1,t)$ and are related to the ohmic heating sources of the plasma trough V_{ext} and I_p. The local plasma loop voltage V_{ext} can be considered as a true actuator of the system that can be directly manipulated by the operator. The second boundary condition $\frac{\partial \Psi}{\partial \rho}(1,t)$ is related to the total plasma current, I_p, by means of (1.10) and this parameter can also be requested as the control input by the feedback algorithm. In the case where the plasma current is used as a control input, it is considered that the desired value of I_p is obtained by regulating the ohmic poloidal field coil voltage such that the plasma current follows the desired form requested by the controller. The regulation of I_p is usually done by applying a PID controller on the poloidal magnetic coils.
The external heating sources are considered as in-domain actuators. Using these actuators, the desired current density profile j_{aux} and the auxiliary heating power density profile Q_{aux} can be modulated. In most of the control applications, including this work, the number of external heating sources is limited and also their degrees of freedom. This imposes strong shape constraints for achievable profiles. For control design purposes a simple mathematical model for these deposits shapes can be used. The total auxiliary current is calculated as the sum of individual induced from each heating source:

$$j_{aux} = \sum_{i=1}^{n_{aux}} j_{aux,i} \tag{1.36}$$

where n_{aux} denotes the number of the auxiliary sources. For the ECCD antennas in (Felici et al., 2011), a simple approximate power and current densities are considered by weighted Gaussian distributions:

$$j_{aux,i} = \frac{T_e}{n_e} j_{dis,i}(x) P_{aux,i}(t) \tag{1.37}$$

which represents the product of the weighted Gaussian distributions $j_{dis,i}(x)$ representing the normalized reference current density deposition profiles, the input powers $P_{aux,i}(t)$ and the current-drive efficiency,$\frac{\overline{T}_e}{n_e}$, for the i-th electron cyclotron current drive.

The total auxiliary power density is calculated as a sum of the individuals induced from each external input:

$$Q_{aux} = \sum_{i=1}^{n_{aux}} Q_{aux,i} \tag{1.38}$$

The individual auxiliary power densities are modeled as:

$$Q_{aux,i} = Q_{dis,i}(x) P_{aux,i}(t) \tag{1.39}$$

where $Q_{dis,i}$ is a normalized reference power density deposition profile for the i-th auxiliary source.
In most of the control applications, the weighted Gaussian distributions are fixed by the choice of the position and distribution of the external heating sources such that they are compatible with the desired final state of the plasma parameters. This means that the only parameter, that is available to be manipulated by the control algorithm, is $P_{aux}(t)$.

1.5 Control problem formulation

The transport equations presented above are used to define the control model for important plasma parameters such as the safety factor and the plasma β coeficient, which are crucial for the performance and the stability of tokamak plasmas. The control of the plasma quantities is performed by using several actuation methods as a combination of boundary and in-domain actuators.
The main objective of this thesis is the simultaneous control of several plasma magnetic and kinetic parameters. Because of the complexity and high nonlinearities of the transport models in tokamak, a linearized model around the operation point is used for the control design. In Chapter 2, appropriate linear models for control design are presented. The linear control models of the two coupled transport equations can be obtained by:

- First-principle driven models, where the control model is based on the linearized equations presented in this section;
- Data-driven models, where measurement data from the tokamak machine are used to construct a model using system identification techniques.

The control approach considered in this thesis is based on infinite dimensional settings by using Lyapunov analysis applied on coupled partial differential equations of the plasma

transport. Using Lyapunov techniques we can guarantee the asymptotic stability of the system and also tune the speed of convergence to the reference profiles. Because of the different time scales between the magnetic and the kinetic parameters, the control strategy is modified by separating the fast from the slow component using singular perturbation theory.

Chapter 2

Linear models for control

Contents

2.1 First-principle linearized model for control 34
2.2 Data-driven model for control 36
2.2.1 Problem statement and identification procedure 37
2.2.2 Pre-processing the data for system identification 43
2.3 Subspace identification 44
2.3.1 MOESP method for system identification 44
2.3.2 Determining the order of the system 46
2.3.3 Eigenvalues constraints in subspace identification 47
2.4 Output-error identification 49
2.4.1 Estimation of the state-space matrices 49
2.4.2 Estimation of the safety factor profile 50
2.4.3 Estimation of the reference steady-state 51
2.5 Identification results 52
2.6 Conclusion on the identification approach 56
2.7 Conclusion of the chapter 57

The control-oriented model that was presented in the previous chapter is highly nonlinear and is complex for most of the control design methods. For a control design purpose, a linearized model can be successfully used in most cases. Linear models are easier to understand and allow us to use a large panel of control methods. Linearization involves creating a linear approximation of a nonlinear system that is valid in a neighbourhood around an equilibrium point. The equilibrium point is extracted from a steady-state condition. In this chapter two kinds of linearized models are presented. The first one is a so-called first-principle model that is derived by direct linearization of the model given analytically in the previous chapter. The other way to obtain a linearized model of the system is by using system identification techniques applied to measurement data. This approach does

not require an exact knowledge of the complex equations of the system. The parameters in the data-driven models are calculated by best fitting the outputs of the identified model with the measured data.

2.1 First-principle linearized model for control

In this section the control model is developed taking z and T_e as states of the system and their evolution is given by (1.26) and (1.22), respectively. The linearized model is obtained around equilibrium profiles $(\overline{z}, \overline{T}_e)$. The distributed inputs are represented by the power of the auxiliary heating sources and are presented with the notation $u(t)$ (see Section 1.5) and the ohmic heating comes from the boundary control input $I_p(t)$ given in (1.10). The equilibrium point is calculated by measuring the values of the plasma parameters when the constant inputs $(\overline{u}, \overline{I}_p)$ are applied, during a sufficiently long time, so that the system reaches a steady state. An equilibrium is defined as a stationary solution of (1.22) and (1.26) when $\frac{\partial z}{\partial t} = \frac{\partial T_e}{\partial t} = 0$:

$$\begin{cases} 0 = \dfrac{\partial}{\partial x}\left(\dfrac{\overline{\eta}_{\|}}{\mu_0 a^2 x}\dfrac{\partial}{\partial x}(x\overline{z})\right) + \dfrac{\partial}{\partial x}\left(\overline{\eta}_{\|} R_o(\overline{j}_{aux} + \overline{j}_{bs})\right) \\ 0 = \dfrac{1}{a^2}\dfrac{1}{x}\dfrac{\partial}{\partial x}(x n_e \overline{\chi}_e \dfrac{\partial \overline{T}_e}{\partial x}) + \overline{Q}_{OH} - \overline{Q}_{ei} - \overline{Q}_{rad} + \overline{Q}_{aux} \end{cases} \tag{2.1}$$

where:

$$\begin{aligned} \overline{\eta}_{||} &= \frac{k_{sp} Z_{eff}}{\overline{T}_e^{3/2}} \\ \overline{\chi}_e &= 2.510^{-4} \frac{\mid \bigtriangledown(\overline{T}_e n_e) \mid}{n_e} \frac{a^2 x}{\overline{z}}^2 \\ \overline{j}_{bs} &= \frac{k_{bs}}{\overline{z}}\left(\mathcal{L}_{31}\frac{\partial n_e}{\partial x}\overline{T}_e + \left(\mathcal{L}_{31} + R_{pe}\mathcal{L}_{32} + (1 - R_{pe})\mathcal{L}_{34}\right)\frac{\partial \overline{T}_e}{\partial x} n_e\right) \\ \overline{Q}_{rad} &= f_{rad}\overline{T}_e^{1/2} \\ \overline{Q}_{ei} &= f_{ei}\overline{T}_e \\ \overline{Q}_{OH} &= \frac{\overline{\eta}_{||}}{n_e \mu_0^2 R_0^2 a^3 x^2}\left(\frac{\partial}{\partial x}(x\overline{z})\right)^2 \end{aligned} \tag{2.2}$$

The linearized model is derived around the steady state with the change of variables:

$$\begin{aligned} z &= \overline{z} + \tilde{z} \\ T_e &= \overline{T}_e + \tilde{T}_e \\ u &= \overline{u} + \tilde{u} \\ I_p &= \overline{I}_p + \tilde{I}_p \end{aligned} \tag{2.3}$$

using Taylor series with first order approximation. Here $(\overline{z}, \overline{T}_e, \overline{u}, \overline{I}_p)$ denotes the equilibrium point of the system, and $(\tilde{z}, \tilde{T}_e, \tilde{u}, \tilde{I}_p)$ denotes incremental variations around this point.
The model is simplified additionally by considering the following assumptions:

- The electron density profile is constant during the heat process, $n_e = const$;
- The space variations of the electron density are neglected with respect to those of the temperature.

Under these assumptions, the simplified linearized coupled model coming from (2.1) and (2.2) is derived as:

$$\begin{cases} \dfrac{\partial \tilde{z}}{\partial t} = \dfrac{\partial}{\partial x}\left(\dfrac{a_1(x)}{x}\dfrac{\partial}{\partial x}(x\tilde{z})\right) + \dfrac{\partial}{\partial x}(a_2(x)\tilde{T}_e) \\ \qquad\qquad + \dfrac{\partial}{\partial x}\left(a_3(x)\dfrac{\partial \tilde{T}_e}{\partial x}\right) + \dfrac{\partial}{\partial x}\left(a_4(x)\tilde{z}\right) + \dfrac{\partial}{\partial x}\left(a_5(x)\tilde{j}_{aux}(\tilde{u}, x, t)\right) \\ \varepsilon\dfrac{\partial \tilde{T}_e}{\partial t} = \dfrac{1}{x}\dfrac{\partial}{\partial x}\left(xb_1(x)\dfrac{\partial \tilde{T}_e}{\partial x}\right) - b_2(x)\tilde{T}_e + \dfrac{1}{x}\dfrac{\partial}{\partial x}\left(xb_3(x)\tilde{z}\right) \\ \qquad\qquad + \dfrac{b_4(x)}{x}\left(\dfrac{\partial}{\partial x}(x\tilde{z})\right) + b_5(x)\tilde{Q}_{aux}(\tilde{u}, x, t) \end{cases} \tag{2.4}$$

with boundary conditions:

$$\begin{aligned} \tilde{z}(0,t) &= 0, \forall t \geq 0 \\ z(1,t) &= -\frac{R_o \mu_0 \tilde{I}_p(t)}{2\pi}, \forall t \geq 0 \\ \frac{\partial \tilde{T}_e}{\partial x}(0,t) &= 0, \forall t \geq 0 \\ \tilde{T}_e(1,t) &= \tilde{T}_{e,edge}, \forall t \geq 0 \end{aligned} \tag{2.5}$$

with initial conditions:

$$\tilde{z}(x,0) = \tilde{z}_0;\ \tilde{T}_e = \tilde{T}_{e,0}, \forall x \in [0,1] \tag{2.6}$$

where:

$$
\begin{aligned}
a_1(x) &= \frac{\overline{\eta}_{\|}}{\mu_0 a^2} \\
a_2(x) &= \frac{1}{\mu_0 a^2}\frac{\partial \overline{\eta}_{\|}}{\partial \overline{T}_e}\frac{\partial}{\partial x}(x(\overline{z})) + \frac{\partial \overline{\eta}}{\partial \overline{T}_e} R_0 \overline{j}_{ni} + \frac{\partial \overline{j}_{aux}}{\partial \overline{T}_e}\overline{\eta} R_0 + \overline{\eta}_{\|} R_0 \frac{k_{bs}}{\overline{z}}\left(\mathcal{L}_{31}\frac{\partial n_e}{\partial x}\right) \\
a_3(x) &= \overline{\eta}_{||} R_0 \frac{k_{bs}}{\overline{z}}\left(\mathcal{L}_{31} + R_{pe}\mathcal{L}_{32} + (1-R_{pe})\mathcal{L}_{34}\right) n_e \\
a_4(x) &= -\overline{\eta}_{||} R_0 \frac{k_{bs}}{\overline{z}^2}\left(\mathcal{L}_{31}\frac{\partial n_e}{\partial x}\overline{T}_e + \left(\mathcal{L}_{31} + R_{pe}\mathcal{L}_{32} + (1-R_{pe})\mathcal{L}_{34}\right)\frac{\partial \overline{T}_e}{\partial x} n_e\right) \\
a_5(x) &= \overline{\eta}_{||} R_0 \\
b_1(x) &= \frac{2\varepsilon}{3a^2}\left(\overline{\chi}_e + \frac{\partial \overline{T}_e}{\partial x}\frac{\partial \overline{\chi}_e}{\partial(\nabla \overline{T}_e)}\right) \\
b_2(x) &= -\frac{2\varepsilon}{3n_e}\left(f_{ei} + \frac{1}{2} f_{rad}\overline{T}_e^{-1/2} - \frac{4}{3}\frac{\frac{\partial \overline{\eta}_{||}}{\partial \overline{T}_e}}{n_e \mu_0^2 R_0^2 a^3 x^2}\left(\frac{\partial}{\partial x}(x\overline{z})\right)^2\right) \\
b_3(x) &= \frac{\varepsilon}{a^2}\frac{\partial \overline{\chi}_e}{\partial \overline{z}}\frac{\partial \overline{T}_e}{\partial x} \\
b_4(x) &= \frac{4\varepsilon}{3}\frac{\overline{\eta}_{\|}}{n_e \mu_0^2 R_0^2 a^3 x}\left(\frac{\partial}{\partial x}(x\overline{z})\right) \\
b_5(x) &= \frac{2\varepsilon}{3n_e}
\end{aligned}
\tag{2.7}
$$

In this model ε stands for the typical ratio between the energy confinement time and the characteristic resistive diffusion time. This parameter varies with the size of the different tokamak machines. In a large tokamak such as ITER this parameter is indeed small ($\varepsilon \approx 0.01$), that makes the scales of the dynamics of the states to be very different. The analysis of such systems is achieved with the help of the singular perturbation theory.

2.2 Data-driven model for control

The data-driven model in this section is obtained using system identification techniques that are trying to estimate a gray box model of a dynamic system based on observing input-output from experimental data. The model is based only on data without requiring exact previous knowledge of the dynamics. Thus, an exact knowledge of the physics of the system is not required. In comparison with the nonlinear models used in plasma simulators, the model obtained by system identification is linear and fast, and does not require an accurate knowledge of all the parameters that would be required in a first-principle model. The identified system is obtained in state-space form that is the most suitable for

control design. The simplicity and generality of the system identification approach makes the technique easily adaptable to other tokamak machines with different parameters and different inputs. The identified model represents the dynamics of the kinetic and the magnetic states of the plasma combined in one system. Data-driven LTI models of coupled magnetic and kinetic parameters already have been developed in (Moreau et al., 2008; Moreau et al., 2011). Here the structure of the models is based on a singular perturbation approximation that took advantage of the large ratio between the time scales involved in the magnetic and kinetic diffusion processes. Such two-time-scale models consist of a slow model and a fast model, with their respective sets of eigenvalues and eigenfunctions that were identified separately using an output-error identification scheme. In the present work, the two-time-scale approximation is not used so the system is more complex and could, in principle, be more accurate for certain tokamak machines. In order to identify a large order MIMO system that could lead to improved accuracy with respect to the previous works, a combination of a subspace identification method and output-error identification methods is used in this thesis. The subspace identification is a powerful method for state-space identification of MIMO systems (Katayama, 2006; Ljung, 1998; Verhaegen and Dewilde, 1992; Di Ruscio, 1997).
The identification is performed using data provided by the METIS code, a fast integrated tokamak simulation tool for the CRONOS suite. The METIS code is designed as a fast tokamak simulator implemented in MATLAB ®. These data sets simulate plasma discharges and the identification method can be tested. Here a nonlinear simulator is used to simulate the plasma evolution in DIII-D tokamak.

2.2.1 Problem statement and identification procedure

In tokamaks, the poloidal flux does not reach a stationary value even when the loop voltage and the auxiliary power are kept constant. In fact, at the plasma edge, we have $V_{ext} = -\partial\Psi(1,t)/\partial t$ and it is this linear flux variation that induces the ohmic current in the plasma. Following reference (Moreau et al., 2008), the following transformation is introduced: $\Psi_r(x,t) = \Psi(x,t) - \Psi(1,t)$, so that the state that is going to be used for the identification is the internal poloidal flux $\Psi_r(x,t)$. This variable can indeed be used as a state variable of the system and is even a natural state variable for the identification of this system. It is directly related to the safety factor profile and can therefore be used for its control. The state equation for the internal poloidal flux is given by (1.29). It has a stable dynamics and it can be linearized and used for the system identification procedure. The identified model should represent the dynamics of the variations of $\Psi_r(x,t)$ and $T_e(x,t)$ around the reference values, $\overline{\Psi}_r$ and $\overline{T}_e$, subject to variations of $P(t)$ and V_{ext} around the

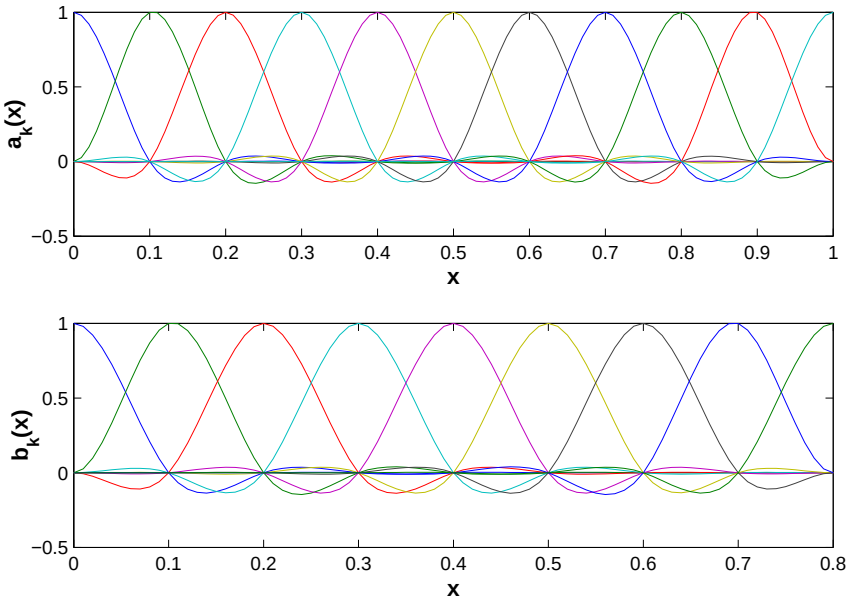


Figure 2.1: Cubic splines $a_k(x)$ used for the expansion of Ψ_r, and $b_k(x)$ used for the expansion of T_e.

reference values $\overline{P}$ and $\overline{V}_{ext}$. Therefore let us define:

$$\begin{aligned}
\tilde{\Psi}_r(x,t) &= \Psi_r(x,t) - \overline{\Psi}_r(x) \\
\tilde{T}_e(x,t) &= T_e(x,t) - \overline{T}_e(x) \\
\tilde{P}(t) &= P(t) - \overline{P}(x) \\
\tilde{V}_{ext}(t) &= V_{ext}(t) - \overline{V}_{ext}(x)
\end{aligned} \tag{2.8}$$

where the input $P(t)$ represents the power of the heating and current drive systems e.g.:

$$P(t) = \begin{bmatrix} P_{NBI1}(t) \\ P_{NBI2}(t) \\ P_{ECCD}(t) \end{bmatrix} \tag{2.9}$$

The first actuators that are used in this case are two deuterium neutral beam injectors: an off-axis co-current NBI power P_{NBI1} and an on-axis co-current NBI power P_{NBI2}. The other two inputs are the power of electron cyclotron current drive system (ECCD) P_{ECCD} and the loop voltage at the plasma surface $V_{ext}(t)$.

The output data of METIS simulator are interpolated on a unique radial grid for each parameter profile through a cubic-splines Galerkin approximation. The distributed profile system is represented as a lumped parameter system using the Galerkin projection to

represent the finite developments (e.g. see (Moreau et al., 2008)) as:

$$\Psi_r(x,t) = \sum_{k=1}^{n_\Psi} \Psi_{rk}(t) a_k(x) \tag{2.10}$$

$$T_e(x,t) = \sum_{k=1}^{n_T} T_{ek}(t) b_k(x) \tag{2.11}$$

where a_k and b_k are cubic splines for the magnetic profile and piecewise linear functions for the temperature profile, respectively (see Fig. 2.1 for a plot of these functions). For the spatial discretization of $\Psi_r(x,t)$, 11 spline functions ($n_\Psi = 11$) were used at radial knots $x = 0, 0.1, 0.2, \ldots, 1$, and for the spatial discretization of $T_e(x,t)$, 9 spline functions ($n_T = 9$) were used at radial knots $x = 0, 0.1, 0.2, \ldots, 0.8$.
Based on the structure of thie model (1.29) and (1.16) and flux-averaged plasma transport equations, a linearized gray-box model of system can be postulated in the form (Moreau et al., 2008; Moreau et al., 2011):

$$\begin{aligned} \dot{\tilde{\Psi}}_r(t) &= A_{11}\tilde{\Psi}_r(t) + A_{12}\tilde{T}_e(t) + B_{\Psi,P}\tilde{P}(t) + B_{\Psi,V}\cdot\tilde{V}_{ext}(t) \\ \dot{\tilde{T}}_e(t) &= A_{21}\tilde{\Psi}_r(t) + A_{22}\tilde{T}_e(t) + B_{T_e,P}\tilde{P}(t) \end{aligned} \tag{2.12}$$

where $\tilde{\Psi}_r(t) = [\tilde{\Psi}_{r1}(t), \tilde{\Psi}_{r2}(t), .., \tilde{\Psi}_{rn_\Psi}(t)]^T$ and $\tilde{T}_e(t) = [\tilde{T}_{e1}(t), \tilde{T}_{e2}(t), .., \tilde{T}_{en_T}(t)]^T$ are the state vectors representing the sets of the Galerkin coefficients of $\Psi_r(x,t)$ and $T_e(x,t)$, respectively.

This model is a lumped-parameter state-space mathematical model of the physical system, with a set of state variables $\tilde{\Psi}_r \in \mathbb{R}^{n_\Psi}$ and $\tilde{T}_e \in \mathbb{R}^{n_T}$ and inputs $\tilde{P} \in \mathbb{R}^3$ and V_{ext}. The matrices $A_{11} \in \mathbb{R}^{n_\Psi \times n_\Psi}$, $A_{12} \in \mathbb{R}^{n_\Psi \times n_T}$, $A_{21} \in \mathbb{R}^{n_T \times n_\Psi}$ and $A_{22} \in \mathbb{R}^{n_T \times n_T}$ are state matrices and $B_{\Psi,P} \in \mathbb{R}^{n_\Psi \times 3}$, $B_{\Psi,V} \in \mathbb{R}^{n_\Psi}$ and $B_{T_e,P} \in \mathbb{R}^{n_T \times 3}$ are input matrices to be identified. In fact, the matrix $B_{\Psi,V}$ in front of V_{ext} does not need to be identified, since it is known from the derivation of the matrix structure of the system in (Moreau et al., 2008). The idea for the control is to reach the desired equilibrium values of the safety factor by using only a limited number of actuators. Note that this choice of actuators can easily be modified and the identification method holds for any set of known inputs.
This model writes in the standard state-space form by defining $\tilde{X}(t) = [\tilde{\Psi}_{rk}^T(t)\ \tilde{T}_{ek}^T]^T$ and $\tilde{U}(t) = [\tilde{P}^T(t)\ \tilde{V}_{ext}(t)]^T$

$$\dot{\tilde{X}}(t) = A\tilde{X}(t) + B\tilde{U}(t) \tag{2.13}$$

with:

$$A = \begin{bmatrix} A_{11} & A_{12} \\ A_{21} & A_{22} \end{bmatrix} \text{ and } B = \begin{bmatrix} B_P B_V \end{bmatrix} = \begin{bmatrix} B_{\Psi,P} & B_{\Psi,V} \\ B_{T_e,P} & 0 \end{bmatrix} \tag{2.14}$$

Assuming a temporal discretization with time step Δt, at time stamps $[t_1, t_2, .., t_N]$ where $t_N = t_1 + (N-1)\Delta t$, with the corresponding discrete-time data $[U_1, U_2, .., U_N]$ and $[X_1, X_2, .., X_N]$

sampled from the continuous-time dynamics (2.13), and applying zero-order hold on the inputs, the discrete system is then obtained as:

$$\tilde{X}(t+1) = A_d\tilde{X}(t) + B_d\tilde{U}(t) \tag{2.15}$$

where

$$A_d = e^{A\Delta t}, \quad B_d = \int_0^{\Delta t} e^{A\tau}Bd\tau \tag{2.16}$$

The inverse of the safety factor can be considered as an output of the system. It depends only on the plasma parameters and geometry, and not explicitly on the heating and current drive power. Its linearized relation with the states of the system can be represented by:

$$\tilde{\iota}(t) = C_\iota \cdot \begin{bmatrix} \tilde{\Psi}_r(t) \\ \tilde{T}_e(t) \end{bmatrix} \tag{2.17}$$

The data collected for the identification were obtained from nonlinear plasma simulations, using the METIS code. METIS is a rapidly converging module of the CRONOS plasma transport code (Artaud et al., 2010), which includes an MHD equilibrium and current diffusion solver, and combines plasma transport nonlinearity with 0-D scaling laws and 1.5-D ordinary differential equations. Despite its simplicity, it integrates basically all the complex features of real tokamak physics in a simplified but comprehensive and flexible way. The complexity of tokamak physics is restored through the very large number of possible options and models that the code offers for every elementary physical process (e.g. scaling laws, or fixing some source or parameter profiles and evolving others, etc.).
The simulation data were divided in two sets: one for identification and another for the validation of the identified system. For the validation of the MIMO system, the measurements from the outputs of the simulated system were compared with the original data obtained from the non-linear METIS simulator. For each output, the normalized root-mean-square error (NRMSE) fit value is calculated as:

$$fit_i(\%) = 100 * \left(1 - \frac{\parallel y_i(t) - \widehat{y}_i(t) \parallel}{\parallel y_i(t) - \langle y \rangle_i \parallel}\right)\% \tag{2.18}$$

where y is the original data, $\widehat{y}$ is the estimated outputs of the model, $\langle y \rangle$ represents the mean value of the output and i represents the index of the output.

2.2.1.1 Overview of the identification method

Equations (2.12)-(2.17) represent a grey-box model where most of the dynamics of the system is unknown and only the value of the matrix $B_{\Psi,V}$ is known from the linearization and

the discretization of (1.29) as shown in (Moreau et al., 2008). For the identification of this state-space model, a combination of two identification methods is used based on the procedure proposed in (Haverkamp, 2000; Verhaegen and Verdult, 2007). First a Multivariable Output Error State sPace (MOESP) method (Verhaegen and Dewilde, 1992) is applied. The model obtained by the MOESP method is not optimal when the input signals are short (Suleiman and Monin, 2007) and due to the complexity of the system, but it can be used to initialize the model for the recursive Output-Error (OE) method. A combination of subspace and recursive least-square methods has been already used in identification of MIMO state-space models (Verhaegen and Verdult, 2007). The MOESP method is also very useful to determine the order of the system to be identified. The recursive OE method initialized with the previously identified system gives a more accurate identification of the system dynamics. Before the identification, the data must be pre-processed by removing the means from the inputs and the outputs, and the original system must be transformed, through simple algebra, into a system for the zero-mean pre-processed data.
Along with the identification methods, some constraints on the eigenvalues of the system can also be introduced to reflect specific properties of the physical system. The identification cycle is presented on Fig. 2.2.

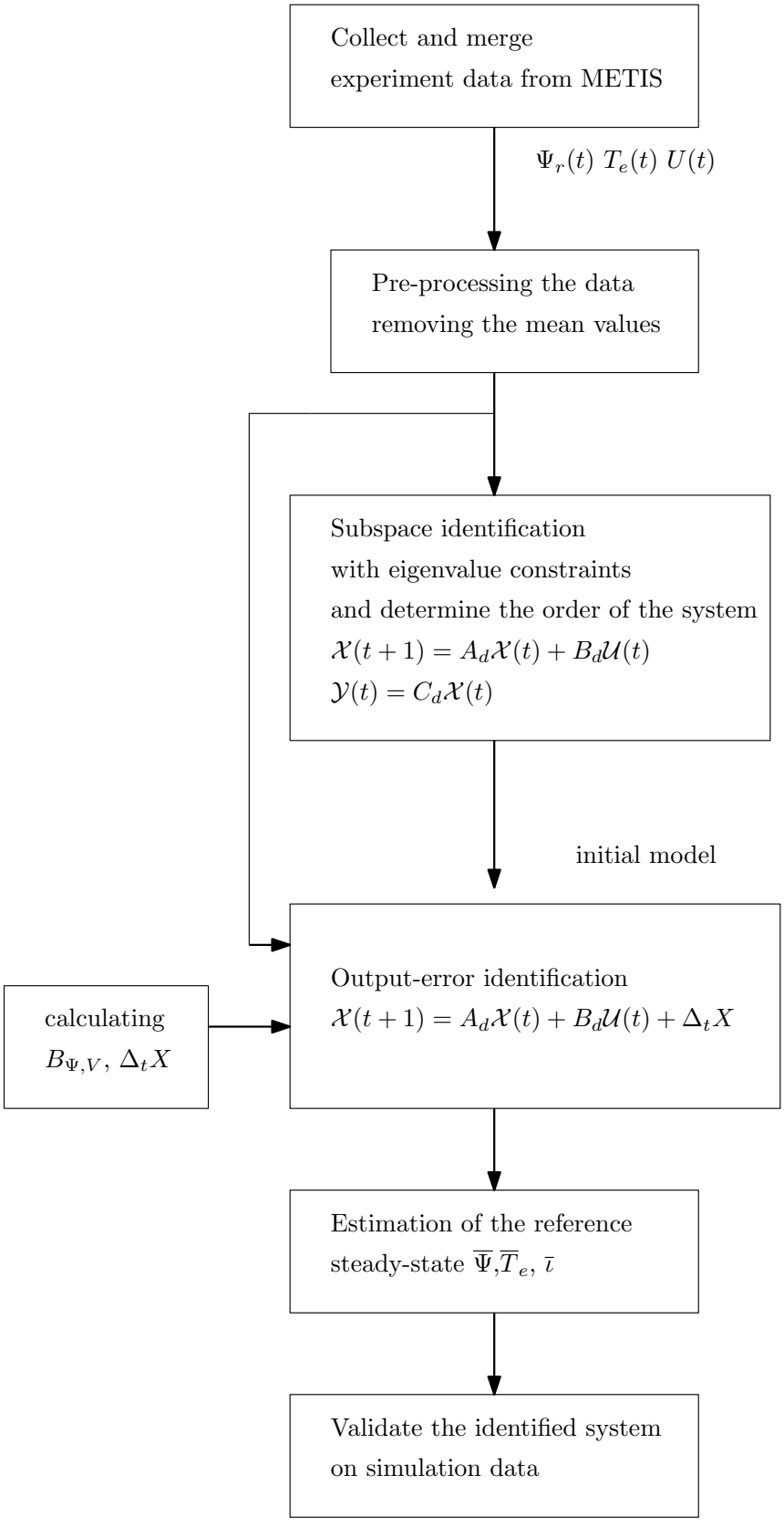


Figure 2.2: Overview of the method.

2.2.2 Pre-processing the data for system identification

The data that are used for estimation should be pre-processed by removing the offsets before the identification (e.g. see Chapter 14 in (Ljung, 1998)). Processed data describe the relationship between the change in input signals and the change in output signals. The pre-processing operation helps to estimate more accurately linear models because the linear models identification methods cannot capture arbitrary differences between the input and output signal levels. One way of removing the offsets in the data is by removing from the system variables the reference values corresponding to steady state equilibrium around which the system has been linearized, as it was done, for example, in Equation (2.8). The reference values corresponding to a given set of steady inputs could be known in the case where the so-called experimental data is obtained from non-linear plasma simulators because the simulations could in principle be extended until the plasma reaches an equilibrium. This is not the case, however, if one uses real experimental data because, in most tokamaks, the plasma does not reach a physical equilibrium state before the end of the discharge even with steady inputs, so the measurements that can be used for system identification consist only of transient data. For the sake of generality, it shall be assumed that the reference values are not known *a priori*, and use a technique to identify them. To bring the data near the linearization point, the data are pre-processed by removing the mean values:

$$\begin{aligned} \mathcal{X}(t) &= X(t) - \langle X \rangle \\ \mathcal{P}(t) &= P(t) - \langle P \rangle \\ \mathcal{V}_{ext}(t) &= V_{ext}(t) - \langle V_{ext} \rangle \end{aligned} \tag{2.19}$$

where $\langle X \rangle = [\langle \Psi_r \rangle^T \ \langle T_e \rangle^T]^T$, $\langle P \rangle$ and $\langle V_{ext} \rangle$ are the mean values of the measured vectors. The model corresponding to the model of the zero-mean data is:

$$\begin{aligned} \dot{X}(t) = \dot{\mathcal{X}}(t) &= A(\mathcal{X}(t) + \langle X \rangle) + B(\mathcal{U}(t) + \langle U \rangle) \\ &= A\mathcal{X}(t) + B\mathcal{U}(t) + \Delta_t X \end{aligned} \tag{2.20}$$

where

$$\begin{aligned} \Delta_t X &= A \langle X \rangle + B \langle U \rangle \\ &= A \frac{1}{t_N - t_1} \int_{t_1}^{t_N} X(t)dt + B \frac{1}{t_N - t_1} \int_{t_1}^{t_N} U(t)dt \\ &= \frac{1}{t_N - t_1} \int_{t_1}^{t_N} \dot{X}(t)dt = \frac{X(t_N) - X(t_1)}{t_N - t_1} \end{aligned} \tag{2.21}$$

The term $\Delta_t X$ represents an offset that should be considered when the identification is performed. If the full state is measured and there is no measurement noise (as in this case), the values of $\Delta_t X_j$ are known and can be calculated for each different measurement data set X_j represented by $\Psi_r(t)$ and $T_e(t)$.

In the black-box subspace based algorithms or in the case where there is a measurement noise in the data, this offset should be estimated considering a constant input to the system as in (Bauer, 2000). In identification procedures as the output-error method, the system can be presented in a specific form where $\Delta_t X_j$ can be introduced as an additional input of the system.

2.3 Subspace identification

2.3.1 MOESP method for system identification

The simulations consist of multiple short input/output data sets. In the different reference sets, the inputs of the MIMO system are modulated in order to have a better estimation of the dynamics of the system for each input/output channel. Thus, linear-multivariable system identification techniques are used where the multi-experiment data are merged together for one identification cycle. Techniques dealing with multiple data sets in subspace identification methods are presented in (Duchesne et al., 1996; Suleiman and Monin, 2007). Here the extension is done in a similar way for the MOESP method. The subspace method is used to find an initial system, i.e. approximations for the elements in the A_d, B_d and C_d matrices, which will be used as initial values for the recursive output-error identification. The identified system using the subspace identification method is given by the discrete-time LTI system

$$\begin{aligned} \mathcal{X}(t+1) &= A_d\mathcal{X}(t) + B_{d,e}\mathcal{U}(t) \\ \mathcal{Y}(t) &= C_d\mathcal{X}(t) \end{aligned} \tag{2.22}$$

where $A_d \in \mathbb{R}^{n\times n}$, where $n = n_\Psi + n_T$ is the state matrix, $B_{d,e} = [B_P\ B_V\ B_\delta] \in \mathbb{R}^{n\times 5}$ is the input matrix and $C_d \in \mathbb{R}^{n_y\times n}$ is the output matrix of the discrete system. In these experiments the input data is $\mathcal{U}(t) = \left[P^T(t)\ V_{ext}(t)\ 1\right]^T$. The output data are combined as: $\mathcal{Y}(t) = \left[\Psi_r^T(t)\ T_e^T(t)\right]^T$. Here the matrix B_δ is added to deal with the additional constant input that should identify the offset that is obtained due to the pre-processing of the data. First, the output and input data are stored in Hankel matrices noted as $\mathcal{Y}_{1,k,N}$ and $\mathcal{U}_{1,k,N}$, respectively. The input Hankel matrix is presented as:

$$\mathcal{U}_{1,k,N} \triangleq \begin{bmatrix} \mathcal{U}(1) & \mathcal{U}(2) & \cdots & \mathcal{U}(N-k+1) \\ \mathcal{U}(2) & \mathcal{U}(3) & \cdots & \mathcal{U}(N-k+2) \\ \vdots & \vdots & \ddots & \vdots \\ \mathcal{U}(k) & \mathcal{U}(k+1) & \cdots & \mathcal{U}(N) \end{bmatrix} \tag{2.23}$$

where the subscript 1 is the index of the first data sample and k denotes the number of rows in the matrix. N represents the last data sample of the experiment. The output

Hankel matrix is calculated in the same way.
Given $1 \dots N$ measurements of the input, the output of the system can be written using recursive substitution as follows:

$$\begin{aligned}
\mathcal{Y}(1) &= C_d \mathcal{X}(1) \\
\mathcal{Y}(2) &= C_d X(2) = C_d A_d \mathcal{X}(1) + C_d B_d \mathcal{U}(1) \\
&\vdots \\
\mathcal{Y}(N) &= C_d A_d^K \mathcal{X}(1) + C_d A_d^{N-1} B_d \mathcal{U}(1) + \ldots + C_d B_d \mathcal{U}(N-1)
\end{aligned} \tag{2.24}$$

Using this extension, the system can be cast into a special matrix form called data equation. The data equation in this work is extended to deal with multiple data sets that are merged together as in (Suleiman and Monin, 2007). The input-output data equation is defined in condensed form as:

$$\begin{aligned}
[\mathcal{Y}_{1,k,N_1} \mid \cdots \mid \mathcal{Y}_{1,k,N_K}] =& \Gamma_k [\mathcal{X}_{1,N_1-k+1} \mid \cdots \mid \mathcal{X}_{1,N_K-k+1}] \\
&+ \Phi_k [\mathcal{U}_{1,k,N_1} \mid \cdots \mid \mathcal{U}_{1,k,N_K}]
\end{aligned} \tag{2.25}$$

where K is the total number of experiments in the merged database. The matrices Γ_k and Φ_k in this equation are called the extended observability matrix and the block Toeplitz matrix, respectively and are defined as (Di Ruscio, 1997):

$$\Gamma_k = \begin{bmatrix} C_d \\ C_d A_d \\ \vdots \\ C_d A_d^{k-1} \end{bmatrix}$$

$$\Phi_k = \begin{bmatrix} 0 & 0 & \cdots & 0 \\ C_d B_d & 0 & \cdots & 0 \\ \vdots & \vdots & \ddots & \vdots \\ C_d A_d^{(k-2)} B_d & C_d A_d^{(k-3)} B_d & \cdots & C_d B_d \end{bmatrix}$$

The row-vector is constructed from the states $\mathcal{X}(t)$ where the first subscript denotes the starting index and the second subscript the length of the vector:
$\mathcal{X}_{1,N-k+1} = \big[\mathcal{X}(1)\ \mathcal{X}(2)\ \cdots\ \mathcal{X}(N-k+1)\big]$.
The LQ decomposition (where L is a lower triangular matrix) of the data matrix for the MOESP method can be obtained as:

$$\begin{bmatrix} \mathcal{U}_{1,k,N_1} \mid \mathcal{U}_{1,k,N_2} \mid \cdots \mid \mathcal{U}_{1,k,N_K} \\ \mathcal{Y}_{1,k,N_1} \mid \mathcal{Y}_{1,k,N_2} \mid \cdots \mid \mathcal{Y}_{1,k,N_K} \end{bmatrix} = \begin{bmatrix} L_{11} & 0 \\ L_{21} & L_{22} \end{bmatrix} \begin{bmatrix} Q_1^T \\ Q_2^T \end{bmatrix} \tag{2.26}$$

Thus, (2.26) can be written as

$$\begin{aligned}
[\mathcal{U}_{1,k,N_1} \mid \mathcal{U}_{1,k,N_2} \mid \cdots \mid \mathcal{U}_{1,k,N_K}] &= L_{11} Q_1^T \\
[\mathcal{Y}_{1,k,N_1} \mid \mathcal{Y}_{1,k,N_2} \mid \cdots \mid \mathcal{Y}_{1,k,N_K}] &= L_{21} Q_1^T + L_{22} Q_2^T
\end{aligned} \tag{2.27}$$

The calculation of L_{22} by combining (2.25) and (2.27) is fully explained in (Katayama, 2006) and the result can be written as:

$$L_{22} = \Gamma_k[\mathcal{X}_{1,N_1-k+1}...\mathcal{X}_{1,N_K-k+1}]Q_2 \tag{2.28}$$

2.3.2 Determining the order of the system

By performing a singular value decomposition (SVD) on L_{22}, we get

$$L_{22} = W\Sigma V^T$$

where Σ is a diagonal matrix with singular values of L_{22} on its diagonal, the columns of W are the left singular vectors and V^T has rows that are the right singular vectors obtained by SVD. Examining the elements of the rectangular diagonal matrix with non-negative real numbers Σ, a decision about the choice of the order of the system can be made. The order of the system can in principle be obtained by reducing Σ to the first n elements with highest values, $\Sigma_1 = diag[\sigma_1,\ \sigma_2,\ ...\ ,\sigma_n]$, where $\sigma_1 \geq \sigma_2 \geq ... \geq \sigma_n > 0 \approx \sigma_{n+1} \approx \sigma_{n+2}...$
The decision about the order of the system using subspace methods is heuristic. The order of the system, n should be taken such that the values of the eliminated elements of Σ are zero or close to zero. L_{22} can thus be approximated as:

$$L_{22} \simeq \begin{bmatrix} W_1\ W_2 \end{bmatrix} \begin{bmatrix} \Sigma_1 & 0 \\ 0 & 0 \end{bmatrix} \begin{bmatrix} V_1^T \\ V_2^T \end{bmatrix} = W_1\Sigma_1 V_1^T$$

In the case of this system, Σ was calculated by taking as outputs all the 20 available measured outputs for $\Psi_r(x,t)$ and $T_e(x,t)$ at 11 and 9 radial points, respectively. The first 10 singular values are presented in Fig. 2.3. From the singular values it can be concluded that the system can be well represented if the order is taken to be $n \geq 4$. Another criterion that limits the order of the system is that the characteristic times of all the identified eigenmodes should be larger than the sampling time. In addition, the controlled system has only a few degrees of freedom because there are only 4 available actuators. For the sake of simplicity, the order of the system and the number of controlled outputs is restricted to a maximum of $n = n_y = 8$, so that the number of outputs in the system to be identified is equal to the order of the system. Thus, for the outputs of the system, 4 outputs were taken for the poloidal magnetic flux and 4 outputs for the electron temperature in particular radii that are important for profile control. This reduction of the number of outputs used for the identification simplifies the identification process and reduces the number of parameters that need to be estimated.
Once the order of the system has been selected, an estimate of the extended observability matrix is calculated taking only the first 8 singular values as:

$$\widehat{\Gamma}_k = W_1\Sigma_1^{1/2}$$

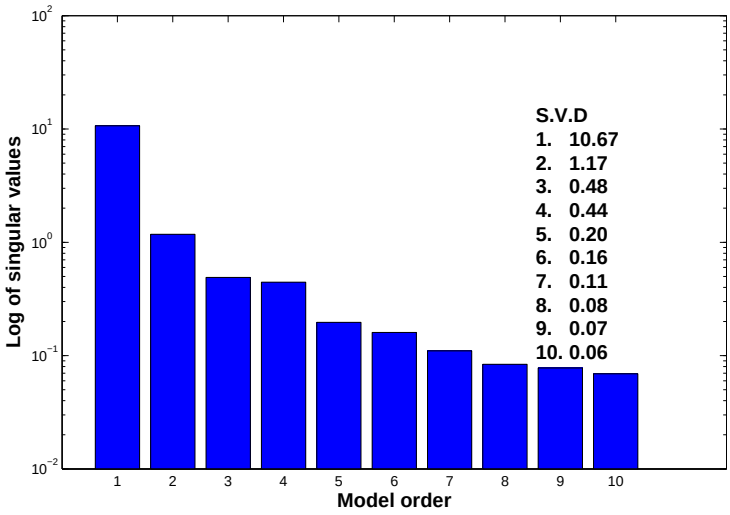


Figure 2.3: First 10 singular values of Σ that indicate the order of the model.

2.3.3 Eigenvalues constraints in subspace identification

The initial estimate of $\hat{A}_d$ using the MOESP method is given by minimizing the cost function

$$J_\Gamma(A_d) = \| \widehat{\Gamma}_0 A_d - \widehat{\Gamma}_1 \|_F \tag{2.29}$$

where $\widehat{\Gamma}_0 = \widehat{\Gamma}_k(1 : n_y(k-1), :)$ and $\widehat{\Gamma}_1 = \widehat{\Gamma}_k(n_y + 1 : n_y k, :)$. Here $\widehat{\Gamma}_k(i : j; :)$ stands for the submatrix of $\widehat{\Gamma}_k$ which contains the columns from i-th to j-th columns. $\| \cdot \|_F$ denotes the Frobenius matrix norm. The solution of this linear least-squares problem with the analytic minimum is $\widehat{A}_d = \widehat{\Gamma}_0^{-1}\widehat{\Gamma}_1$. Some of the poles of $\widehat{A}_d$ obtained from (2.29) may be complex-conjugate, which may cause oscillations in the identified system response. The physical system is diffusive and the differential operator of the diffusion equation with constant diffusion coefficient is Hermitian (Ramos, 1987), thus with real eigenvalues. Moreover the experimental observation does not show oscillations in the data. For these reasons the eigenvalues are constraint in an arbitrary small band close to the real axis. As we shall see later, the systems identified within this constraint yield satisfactory simulations of the original data, so there was no real need for introducing complex-conjugate eigenvalues.
The technique of eigenvalue constraints for system identification that is used in this work is elaborated in (Miller and De Callafon, 2013). Using this method the eigenvalues can be constrained by defining linear matrix inequalities (LMI) regions and incorporating them into the subspace identification problem. The LMI-regions define convex regions of the complex plane as LMIs.

An LMI region is a convex region $\mathcal{D}$ of the complex plane, defined in terms of a sym-

metric matrix α and a square matrix β, as:

$$\mathcal{D} = \{z \in \mathbb{C} : f_{\mathcal{D}}(z) \geq 0\} \tag{2.30}$$

where

$$f_{\mathcal{D}}(z) = \alpha + \beta z + \beta^T \overline{z} \tag{2.31}$$

where $\overline{z}$ is complex conjugate of z. The concept of LMI regions is first introduced in (Chilali and Gahinet, 1996) and they are suitable for LMI-based synthesis. The central theorem in (Chilali and Gahinet, 1996) is the following:

Theorem 1
The eigenvalues of a matrix $\mathcal{A} \in \mathbb{R}^{n\times n}$ lie within an LMI region given by (2.30) if and only if there exists a matrix $N \in \mathbb{R}^{n\times n}$ such that:

$$N = N^T > 0, \quad \alpha \otimes N + \beta \otimes (\mathcal{A}N) + \beta^T \otimes (\mathcal{A}N)^T \geq 0 \tag{2.32}$$

The concept of constraints based on LMI regions is incorporated in the subspace identification problems into methods based on the extended observability matrix (Miller and De Callafon, 2013).

In order to get a modified model that consists only of real eigenvalues, the cost function (2.29) should be modified as:

$$J_\Gamma(M, N) = \| \widehat{\Gamma}_0 A_d N - \widehat{\Gamma}_1 N \|_F = \| \widehat{\Gamma}_0 M - \widehat{\Gamma}_1 N \|_F \tag{2.33}$$

where N is a right-hand weighting matrix and $M = A_d N$. The optimization problem with convex constraints is stated as follows:
Given the estimate of the extended observability matrix $\widehat{\Gamma}$ and the LMI region described by parameters α and β,

$$\begin{aligned} & \min\ J_\Gamma(M, N) \\ \text{subject to :}\ & \alpha \otimes N + \beta \otimes M + \beta^T \otimes M^T \geq 0\ ; \\ & N = N^T > 0 \end{aligned} \tag{2.34}$$

with:

$$\beta = \begin{bmatrix} 0 & 1 \\ -1 & 0 \end{bmatrix} \tag{2.35}$$

where $\alpha = 2\delta$ is a small number that limits the imaginary part of the poles $p \in \mathbb{C}$ of the identified system into an arbitrary small band around the real axis in the complex plane represented by the set $\mathcal{R} = \{p \in \mathbb{C} :\ |Im(p)| \leq \delta,\ \delta \geq 0\}$. Once M and N have been found, the new estimate is calculated as: $\hat{A}_d = MN^{-1}$. The convex optimization problem is solved using the YALMIP toolbox for MATLAB (Löfberg, 2004). The matrices C_d and B_d were obtained using the standard MOESP method (Katayama, 2006).

This identification method is not always sufficient for large MIMO systems. As will be seen in Section 2.4, the model obtained by the MOESP for the problem discussed here yields relatively big fitting errors when comparing the simulated outputs with the original data. However, this method provides a good guess for initializing the system. We have therefore used this model as a starting point for an iterative process in which the order of the system is fixed and the model matrices are optimized in each iteration by performing an output-error identification.

2.4 Output-error identification

2.4.1 Estimation of the state-space matrices

The output-error method is an iterative method (Verhaegen and Verdult, 2007) and requires initial values of the parameters that are estimated. The subspace identification method presented in Section 2.3 provides an initial model of the system. The model identified with the subspace method can be easily transformed in a form such that the output matrix C_d is an identity matrix $C_d = I_{n_y}$. This representation of the state space model is called an observable canonical form. It can be used when there is a direct measurement of the states $\mathcal{Y} = \mathcal{X}$ and the data can easily be pre-processed as explained in Subsection 2.2.2. We also introduce the known values of the matrices $B_{\Psi,V}$ and $\Delta_t X$ at this stage. Representing the system in this form avoids the need to identify the output matrix C, which reduces the number of parameters that needs to be estimated.
Using an iterative method the vector $\theta_1 = \left[vec(A)\ vec(B_P)\right]^T$, that contains all the unknown matrices A and B_p, is estimated by minimizing the squared error between the measured states $\mathcal{X}$ and the estimated $\hat{\mathcal{X}}$

$$\min\ J_K(\theta_1) \tag{2.36}$$

$$\begin{aligned} J_K(\theta_1) =& \frac{1}{K}\sum_{i=1}^{K}\frac{1}{N_i}\sum_{j=1}^{N_i}\left\|\mathcal{X}_i(t_j) - \hat{\mathcal{X}}_i(t_j,\theta_1)\right\|_2^2 \\ =& \frac{1}{K}E_K(\theta_1)^T E_K(\theta_1) \end{aligned} \tag{2.37}$$

where:

$$E_K(\theta_1) = \left[E^1_{N_1}(\theta_1)^T\ E^2_{N_2}(\theta_1)^T\ \cdots\ E^K_{N_K}(\theta_1)^T\right]^T \tag{2.38}$$

and

$$E^i_{N_i}(\theta_1) = \frac{1}{\sqrt{N_i}}\left[e^i(1)^T\ e^i(2)^T\ \cdots\ e^i(N_i)^T\right]^T \tag{2.39}$$

is the error vector where $e^i(j) = \mathcal{X}_i(t_j) - \hat{\mathcal{X}}_i(t_j,\theta_1)$.
As in the subspace identification approach (see Section 2.3), the output-error method

is set for a multi-experiment data set, where experiments with different modulations of the inputs are merged for a better estimation of the dynamics of the MIMO system. In this application, multiple-cost approach Leith, Murray-Smith, and Bradley, 1993; Ljung, 1998 is used for the definition of the cost function (2.36) to combine multiple experiments. For identification, there are the measured values of the set: $\{\mathcal{U}_{j,i}, \mathcal{X}_{j,i}\}$ with $j = 1, 2, \ldots, N_i$ and $i = 1, 2, \ldots, K$ (K denotes the number of experiments and N_i is the number of data samples in the i-th experiment).
The estimated state and initial condition are given by

$$\begin{aligned} \hat{\mathcal{X}}_j(t+1, \hat{\theta}_1) &= A_d(\hat{\theta}_1)\hat{\mathcal{X}}_j(t, \hat{\theta}_1) + B_{d,e}(\hat{\theta}_1)\mathcal{U}_e(t) \\ \hat{\mathcal{X}}_j(0) &= \mathcal{X}_j(0) \end{aligned} \tag{2.40}$$

where the inputs are combined in one vector $\mathcal{U}_e(t) = \begin{bmatrix}\mathcal{P}(t)\ \mathcal{V}_{ext}(t)\ 1\end{bmatrix}^T$ and the matrix $B_{d,e} = \int_0^{\Delta t} e^{A\tau} B_e d\tau$ where $B_e = \begin{bmatrix}B_p\ B_v\ \Delta_t X_j\end{bmatrix}$. The estimate (2.40) is presented in a discrete form with a discretization time equal to the sampling time of the experiments, $\Delta t = 5ms$.

Using the estimate in (2.40), the minimization of (2.37) can be performed by using a recursive gradient search method. The initial value of θ_1 for the optimization is the one obtained previously with the MOESP method. In Fig. 2.4 the comparison between the outputs of the identified systems with MOESP and output error methods for $\tilde{\Psi}_r$ and $\tilde{T}_e$ are presented for a particular experiment. From the plots it can be easily noticed that the results, obtained using only the MOESP subspace method, are not satisfactory due to the low NRMSE fit value of the compared outputs. Applying an additional optimization to the model using the output-error method, improves the performance of the identified system.

2.4.2 Estimation of the safety factor profile

In order to formulate the control objectives generally in terms of the safety factor or its inverse, a change of variable is necessary to convert Ψ_r into the controlled variable. For example, the relation between $\iota(x,t)$ and $\Psi_r(x,t)$ can be written as in (Moreau et al., 2011):

$$\begin{aligned} \iota(x,t) &= -\left(\frac{\partial \Psi_r(x,t)}{\partial x}\right)\left(\frac{\partial x}{\partial \Phi(x,t)}\right) \\ &= -\frac{1}{2\Phi_{max}(t)}\left(\frac{1}{x}\frac{\partial \Psi_r(x,t)}{\partial x}\right) \end{aligned} \tag{2.41}$$

where the normalized radius is defined as $x = (\Phi/\Phi_{max})^{1/2}$ and $\Phi_{max}(t) = \Phi(1,t)$ is the toroidal flux inside the magnetic separatrix. The inverse of the safety factor can be presented by finite expansions on a different set of basis functions (Moreau et al., 2013).

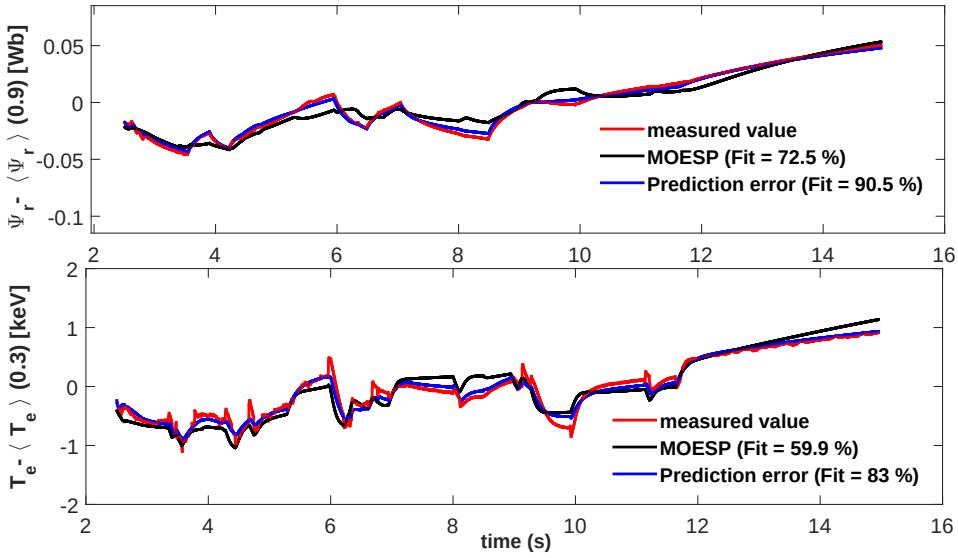


Figure 2.4: Comparison between the measured values of the simulated system and the outputs of the identified system for the MOESP and the output-error methods for simulation # 22.

The approximation of ι with the basis function $\alpha_k(x) = (1/x)(da_k/dx)$, where a_k are the cubic splines for Ψ_r presented in Fig. 2.1, is obtained as:

$$\iota(x,t) = -\frac{1}{2\Phi_{max}(t)} \sum_{k=1}^{n} \alpha_k(x) \Psi_{r\,k}(t) \tag{2.42}$$

If Φ_{max} is assumed to be constant, which is a good approximation when the toroidal field and the plasma shape are fixed, a matrix C_ι for the relation between $\tilde{\iota}(t)$ and $\tilde{\Psi}(t)$ can be found as:

$$\tilde{\iota}(t) = C_\iota \cdot \tilde{X} = \begin{bmatrix} C_{\iota,\Psi_r} & 0 \end{bmatrix} \begin{bmatrix} \tilde{\Psi}_{rk}(t) \\ \tilde{T}_{ek}(t) \end{bmatrix} \tag{2.43}$$

Once the model for the dynamics of Ψ_r and T_e is identified, the relation between ι and the states is approximated by (2.43) using the expression (2.42) to define the matrix C_{ι,Ψ_r}.

2.4.3 Estimation of the reference steady-state

Once the best fitting model is obtained and the optimal discrete representation of the system is transformed into a continuous-time linear time invariant (LTI) model $[A,\ B,\ C_\iota]$, the reference equilibrium values of the states can be estimated as in (Moreau et al., 2008).

Considering a constant input applied for a sufficiently long time, $U(t) = \overline{U}$, we obtain the steady state values $\overline{\Psi}_r$ $\overline{T}_e$. At steady state the plasma is in equilibrium and $\overline{X}$ can be calculated as:

$$\overline{X} = -A^{-1}[B(\overline{U} - \langle U \rangle) + \Delta_t X] + \langle X \rangle \tag{2.44}$$

The reference equilibrium point for the inverse of the safety factor is then:

$$\bar{\iota} = C_\iota \overline{X} \tag{2.45}$$

With this approximate estimation of the reference states, the reduced states $\tilde{X}$ around the reference point can be found. The error of the approximation can only introduce a constant offset both on the controlled variables and their target values. It should therefore have no effect on the control action, which depends only on their difference.

2.5 Identification results

sim. number	$V_{loop}(V)$	$P_{NBI1}(MW)$	$P_{NBI2}(MW)$	$P_{ECCD}(MW)$
1	0.02	1.5	2.5	5
2-6	-0.030 - 0.120	1.5	2.5	5
7-8	0.02	1.5	0 - 5	5
9-10	0.02	1.5	2.5	2.5 - 7.5
11-12	0.02	0 - 5	2.5	5
13	0.02	1.5	0 - 5	2.5 - 7.5
14	0.02	0 - 4	2.5	2.5 - 7.5
15-18	0.02	0 - 4	0 - 5	2.5 - 7
19-20	-0.23 - 0.27	0 - 4	0 - 5	2.5 - 7.5
21	-0.030 - 0.120	0 - 4	2.5	2.5 - 7.5
22	-0.030 - 0.120	1.5	0 - 5	2.5 - 7.5

Table 2.1: Table of the nonlinear METIS simulations used for the system identification showing the minimum and maximum values of the square-wave modulated inputs

For the identification of the model, 22 data sets from the METIS tokamak simulator were provided. The plasma parameters were those of a typical DIII-D steady state scenario that is described with more details in (Moreau et al., 2013). The toroidal field is 1.8 T, the central plasma density is $5 \cdot 10^{19}$ m^{-3} and the plasma current varies between 0.6 MA and 1.2 MA depending on the values of the heating and current drive actuators. The simulations were divided into several groups presented on Table 2.1. In each group, either a single input was modulated or different inputs were modulated in order to have a better estimation of the response of the system when the various inputs are simultaneously

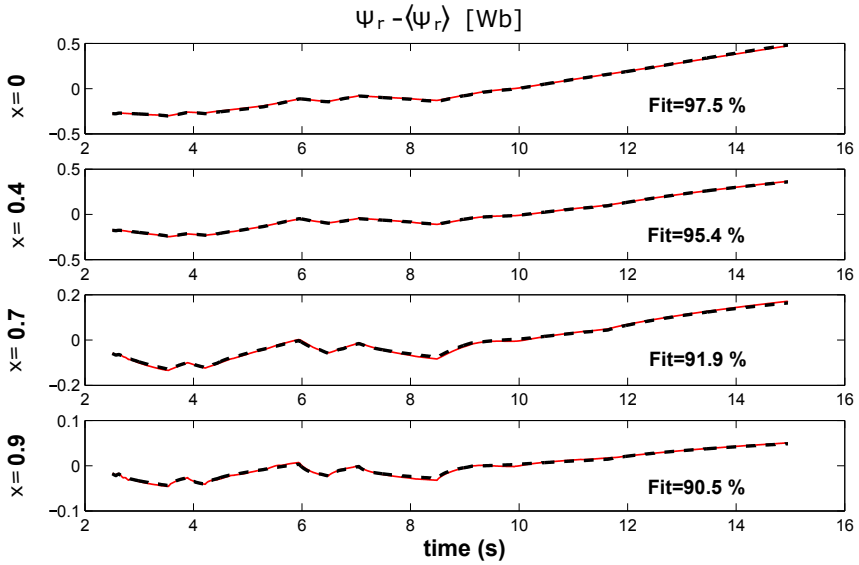


Figure 2.5: Plot of $\Psi_r(t)$ vs time for the simulation # 22. The black dashed traces represent the outputs of the simulation of the identified system and the red traces represent the outputs of the original METIS simulation. The fit parameter defined in (2.18) is indicated in each frame.

varying. The inputs were modulated using pseudorandom binary sequences in order to excite all the relevant frequencies which provide an accurate model that is valid in a large frequency range. In a real tokamak, such square wave excitation of the actuators, and in particular of V_{ext}, may not be possible due to the finite response time of the actuators to their control. However, the response model that is demanded here is to provide the response of the plasma to change in the actuator commands, rather than the response to the actual input powers and surface voltage.

Half of the data set is merged to identify the model and the other half is used for the validation stage. The simulation time for each data set is 15 s and only the data after 2.5 s were used, i.e when the system outputs reach values close to the reference values around which the linear model is sought. The measurements are taken with a sampling time of 0.005 s. The four actuators of the system, P_{NB1}, P_{NB2}, P_{ECCD} and V_{ext} have allowed ranges of variation between $0-5$ MW, $2.5-10$ MW, $0-4$ MW and -0.2 $-$ 0.5 V, respectively.

For the outputs of the system, 4 Galerkin coefficients were chosen from the poloidal magnetic flux profile Ψ and the safety factor ι, at radial grid $x = [0,\ 0.4,\ 0.7,\ 0.9]$ and 4 Galerkin coefficients were chosen for the electron temperature, T_e at radial grid $x = [0,\ 0.2,\ 0.3,\ 0.5]$. Thus the identified system is of order 8.

The characteristic time constants of the estimated system are: 7.69 s, 1.0 s, 0.75 s, 0.62 s, 0.13 s, 0.11 s, 0.07 s, 0.01 s. The estimated $\widehat{A}$ satisfies the eigenvalue constraints described

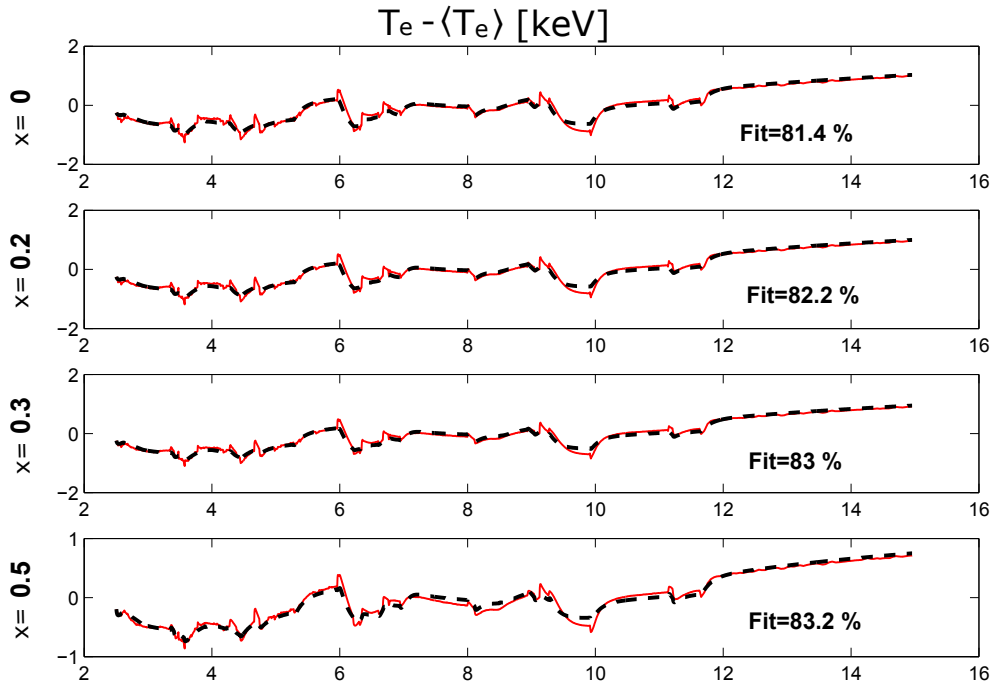


Figure 2.6: Plot of $T_e(t)$ vs time for the simulation # 22. The black dashed traces represent the outputs of the simulation of the identified system and the red traces represent the outputs of the original METIS simulation. The fit parameter defined in (2.18) is indicated in each frame.

in Sections 2.3. Simulations were included where only specific actuators were modulated while the others are fixed for a better estimation of the columns of B_P that are connected to these inputs. The value of $B_{\Psi,V}$, which is known from the physics of the problem, provides the response of the poloidal magnetic flux to the most powerful actuator in the system, V_{ext}.

Note that this system is a linearized model that represents the dynamics of the kinetic and magnetic profiles in a tokamak in a relatively broad vicinity of the linearization point, since the reference data set has a large variation of the actuators. Despite the highly nonlinear dynamics of the physical system, this model can be used only if the states of the system are in this broad vicinity, and therefore it is restricted to profile control applications in a particular tokamak and plasma scenario (toroidal magnetic field, plasma shape and average density) but with relatively large power variations (several megawatts). By taking the mean value of all the inputs used for the identification: $P_{NBI1} = 2.3\ MW$, $P_{NBI2} = 4.8\ MW$, $P_{ECCD} = 1.1\ MW$ and $V_{ext} = 0.028\ V$ as reference inputs, the reference states of the identified system can be calculated. Calculating the reference states for Ψ and T_e using (2.44), we get: $\overline{\Psi}_r = [2,\ 1.43,\ 0.61,\ 0.18]\ Wb$ and $\overline{T}_e = [5.56,\ 5.31,\ 5.03,\ 3.94]\ keV$.

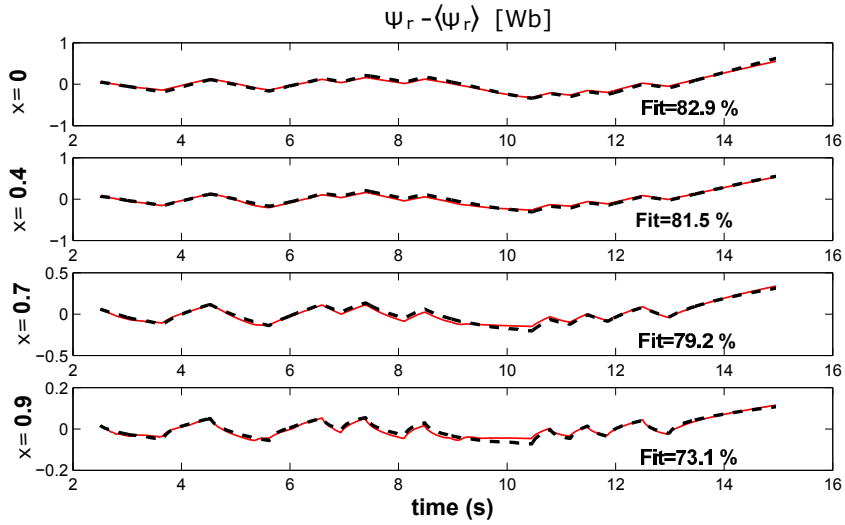


Figure 2.7: Plot of $\Psi_r(t)$ vs time for the simulation # 19. The black dashed traces represent the outputs of the simulation of the identified system and the red traces represent the outputs of the original METIS simulation. The fit parameter defined in (2.18) is indicated in each frame.

The results of the system identification can be evaluated by comparing the data predicted by the identified model with the original data. The inputs waveforms used in the simulation # 22 that is included in the identification data are presented in Fig. 2.9 and the identification results in Fig. 2.5 and Fig. 2.6. The results for simulation # 19, which is not used for identification but only for validation, are also presented. The input waveforms are presented in Fig. 2.10 and the evaluation results in Fig. 2.7 and Fig. 2.8. In both simulations, all the inputs were modulated and the plots of the reference data (METIS simulation) are compared with the output data predicted by the identified system. For each output of the system, the fit parameter values varied from about $70-98$ % for $\Psi_r(x,t)$ outputs and $60-88$ % for $T_e(x,t)$. The quality of the fit is varying within these ranges for all different simulation data except for simulations # 15 and # 20. The fit parameters for simulations # 15 and # 20 were also in the same range if the data is restricted to $t < 11$ s, but they become poor at the end of the simulation (11 $s <$ t ≤ 15 s), yielding fit parameters around $24-45$ % for $\Psi_r(x,t)$ and $55-58$ % for $T_e(x,t)$. The results for simulation # 20 are presented in Fig. 2.12 and Fig. 2.13 and the inputs in Fig. 2.11. This is explained by the fact that the total power dropped down to 2.5 MW between 11 s and 15 s, which results in a low temperature plasma where nonlinearities became more important. The identification results have shown that a linearized multivariable model of the coupled dynamics using a limited number of actuators can be obtained and that the model fits the original data satisfactorily when the power remains larger than 2.5 MW.

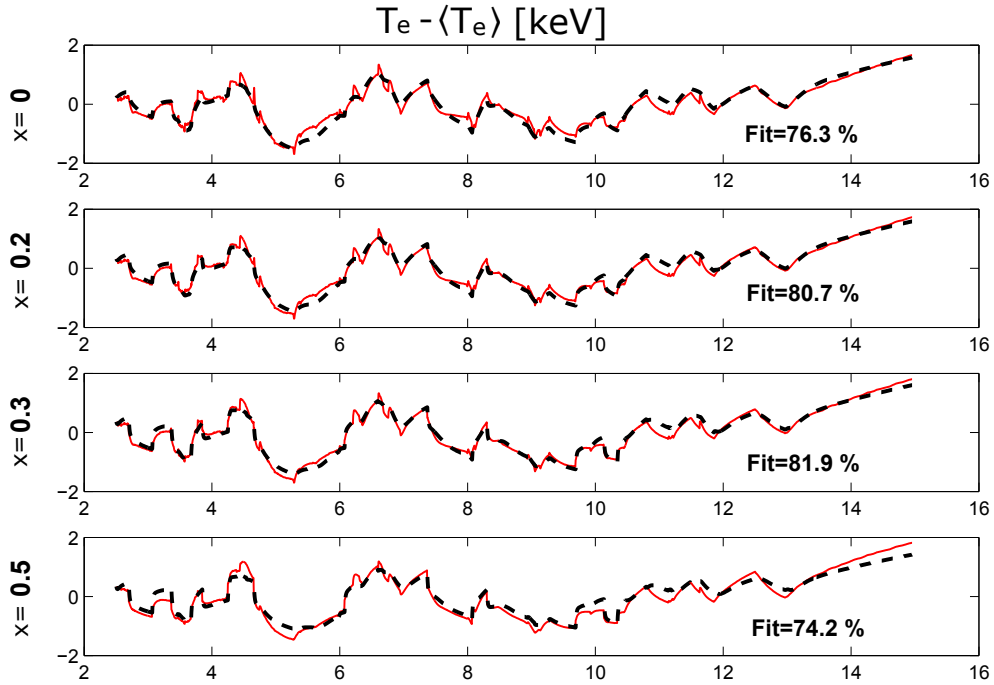


Figure 2.8: Plot of $T_e(t)$ vs time for the simulation # 19. The black dashed traces represent the outputs of the simulation of the identified system and the red traces represent the outputs of the original METIS simulation. The fit parameter defined in (2.18) is indicated in each frame.

2.6 Conclusion on the identification approach

This identified LTI model can be used for control of the coupled parameters in tokamaks. The identification scheme can be easily adapted to different tokamaks and in different conditions where the inputs are different than those used in this study.
The actuator variations used in METIS to obtain the identification/validation data are quite large (several megawatts, fractions of a volt) and typical of the variations that will be allowed during control experiments, with plasma current varying between 0.6 MA and 1.2 MA. As long as the toroidal field and plasma shape do not change, the identified model should then be appropriate for control applications. Otherwise, if a nonlinear model is not available, the only way to use the present approach is to perform series of linear model identifications around different plasma reference profiles. Previous approaches (Moreau et al., 2008; Moreau et al., 2011; Moreau et al., 2013) to the simultaneous control of magnetic and kinetic variables in a tokamak based on the same postulated linear system structure used singular perturbation methods (a two-time-scale approximation) to divide the system into a slow and a fast system that were identified separately. In contrast, the linear model obtained here contains the whole coupled dynamics of the electron temperature

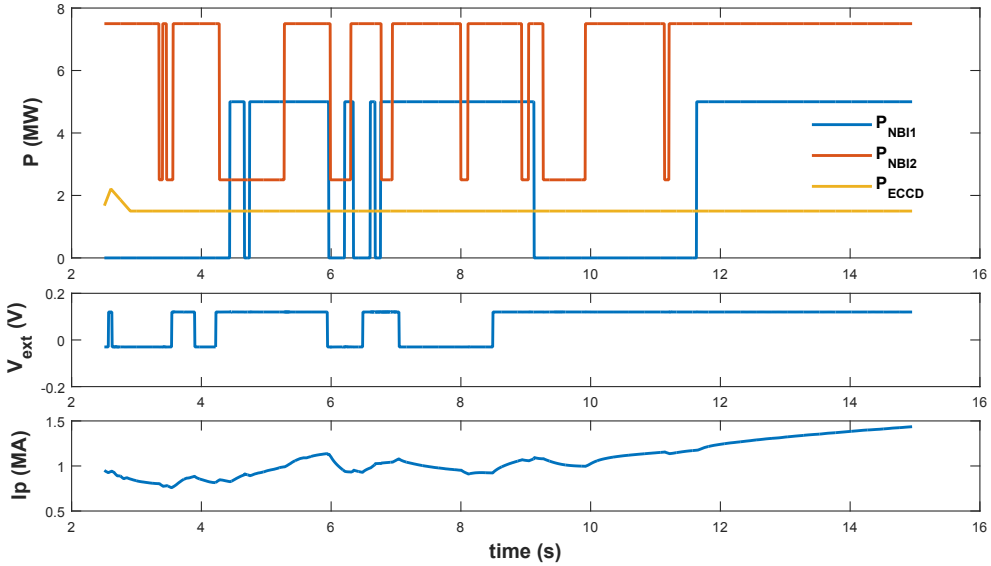


Figure 2.9: Plot of the four inputs (P and V_{ext}) and the total plasma current (I_p) vs time for simulation # 22.

and the poloidal magnetic flux, which may be more adequate for some tokamak machines, depending on the difference of the kinetic and magnetic time scales in a particular machine. The identification method presented here is faster than the one presented in the previous approaches (Moreau et al., 2008; Moreau et al., 2011). The execution time of the subspace identification takes about 10 seconds, while the recursive output-error methods execution time takes about 180 seconds. This combination of subspace and output-error methods could also be used within the two time scale estimation. It can provide a better estimate of the respective order of the slow and the fast models based on the information contained in the low frequency and high frequency data set, respectively.

2.7 Conclusion of the chapter

In this chapter the linearized models of coupled kinetic and magnetic parameters of the tokamak plasma were presented. Several techniques were presented to obtain linear models for control. While the linear model obtained by the system identification technique is presented only in finite-state representation, the linear model obtained by direct linearization of the physical model of the system is given by linear PDEs. In the next two chapters, these linear PDE models are used for developing control algorithms based on infinite dimensional settings.

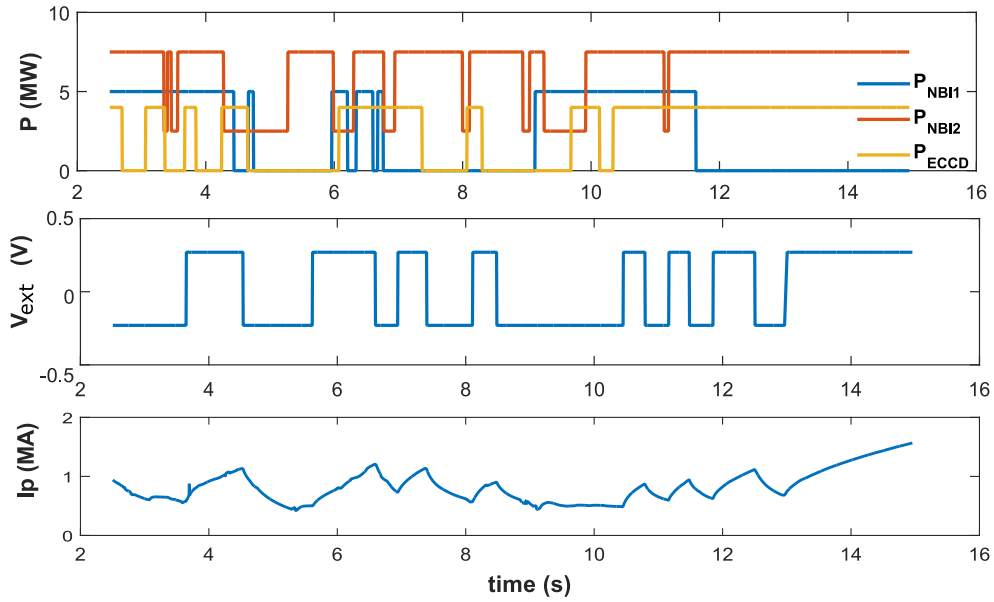


Figure 2.10: Plot of the four inputs (P and V_{ext}) and the total plasma current (I_p) vs time for simulation # 19.

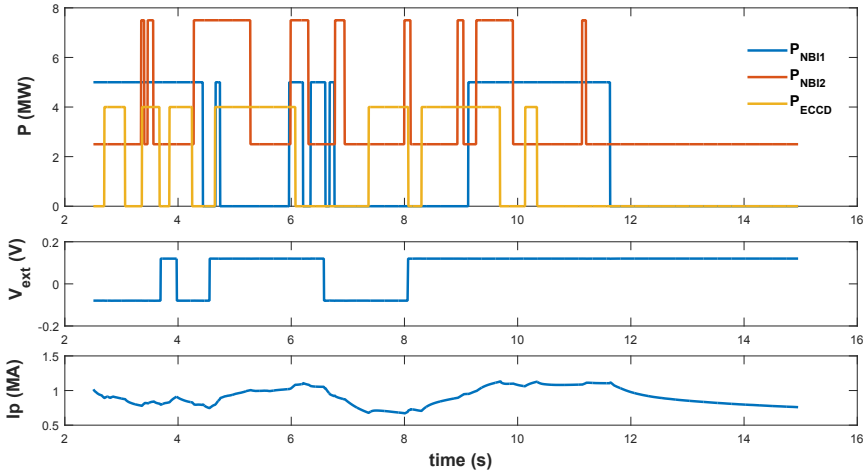


Figure 2.11: Plot of the inputs (P and V_{ext}) and the total plasma current (I_p) vs time for simulation # 20.

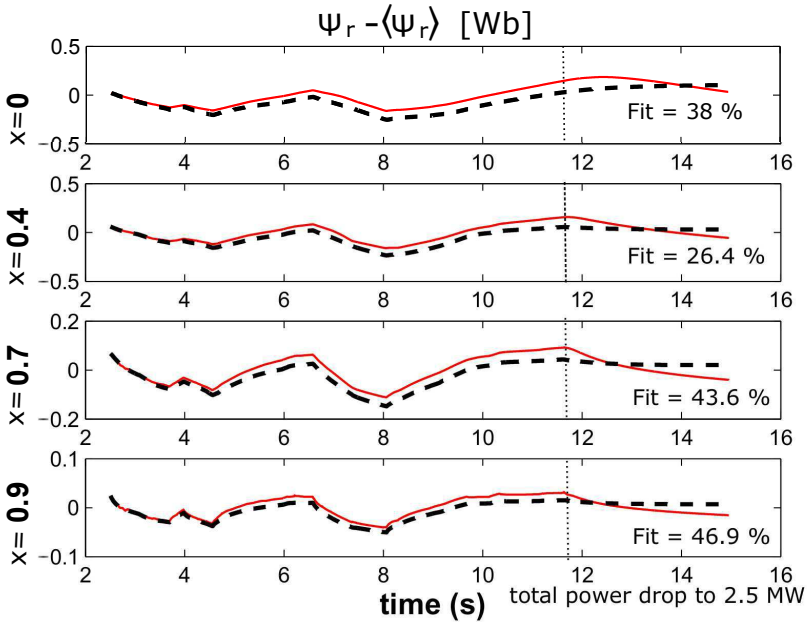


Figure 2.12: Plot of $T_e(t)$ vs time for the simulation # 20. The black dashed lines represent the outputs of the simulation of the identified system and the red traces represent the outputs of the original METIS simulation. The fit parameter defined in (2.18) is indicated in each frame. In this simulation at 11.6 s, the total power drops down to 2.5 MW.

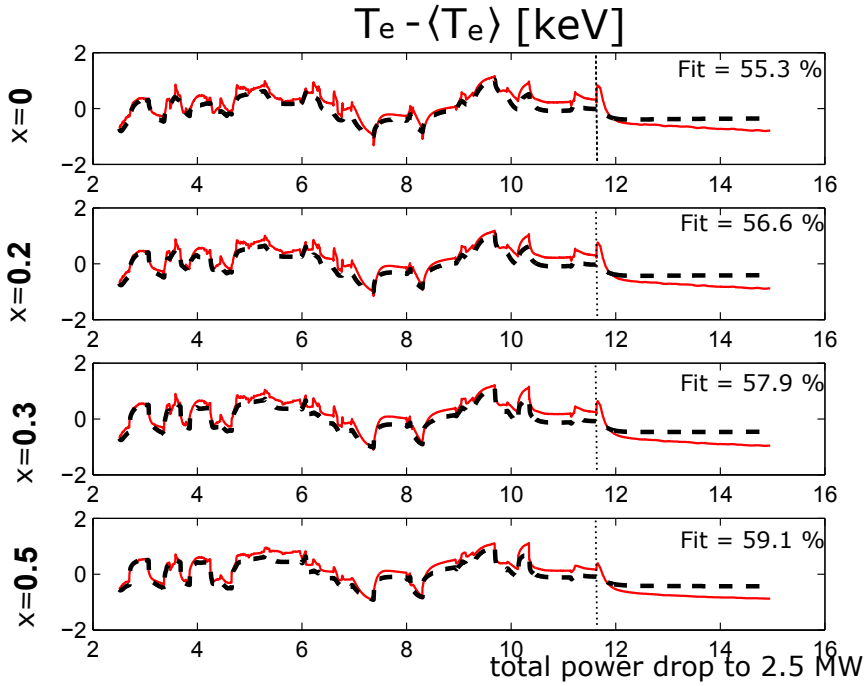


Figure 2.13: Plot of $T_e(t)$ vs time for the simulation # 20. The black dashed lines represent the outputs of the simulation of the identified system and the red traces represent the outputs of the original METIS simulation. The fit parameter defined in (2.18) is indicated in each frame. At 11.6 s the total power drops down to 2.5 MW.

Chapter 3

Distributed control of safety factor and electron temperature

Contents

3.1 Stability analysis and control of the coupled system 63

3.1.1 Calculation of the Lyapunov Function 67

3.1.2 Convergence rate control 67

3.2 System decoupling using singular perturbation theory 68

3.3 Composite control 70

3.3.1 Slow component 70

3.3.2 Control of the convergence rate of the slow component 71

3.3.3 Fast component 72

3.3.4 Control of the convergence rate of the boundary layer system 73

3.4 Control implementation 73

3.4.1 Auxiliary current and power density models 73

3.4.2 Calculation of the control 74

3.5 Results 77

3.5.1 TCV control 77

3.5.2 ITER control 80

3.6 Conclusion of the chapter 83

In this chapter, control algorithms for the simultaneous control of the tokamak safety factor and electron temperature are presented. The coupled system is given by a two coupled 1D linearized resistive diffusion equations in a circular domain. The control design is based on infinite dimensional setting using Control Lyapunov Functions (CLF). A CLF is a candidate Lyapunov function whose derivative can be made negative by the choice of control values (Kokotovic and Freeman, 1996). Control algorithms for tokamak plasmas

using an infinite dimensional approach are already used before. These works are dedicated on the control of the plasma safety factor using only the evolution of the magnetic flux dynamics equation. In (Bribiesca Argomedo et al., 2013a) a strict CLF for the diffusion equation of the poloidal magnetic flux gradient is computed. Here the diffusion coefficient is considered to be space and time varying and the input-to-state stability properties of the system are examined. To deal with the non-constant diffusion coefficient, the candidate Lyapunov function is proposed in a form of a weighted L_2 norm. A similar approach is used in (Gahlawat et al., 2012) by employing the sum-of-squares polynomials framework to maximize the bootstrap current. In (Gaye et al., 2013a) a proportional integral (PI) controller is developed for $\mathcal{H}\infty$ stabilization of spatial distribution of the current profile of tokamak plasmas.
In this chapter the strong coupling between the dynamics of the electron temperature and the magnetic flux equation is considered and simultaneous feedback control of this parameters is developed. There are several works dedicated to simultaneous control of the electron temperature and the safety factor (Kim and Lister, 2012; Barton et al., 2015c) using a finite dimensional approximation of the system.

In the coupled system there is a large difference between the time scales of the two plasma parameters. This difference varies with the size of the tokamak devices. Thus, in this chapter two control designs are proposed. In the first case a stability analysis of the full coupled system is performed and a control strategy is developed without dividing the slow and the fast components. In the second approach the two time scales are decoupled. For the control strategy a composite control is used. Composite control is designed using singular perturbation theory, where the fast component of the electron temperature is decoupled from the slow component that is governed by the evolution of the magnetic flux gradient z. Singular perturbation theory is widely used in control system theory. The singular perturbation model of a dynamical system is a model in which the derivatives of some of the states are multiplied by a small positive parameter ε. The basic concepts and definitions for finite dimensional singular perturbed systems can be found in (Kokotovic, Khalil, and O'reilly, 1999; Khalil and Grizzle, 1996; Gajic, 2001). There are several works dedicated to stability analysis and boundary control of singularly perturbed infinite dimensional systems. A boundary control of a class of linear hyperbolic systems of conservation laws based on the singular perturbation method is presented in (Tang, Prieur, and Girard, 2014). Stability analysis and backstepping control of singularly perturbed parabolic PDEs are presented in (Vazquez and Krstic, 2008).

The control strategy proposed in this chapter is tested on RAPTOR (RApid Plasma Transport simulatOR) (Felici and Sauter, 2012). RAPTOR is a control-oriented, physics-based code for simulating the 1D plasma coupled poloidal flux diffusion equation and the electron temperature transport. The transport equations used in this simulator are nonlinear and are tuned to match the data obtained from the real tokamak operation. The

code is used as a tool for real-time control applications design, fast plasma simulation and as a real-time simulator running in parallel with the plasma discharge in TCV tokamak. The distributed control is performed using Electron Cyclotron Resonance Heating (ECRH) actuation.

3.1 Stability analysis and control of the coupled system

The coupled system used in this chapter consists of two 1D linearized resistive diffusion equations given by (2.4). In the experimental settings, only the auxiliary heating sources are used as control inputs. In this case a perfect tracking of the total plasma current is considered. Thus, the boundary conditions used in this chapter are considered to be homogeneous:

$$\begin{aligned} \tilde{z}(0,t) &= 0, \forall t \geq 0 \\ \tilde{z}(1,t) &= 0, \forall t \geq 0 \\ \frac{\partial \tilde{T}_e}{\partial x}(0,t) &= 0, \forall t \geq 0 \\ \tilde{T}_e(1,t) &= \tilde{T}_{e,edge}, \forall t \geq 0 \end{aligned} \tag{3.1}$$

To prove the stability of the nominal system (2.4), with boundary conditions (3.1) and initial conditions (2.6), the following candidate Lyapunov function is chosen:

$$\mathcal{V}(\tilde{z}, \tilde{T}_e) = \frac{1}{2} \int_0^1 \begin{bmatrix} \tilde{z} & \tilde{T}_e \end{bmatrix} \begin{bmatrix} x^2 p_1(x) & 0 \\ 0 & \gamma x^2 p_2(x) \end{bmatrix} \begin{bmatrix} \tilde{z} \\ \tilde{T} \end{bmatrix} dx \tag{3.2}$$

where $p_1(x) > 0$, $p_2(x) > 0$ for $x \in [0,1]$ are polynomial functions to be selected.

Theorem 2
Suppose that for a given positive number α_1, there exist polynomials p_1 and p_2 such that $p_1(x) > 0$ and $p_2(x) > 0$ for all $x \in [0,1]$, and

$$A_1(x) + \alpha_1 A_2(x) \leq 0 \tag{3.3}$$

for all $x \in [0,1]$ where:

$$A_1(x) = \begin{bmatrix} A_{1,1}(x) & A_{1,2}(x) & A_{1,3}(x) & A_{1,4}(x) \\ A_{1,2}(x) & A_{2,2}(x) & A_{2,3}(x) & 0 \\ A_{1,3}(x) & A_{2,3}(x) & A_{3,3}(x) & A_{3,4}(x) \\ A_{1,4}(x) & 0 & A_{3,4}(x) & A_{4,4}(x) \end{bmatrix} \tag{3.4}$$

$$A_2(x) = \frac{1}{2}\begin{bmatrix} x^2 & 0 & 0 & 0 \\ 0 & \gamma x^2 & 0 & 0 \\ 0 & 0 & 0 & 0 \\ 0 & 0 & 0 & 0 \end{bmatrix} \tag{3.5}$$

$$\begin{aligned}
A_{1,1} =& \frac{1}{2}\Big(3xp_1'(x) + x^2p_1''(x) - p_1(x)\Big)a_1(x) + \frac{1}{2}a_1'(x)\Big(x^2p_1'(x) + 3xp_1(x)\Big) \\
& - 2xp_1(x)a_4(x) - x^2p_1'(x)a_4(x) \\
A_{1,2} =& - xp_1(x)a_2(x) - \frac{1}{2}x^2p_1'(x)a_2(x) + \frac{\gamma}{2\varepsilon}xb_3(x)\Big(xp_2'(x) + p_2(x)\Big) + \frac{\gamma}{2\varepsilon}xp_2(x)b_4(x) \\
A_{1,3} =& - \frac{1}{2}x^2p_1(x)a_4(x) \\
A_{1,4} =& - xp_1(x)a_3(x) - \frac{1}{2}x^2p_1'(x)a_3(x) \\
A_{2,2} =& - \frac{\gamma}{\varepsilon}x^2p_2(x)b_2(x) + \frac{\gamma}{2\varepsilon}b_1(x)\Big((x^2p_2''(x) + 2xp_2'(x) + p_2(x)\Big) \\
& + \frac{\gamma}{2\varepsilon}b_1'(x)\Big(x^2p_2'(x) + xp_2(x)\Big) \\
A_{2,3} =& - \frac{1}{2}x^2p_1(x)a_2(x) - \frac{\gamma}{2\varepsilon}x^2b_3(x)p_2(x) + \frac{\gamma}{2\varepsilon}x^2p_2(x)b_4(x) \\
A_{3,3} =& - x^2p_1(x)a_1(x) \\
A_{3,4} =& - \frac{1}{2}x^2p_1(x)a_4(x) \\
A_{4,4} =& - \frac{\gamma}{\varepsilon}x^2b_1(x)p_2(x)
\end{aligned}$$

Then the time derivative $\dot{\mathcal{V}}$ of $\mathcal{V}$ defined in (3.2) along the solutions of (2.4) and (2.5) satisfies:

$$\begin{aligned}
\dot{\mathcal{V}} \leq & - \beta_1\mathcal{V} + \int_0^1 x^2p_1(x)\frac{\partial}{\partial x}\Big(a_4(x)\tilde{j}_{aux}(\tilde{u},x,t)\Big)\tilde{z}dx \\
& + \gamma\int_0^1 \frac{x^2p_2(x)}{\varepsilon}b_5(x)\tilde{Q}_{aux}(\tilde{u},x,t)\tilde{T}_e dx, \forall t
\end{aligned} \tag{3.6}$$

where $\beta_1 = \dfrac{\alpha_1}{\max\limits_{x\in[0,1]}\Big(p_1(x),p_2(x)\Big)}$.

Proof. The time derivative of the Lyapunov function is:

$$\begin{aligned}
\dot{\mathcal{V}} &= \int_0^1 x^2p_1(x)\frac{\partial\tilde{z}}{\partial t}\tilde{z}dx + \gamma\int_0^1 x^2p_2(x)\frac{\partial\tilde{T}_e}{\partial t}\tilde{T}_e dx \\
&= \dot{\mathcal{V}}_{1,1} + \dot{\mathcal{V}}_{1,2} + \dot{\mathcal{V}}_{2,1} + \dot{\mathcal{V}}_{2,2} + \dot{\mathcal{V}}_{2,3} + \dot{\mathcal{V}}_{2,4}
\end{aligned} \tag{3.7}$$

where:

$$
\begin{aligned}
\dot{\mathcal{V}}_{1,1} &= \int_0^1 x^2 p_1(x) \frac{\partial}{\partial x}\left(\frac{a_1(x)}{x}\frac{\partial}{\partial x}\big(x\tilde{z}\big)\right)\tilde{z}dx \\
\dot{\mathcal{V}}_{1,2} &= \int_0^1 x^2 p_1(x) \frac{\partial}{\partial x}\big(a_2(x)\tilde{T}_e + a_3(x)\frac{\partial \tilde{T}_e}{\partial x} + a_4(x)\tilde{z}\big)\tilde{z}dx \\
\dot{\mathcal{V}}_{2,1} &= \frac{1}{\varepsilon}\int_0^1 x p_2(x)\frac{1}{x}\frac{\partial}{\partial x}\left(x b_1(x)\frac{\partial \tilde{T}_e}{\partial x}\right)\tilde{T}_e dx \\
\dot{\mathcal{V}}_{2,2} &= -\frac{1}{\varepsilon}\int_0^1 x^2 p_2(x) b_2(x)\tilde{T}_e^2 \\
\dot{\mathcal{V}}_{2,3} &= \frac{1}{\varepsilon}\int_0^1 x p_2(x)\frac{\partial}{\partial x}\big(x b_3(x)\tilde{z}\big)\tilde{T}_e \\
\dot{\mathcal{V}}_{2,4} &= \frac{1}{\varepsilon}\int_0^1 x p_2(x) b_4(x)\left(\frac{\partial}{\partial x}(x\tilde{z})\right)\tilde{T}_e dx \\
\dot{\mathcal{V}}_{2,5} &= \frac{1}{\varepsilon}\int_0^1 x^2 p_2(x) b_5(x)\tilde{Q}_{aux}(\tilde{u},x,t)\tilde{T}_e dx
\end{aligned}
\tag{3.8}
$$

Integrating $\dot{\mathcal{V}}_{1,1}$ by parts and considering the boundary conditions (2.5) we get:

$$
\begin{aligned}
\dot{\mathcal{V}}_{1,1} =& x p_1(x)\tilde{z}a_1(x)\frac{\partial}{\partial x}\big(x\tilde{z}\big)\Big|_0^1 - \int_0^1 x^2 p_1(x)a_1(x)\left(\frac{\partial \tilde{z}}{\partial x}\right)^2 dx \\
&- \int_0^1 \Big(2p_1(x) + x p_1'(x)\Big)a_1(x)\tilde{z}^2 dx - \int_0^1 \Big(x^2 p_1'(x) + 3x p_1(x)\Big)a_1(x)\tilde{z}\frac{\partial \tilde{z}}{\partial x}dx \\
=& -\frac{1}{2}a_1(x)\Big(x^2 p_1'(x) + 3x p_1(x)\Big)\tilde{z}^2\Big|_0^1 - \int_0^1 x^2 p_1(x)a_1(x)\left(\frac{\partial \tilde{z}}{\partial x}\right)^2 dx \\
&+ \frac{1}{2}\int_0^1 \Big(3x p_1'(x) + x^2 p_1''(x) - p_1(x)\Big)a_1(x)\tilde{z}^2 dx \\
&+ \frac{1}{2}\int_0^1 a_1'(x)\Big(x^2 p_1'(x) + 3x p_1(x)\Big)\tilde{z}^2 dx
\end{aligned}
\tag{3.9}
$$

Integrating $\dot{\mathcal{V}}_{1,2}$ and $\dot{\mathcal{V}}_{2,1}$ by parts and considering the boundary conditions (2.5) we get:

$$
\begin{aligned}
\dot{\mathcal{V}}_{1,2} =& -\int_0^1 \left(\big(2x p_1(x) + x^2 p_1'(x)\big)\tilde{z} + x^2 p_1(x)\frac{\partial \tilde{z}}{\partial x}\right)a_2(x)\tilde{T}_e dx \\
&- \int_0^1 \left(\big(2x p_1(x) + x^2 p_1'(x)\big)\tilde{z} + x^2 p_1(x)\frac{\partial \tilde{z}}{\partial x}\right)a_3(x)\frac{\partial \tilde{T}_e}{\partial x}dx \\
&- \int_0^1 \left(\big(2x p_1(x) + x^2 p_1'(x)\big)\tilde{z} + x^2 p_1(x)\frac{\partial \tilde{z}}{\partial x}\right)a_4(x)\tilde{z}dx
\end{aligned}
\tag{3.10}
$$

$$\begin{aligned}\dot{\mathcal{V}}_{2,1} =&\frac{1}{\varepsilon}x^2p_2(x)b_1(x)\tilde{T}_e\frac{\partial\tilde{T}_e}{\partial x}\bigg|_0^1-\frac{1}{\varepsilon}\int_0^1\bigg(xp_2(x)+x^2p_2'(x)\bigg)b_1(x)\tilde{T}_e\frac{\partial\tilde{T}_e}{\partial x}dx\\&-\frac{1}{\varepsilon}\int_0^1x^2p_2(x)b_1(x)\bigg(\frac{\partial\tilde{T}_e}{\partial x}\bigg)^2dx\\=&\frac{1}{2\varepsilon}\int_0^1b_1(x)\bigg((x^2p_2''(x)+2xp_2'(x)+p_2(x)\bigg)\tilde{T}_e^2dx\\&+\frac{1}{2\varepsilon}\int_0^1b_1'(x)\bigg(x^2p_2'(x)+xp_2(x)\bigg)\tilde{T}_e^2dx\\&-\frac{1}{\varepsilon}\int_0^1x^2p_2(x)b_1(x)\bigg(\frac{\partial\tilde{T}_e}{\partial x}\bigg)^2dx-\frac{1}{\varepsilon}\bigg(p_2(x)+xp_2'(x)\bigg)b_1(x)\tilde{T}_e^2\bigg|_0^1\end{aligned}\tag{3.11}$$

Here $\tilde{T}_{e,edge}$ is assumed to be very small compared to the temperature in the center of the plasma and we can consider it to be zero in the analysis.
Integrating $\dot{\mathcal{V}}_{2,3}$ and $\dot{\mathcal{V}}_{2,4}$ by parts and considering the boundary conditions (2.5) we get:

$$\dot{\mathcal{V}}_{2,3}=-\frac{1}{\varepsilon}\int_0^1xb_3(x)\bigg(xp_2'(x)+p_2(x)\bigg)\tilde{z}\tilde{T}_edx-\frac{1}{\varepsilon}\int_0^1x^2b_3(x)p_2(x)\frac{\partial\tilde{z}}{\partial x}\tilde{T}_edx\tag{3.12}$$

$$\dot{\mathcal{V}}_{2,4}=\frac{1}{\varepsilon}\int_0^1xp_2(x)b_4(x)\tilde{z}\tilde{T}_edx+\frac{1}{\varepsilon}\int_0^1x^2p_2(x)b_4(x)\frac{\partial\tilde{z}}{\partial x}\tilde{T}_edx\tag{3.13}$$

The derivative of the Lyapunov function combining (3.7)-(3.13) can be written as:

$$\begin{aligned}\dot{\mathcal{V}}=&\int_0^1\begin{bmatrix}\tilde{z}\\\tilde{T}_e\\\frac{\partial\tilde{z}}{\partial x}\\\frac{\partial\tilde{T}_e}{\partial x}\end{bmatrix}^TA_1(x)\begin{bmatrix}\tilde{z}\\\tilde{T}_e\\\frac{\partial\tilde{z}}{\partial x}\\\frac{\partial\tilde{T}_e}{\partial x}\end{bmatrix}dx+\int_0^1x^2p_1(x)\frac{\partial}{\partial x}\bigg(a_4(x)\tilde{j}_{aux}(\tilde{u},x,t)\bigg)\tilde{z}dx\\&+\gamma\int_0^1\frac{x^2p_2(x)}{\varepsilon}b_5(x)\tilde{Q}_{aux}(\tilde{u},x,t)\tilde{T}_edx\end{aligned}\tag{3.14}$$

where the matrix $A_1(x)$ is given in (3.4).
Combining the inequality (3.3) and (3.14) provides (3.6). □

Corollary 1
Under the conditions of Theorem 2, the system (2.4) with $\tilde{u}=0$, boundary condition (2.5) and initial conditions (2.6) is globally exponentially stable. The convergence rate of the system satisfies $\mathcal{V}\leq e^{-\beta_1t}\mathcal{V}(\tilde{z}_0,\tilde{T}_{e,0})$ where $\beta_1=\alpha_1/[\max_{x\in[0,1]}\big(p_1(x),p_2(x)\big)]$.

Proof. By setting $\tilde{u} = 0$, the auxiliary current and power density are zero ($\tilde{j}_{aux} = 0, \tilde{Q}_{aux} = 0$) and from Theorem 2, the following inequality is obtained:

$$\dot{\mathcal{V}} \leq -\beta_1 \mathcal{V}, \forall t \geq t_0 \tag{3.15}$$

integrating this inequality over time gives the result. □

3.1.1 Calculation of the Lyapunov Function

To compute the polynomial functions p_1 and p_2 that are presented in Theorem 2, let us consider them as Legendre polynomials. See Appendix A for their definition. Using Legendre polynomials, the inequality (3.3) is formulated and solved as an LMI problem that is defined with x in the range $[0, 1]$. Legendre polynomials are orthogonal in the range $[-1, 1]$, and the polynomials p_1 and p_2 may be expanded in this interval in terms of them as (Kaplan, 2002):

$$p_1(x) = \sum_{i=0}^{N_1} c_{1,i} P_i(x)$$

$$p_2(x) = \sum_{i=0}^{N_2} c_{2,i} P_i(x)$$

where $c_{1,1}, ..., c_{1,N_1}$ and $c_{2,1}, ..., c_{2,N_1}$ are constant, $P_i(x)$ is $i-th$ order Legendre polynomial and N_1 and N_2 are the orders of the Legendre polynomials for p_1 and p_2, respectively.
Sampling the interval $[0, 1]$ and representing p_1 and p_2 as a sum of Legendre polynomials permits us to formulate the following LMI problem:
Maximize $\alpha_1 \geq 0$
such that the polynomials p_1 and p_2 satisfy:

1. $0 < p_1(x) \leq p_{1,max}$ and $0 < p_2(x) \leq p_{2,max}, \forall x \in [0, 1]$
2. $A_1(x) + \alpha_1 A_2(x) \leq 0, \forall x \in [0, 1]$

This LMI problem for finding the unknown constant parameters $c_{1,1}, ..., c_{1,N_1}$ and $c_{2,1}, ..., c_{2,N_1}$ is solved using YALMIP toolbox (Löfberg, 2004) for MATLAB ®.

3.1.2 Convergence rate control

Considering the previous results, a control strategy is presented. This theory can be implemented in small scale tokamaks in which there is no significant time scales difference

between the fast and the slow components. This control strategy is not appropriate to be applied in large scale tokamaks. Using only one candidate Lyapunov function is not effective enough to control the convergence rate of a system that consists of several components with different time scales. The control strategy for large tokamaks is discussed in the next section.

Corollary 2
If the conditions of Theorem 2 are verified, the feedback control parameters $\tilde{u}_{ctr}$ can be calculated to obtain the following relation:

$$\begin{aligned}&\int_0^1 x^2 p_1(x)\frac{\partial}{\partial x}\left(a_4(x)\tilde{\tilde{j}}_{aux}(\tilde{u}_{ctrl},x,t)\right)\tilde{z}dx\\&+\gamma\int_0^1 \frac{x^2 p_2(x)}{\varepsilon}b_5(x)\tilde{Q}_{aux}(\tilde{u}_{ctrl},x,t)\tilde{T}_e dx=-\alpha_2\mathcal{V}\end{aligned}\tag{3.16}$$

where $\alpha_2 > 0$ is a tuning parameter. Using this feedback control, the system (2.4) with boundary conditions (2.5) is globally exponentially stable with convergence rate that satisfies $\dot{\mathcal{V}} \leq -\beta_2\mathcal{V}$, where $\beta_2 = (\alpha_1+\alpha_2)/[\max_{x\in[0,1]}\big(p_1(x),p_2(x)\big)]$. The convergence rate is thus increased by a factor $\alpha_2/[\max_{x\in[0,1]}\big(p_1(x),p_2(x)\big)]$.

3.2 System decoupling using singular perturbation theory

In the tokamak machines, in particular in the large scale machines, the dynamics of the evolution of z is much slower than the dynamics of T_e (Moreau et al., 2008). To deal with the two time scales we introduce the small (constant) parameter ε that represents the typical ratio between the energy confinement time and the characteristic resistive diffusion time. To apply the singular perturbation theory, the system is divided in two different time scales introducing the fast time scale $\tau = \varepsilon t$. Using this time scale we can divide the system by slow and fast components. The slow components are considered fixed in the fast time scale and using static equations they are separated from the fast component. Considering that $\varepsilon \ll 1$, the static equation for the electron temperature is computed assuming that the left side of T_e equation is equal to zero. In this equation T_e is replaced by T_s, which denotes the slow variation of the temperature and is called quasi-steady state (QSS), determined by:

$$\begin{aligned} 0 =& \frac{1}{x}\frac{\partial}{\partial x}\left(xb_1(x)\frac{\partial \tilde{T}_s}{\partial x}\right) - b_2(x)\tilde{T}_s + \frac{1}{x}\frac{\partial}{\partial x}\left(xb_3(x)\tilde{z}\right) \\ &+ \frac{b_4(x)}{x}\left(\frac{\partial}{\partial x}(x\tilde{z})\right) + b_5(x)\tilde{Q}_{aux,s}(\tilde{u}_s, x, t) \end{aligned} \tag{3.17}$$

with boundary conditions:

$$\begin{aligned} \frac{\partial \tilde{T}_s}{\partial x}(0,t) &= 0 \\ \tilde{T}_s(1,t) &= \tilde{T}_{e,edge} \end{aligned} \tag{3.18}$$

The solution of $\tilde{T}_s(\tilde{z}, \tilde{P}_{aux,s}, x, t)$ is calculated at each time instant. Because of the complexity of this equation, the solution is calculated using numerical methods in the control applications. The temperature can be presented as the sum of the slow and the fast component: $T_e = T_s + T_f$. The evolution of the fast dynamics is presented by the boundary layer model in fast-time scale:

$$\frac{\partial \tilde{T}_f}{\partial \tau} = \frac{1}{x}\frac{\partial}{\partial x}\left(xb_1(x)\frac{\partial \tilde{T}_f}{\partial x}\right) - b_2(x)\tilde{T}_f + b_5(x)\tilde{Q}_{aux,f}(\tilde{u}_f, x, \tau) \tag{3.19}$$

with boundary conditions:

$$\begin{aligned} \frac{\partial \tilde{T}_f}{\partial x}(0,\tau) &= 0 \\ \tilde{T}_f(1,\tau) &= 0 \end{aligned} \tag{3.20}$$

Finally, the decoupled system is presented as:

$$\begin{cases} \dfrac{\partial \tilde{z}}{\partial t} = \dfrac{\partial}{\partial x}\left(\dfrac{a_1(x)}{x}\dfrac{\partial}{\partial x}\left(x\tilde{z}\right)\right) + \dfrac{\partial}{\partial x}\left(a_2(x)\tilde{T}_s\right) \\ \qquad\qquad + \dfrac{\partial}{\partial x}\left(a_3(x)\dfrac{\partial \tilde{T}_s}{\partial x}\right) + \dfrac{\partial}{\partial x}\left(a_4(x)\tilde{z}\right) + \dfrac{\partial}{\partial x}\left(a_5(x)\tilde{j}_{aux}(\tilde{u}_s, x)\right) \\ \dfrac{\partial \tilde{T}_f}{\partial \tau} = \dfrac{1}{x}\dfrac{\partial}{\partial x}\left(xb_1(x)\dfrac{\partial \tilde{T}_f}{\partial x}\right) - b_2(x)\tilde{T}_f + b_5(x)\tilde{Q}_{aux,f}(\tilde{u}_f, x, \tau) \end{cases} \tag{3.21}$$

with boundary conditions:

$$\begin{aligned} \tilde{z}(0,t) &= 0 \\ \tilde{z}(1,t) &= 0 \\ \frac{\partial \tilde{T}_f}{\partial x}(0,\tau) &= 0 \\ \tilde{T}_f(1,\tau) &= 0 \end{aligned} \tag{3.22}$$

3.3 Composite control

3.3.1 Slow component

The composite control is obtained by separately calculating and combining the slow (u_s) component and the fast (u_f) component. First, the slow component of the control is calculated by considering only the evolution of the slow component of the system:

$$\begin{cases} \dfrac{\partial \tilde{z}}{\partial t} = \dfrac{\partial}{\partial x}\left(\dfrac{a_1(x)}{x}\dfrac{\partial}{\partial x}(x\tilde{z})\right) + \dfrac{\partial}{\partial x}\left(a_2(x)\tilde{T}_s + a_3(x)\dfrac{\partial \tilde{T}_s}{\partial x} + a_4(x)\tilde{z}\right) \\ \qquad\quad + \dfrac{\partial}{\partial x}\left(a_5(x)\tilde{j}_{aux}(\tilde{u}_s, x, t)\right) \end{cases} \tag{3.23}$$

with boundary conditions:

$$\begin{aligned} \tilde{z}(0,t) &= 0 \\ \tilde{z}(1,t) &= 0 \end{aligned} \tag{3.24}$$

To compute the stability of the slow component of the system, the following Lyapunov function candidate is chosen:

$$\mathcal{V}_s(\tilde{z}) = \frac{1}{2}\int_0^1 x^2 p_s(x)\tilde{z}^2 dx \tag{3.25}$$

Theorem 3
Suppose that for a given positive number α_3 there exists a polynomial $p_s(x)$ such that $p_s(x) > 0$ for all $x \in [0,1]$ and satisfying for all $x \in [0,1]$:

$$\begin{aligned} &\frac{1}{2}a_1(x)\left(3xp_s'(x) + x^2 p_s''(x) - p_s(x)\right) + \frac{1}{2}a_1'(x)\left(x^2 p_s'(x) + 3xp_s(x)\right) \\ &+ a_4(x)\left(xp_s(x) + \frac{1}{2}x^2 p_1'(x)\right) + \frac{1}{2}x^2 a_4'(x)p_s(x) + \alpha_3\frac{1}{2}x^2 \leq 0 \end{aligned} \tag{3.26}$$

then the time derivative $\dot{\mathcal{V}}_s$ of the function $\mathcal{V}_s$ defined by (3.25) verifies:

$$\begin{aligned} \dot{\mathcal{V}}_s \leq &-\beta_3 \mathcal{V}_s + \int_0^1 x^2 p_s(x)\frac{\partial}{\partial x}\left(a_2(x)\tilde{T}_s + a_3(x)\frac{\partial \tilde{T}_s}{\partial x}\right)\tilde{z}dx \\ &+ \int_0^1 x^2 p_s(x)\frac{\partial}{\partial x}\left(a_5(x)\tilde{j}_{aux}(\tilde{u}_s, x, t)\right)\tilde{z}dx \end{aligned} \tag{3.27}$$

where $\beta_3 = \frac{\alpha_3}{\max\limits_{x\in[0,1]} p_s(x)}$

Proof. The time derivative of the Lyapunov function is:

$$\begin{aligned}\dot{\mathcal{V}}_s =&\frac{1}{2}\int_0^1 x^2 p_s(x)\frac{\partial \tilde{z}}{\partial t}\tilde{z}dx\\ =&\int_0^1 x^2 p_s(x)\frac{\partial}{\partial x}\left(a_1(x)\frac{\partial}{\partial x}(x\tilde{z})\right)\tilde{z}dx+\int_0^1 x^2 p_s(x)\frac{\partial}{\partial x}\left(a_4(x)\tilde{z}\right)dx\\ &+\int_0^1 x^2 p_s(x)\frac{\partial}{\partial x}\left(a_2(x)\tilde{T}_s+a_3(x)\frac{\partial \tilde{T}_s}{\partial x}\right)\tilde{z}dx\\ &+\int_0^1 x^2 p_s(x)\frac{\partial}{\partial x}\left(a_5(x)\tilde{j}_{aux}(u,x,t)\right)\tilde{z}dx\end{aligned} \tag{3.28}$$

Integrating by parts, considering the boundary conditions (3.24) we obtain the following inequality:

$$\begin{aligned}\dot{\mathcal{V}}_s =&\frac{1}{2}\int_0^1 \left(3xp_s'(x)+x^2p_s''(x)-p_s(x)\right)a_1(x)\tilde{z}^2dx+\frac{1}{2}\int_0^1 a_1'(x)\left(x^2p_s'(x)+3xp_s(x)\right)\tilde{z}^2dx\\ &+\int_0^1 a_4(x)\left(xp_s(x)+\frac{1}{2}x^2p_1'(x)\right)\tilde{z}^2dx-\int_0^1\frac{1}{2}x^2a_4'(x)p_1(x)\tilde{z}^2dx\\ &-\int_0^1 x^2p_s(x)a_1(x)\left(\frac{\partial\tilde{z}}{\partial x}\right)^2dx+\int_0^1 x^2p_s(x)\frac{\partial}{\partial x}\left(a_2(x)\tilde{T}_s+a_3(x)\frac{\partial\tilde{T}_s}{\partial x}\right)\tilde{z}dx\\ &+\int_0^1 x^2p_s(x)\frac{\partial}{\partial x}\left(a_5(x)\tilde{j}_{aux}(u,x,t)\right)\tilde{z}\\ \leq&\frac{1}{2}\int_0^1 \left(3xp_s'(x)+x^2p_s''(x)-p_s(x)\right)a_1(x)\tilde{z}^2dx+\frac{1}{2}\int_0^1 a_1'(x)\left(x^2p_s'(x)+3xp_s(x)\right)\tilde{z}^2dx\\ &+\int_0^1 a_4(x)\left(xp_s(x)+\frac{1}{2}x^2p_1'(x)\right)\tilde{z}^2dx-\int_0^1\frac{1}{2}x^2a_4'(x)p_1(x)\tilde{z}^2dx\\ &+\int_0^1 x^2p_s(x)\frac{\partial}{\partial x}\left(a_2(x)\tilde{T}_s+a_3(x)\frac{\partial\tilde{T}_s}{\partial x}\right)\tilde{z}dx\\ &+\int_0^1 x^2p_s(x)\frac{\partial}{\partial x}\left(a_5(x)\tilde{j}_{aux}(u,x,t)\right)\tilde{z}\end{aligned} \tag{3.29}$$

Combining the inequalities (3.26) and (3.29) proves the theorem. □

3.3.2 Control of the convergence rate of the slow component

Corollary 3

If the conditions of Theorem 3 are verified, the feedback control parameters of the slow component, $\tilde{u}_{s,ctr}$ can be calculated to obtain the following relation:

$$\int_0^1 x^2 p_s(x)\frac{\partial}{\partial x}\left(a_2(x)\tilde{T}_s + a_3(x)\frac{\partial \tilde{T}_s}{\partial x}\right)\tilde{z}dx + \int_0^1 x^2 p_s(x)\frac{\partial}{\partial x}\left(a_5(x)\tilde{j}_{aux}(\tilde{u}_{s,ctr},x,t)\right)\tilde{z} = -\alpha_4 \mathcal{V}_s \tag{3.30}$$

where $\alpha_4 > 0$ is a tuning parameter. Using this feedback control, the system (3.23) with boundary conditions (3.24) is globally exponentially stable with a convergence rate that satisfies $\dot{\mathcal{V}}_s \leq -\beta_4 \mathcal{V}_s$, where $\beta_4 = \frac{\alpha_3+\alpha_4}{\max\limits_{x\in[0,1]} p_s(x)}$.

3.3.3 Fast component

The fast component of the system is presented by the following PDE:

$$\frac{\partial \tilde{T}_f}{\partial \tau} = \frac{1}{x}\frac{\partial}{\partial x}\left(x b_1(x)\frac{\partial \tilde{T}_f}{\partial x}\right) - b_2(x)\tilde{T}_f + b_5(x)\tilde{Q}_{aux,f}(\tilde{u}_f,x,t) \tag{3.31}$$

with boundary conditions:

$$\begin{aligned}\frac{\partial \tilde{T}_f}{\partial x}(0,\tau) &= 0\\ \tilde{T}_f(1,\tau) &= 0\end{aligned} \tag{3.32}$$

To compute the stability of the fast component (boundary layer system) the following Lyapunov function candidate is selected:

$$\mathcal{V}_f(\tilde{T}_f) = \frac{1}{2}\int_0^1 x^2 p_f(x)\tilde{T}_f^2 dx \tag{3.33}$$

Theorem 4
Suppose that for a given positive number α_5 there exists a polynomial $p_f(x)$ such that $p_f(x) > 0$ for all $x \in [0,1]$ and satisfying for all $x \in [0,1]$:

$$\begin{aligned}&\frac{1}{2}b_1(x)\left(x^2 p_f''(x) + 2x p_f'(x) + p_f(x)\right)\\ &+ \frac{1}{2}b_1'(x)\left(x^2 p_f'(x) + x p_f(x)\right) - x^2 b_2(x) p_f(x) + \alpha_5 \frac{1}{2}x^2 \leq 0\end{aligned} \tag{3.34}$$

then the time derivative $\dot{\mathcal{V}}_f$ of the function $\mathcal{V}_f$ defined by (3.33) verifies

$$\dot{\mathcal{V}}_f \leq -\beta_5 \mathcal{V}_f + \int_0^1 x^2 p_f(x) b_5(x)\tilde{Q}_{aux,f}(\tilde{u}_f,x,\tau)\tilde{T}_f dx \tag{3.35}$$

where $\beta_5 = \frac{\alpha_5}{\max\limits_{x\in[0,1]} p_f(x)}$.

Proof.

$$\begin{aligned}\dot{\mathcal{V}}_f = &\int_0^1 x^2 p_f(x)\frac{1}{x}\frac{\partial}{\partial x}\left(xb_1(x)\frac{\partial \tilde{T}_f}{\partial x}\right)\tilde{T}_f dx \\ &- \int_0^1 x^2 p_f(x) b_2(x)\tilde{T}_f^2 dx + \int_0^1 x^2 p_f(x) b_5(x)\tilde{Q}_{aux,f}(\tilde{u}_f, x, t)\tilde{T}_f dx\end{aligned} \tag{3.36}$$

Integrating by parts and considering the boundary conditions of the boundary layer system (3.32), we have:

$$\begin{aligned}\dot{\mathcal{V}}_f =&\frac{1}{2}\int_0^1 b_1(x)\left(x^2 p_f''(x) + 2xp_f'(x) + p_f(x)\right)\tilde{T}_f^2 dx \\ &+ \frac{1}{2}\int_0^1 b_1'(x)\left(x^2 p_f'(x) + xp_f(x)\right)\tilde{T}_f^2 dx - \int_0^1 x^2 p_f(x) b_1(x)\left(\frac{\partial \tilde{T}_f}{\partial x}\right)^2 dx \\ &- \int_0^1 x^2 p_f(x) b_2(x)\tilde{T}_f^2 dx + \int_0^1 x^2 p_f(x) b_5(x)\tilde{Q}_{aux,f}(\tilde{u}_f, x, t)\tilde{T}_f dx\end{aligned} \tag{3.37}$$

Combining the inequalities (3.34) and (3.37) provides (3.35). □

3.3.4 Control of the convergence rate of the boundary layer system

Corollary 4
If the conditions of Theorem 4 are verified. The feedback control parameters of the boundary layer system, $\tilde{u}_{f,ctr}$ can be calculated to obtain the following relation:

$$\int_0^1 x^2 p_f(x) b_5(x)\tilde{Q}_{aux,f}(\tilde{u}_{f,ctr}, x, \tau)\tilde{T}_f dx = -\alpha_6 \mathcal{V}_f \tag{3.38}$$

where $\alpha_6 > 0$ is a tuning parameter. Using this feedback control, the system (3.31) with boundary conditions (3.32) is globally exponentially stable with convergence rate that satisfies $\dot{\mathcal{V}} \leq -\beta_6 \mathcal{V}$, where $\beta_6 = \frac{\alpha_5+\alpha_6}{\max\limits_{x\in[0,1]} p_f(x)}$.

3.4 Control implementation

3.4.1 Auxiliary current and power density models

In this application, for the model of the auxiliary sources, the analytical parametrization is considered as in Section 1.5. The total auxiliary current density is computed as the sum

of the current densities induced by each ECCD antenna:

$$\tilde{j}_{aux} = \sum_{i=1}^{n_{aux}} \frac{\overline{T}_e}{n_e} j_{dis,i}(x)\tilde{P}_{aux,i}(t) \tag{3.39}$$

where n_{aux} denotes the number of the ECCD sources. Weighted Gaussian distributions $j_{dis,i}(x)$ representing the normalized reference current density deposition profiles are considered as in (Felici et al., 2011):

$$j_{dis,i} = c_{cd} e^{x^2/a0.5^2} e^{-4(x-x_{dept,i})^2/a\omega_{cd,i}^2} \tag{3.40}$$

where ω_{dep} is the deposition width and x_{dep} is the the location of the peak of the deposition and c_{dc} is a parameter that describes the efficiency of current drive values. In this work we are using the model presented in (Felici et al., 2011) that is implemented in the simulator.

The total auxiliary power density is presented as the sum of the power densities produced by each ECCD antenna as given in Section 1.5:

$$\tilde{Q}_{aux} = \sum_{i=1}^{n_{aux}} Q_{dis,i}(x)\tilde{P}_{aux,i}(t) \tag{3.41}$$

The individual auxiliary power densities are modeled as in (Felici et al., 2011):

$$Q_{dis,i} = exp\{\frac{-4(x-x_{dep,i})^2}{a^2\omega_{dep,i}^2}\} / \int_0^1 exp\{\frac{-4(x-x_{dep,i})^2}{a^2\omega_{dep,i}^2}\} V' dx \tag{3.42}$$

3.4.2 Calculation of the control

The control is implemented using limited number of actuators with limited degrees of freedom. As it was presented previously in this chapter, only the powers of the ECCD clusters (P_{aux}) are used as control inputs. In the controller implementation, the optimal values of these parameters have to be calculated. In the case of the practical implementation of the controller presented in Section 3.1.2, the following optimization problem is formulated to find the optimal engineering parameters at each time instant (Bribiesca Argomedo et al., 2013a):

$$\begin{aligned} &arg\,\min_{\tilde{u}} \;\; f(\tilde{u}) \\ &\text{subject to}: -\alpha_2 \mathcal{V} \leq f(\tilde{u}) \leq 0 \\ &\tilde{u}_{min} \leq \tilde{u} \leq \tilde{u}_{max} \end{aligned} \tag{3.43}$$

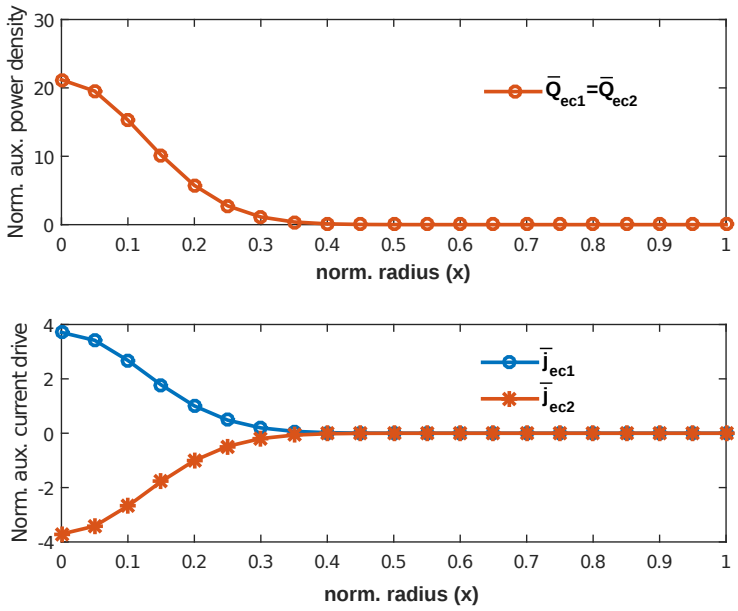


Figure 3.1: Normalized auxiliary electron cyclotron current-drive j_{dis} $(10^{20}\frac{m^{-5}A}{keVW})$ and Normalized auxiliary electron cyclotron power density Q_{dis} (m^{-3}) for the TCV configuration.

where

$$f(\tilde{u}) = \int_0^1 x^2 p_1(x) \frac{\partial}{\partial x}\big(a_4(x)\tilde{j}_{aux}(\tilde{u},x)\big)\tilde{z}dx + \int_0^1 x^2 \frac{\gamma p_2(x)}{\varepsilon} b_5(x)\tilde{Q}_{aux}(\tilde{u},x)\tilde{T}_e dx$$

Here $\tilde{u}_{min}$ and $\tilde{u}_{max}$ stand for the minimum and the maximum values of the allowed $\tilde{P}_{aux}$ for each antenna.

Remark

The convergence rate of the system is this section is calculated from a practical implementation standpoint. It takes into account the limitations of the current and of the power distribution profiles imposed by the limitations of the inputs. These limitations make the equality (3.16) to be very restrictive and hard to be achieved. The optimization (3.43) solves the optimal engineering parameters to reach the desired convergence rate α_2 in a less conservative way. Therefore, the closed-loop system is stable and the convergence rate varies in the range: $-\beta_1\mathcal{V} \leq \dot{\mathcal{V}} \leq -\beta_2\mathcal{V}$, depending on the limitations of the control inputs.

In the case where the system is divided into two components using singular perturbation theory, there are two objective functions that should be solved. The first one is to find the solution of the inputs for the feedback control of the slow component (3.30), and the

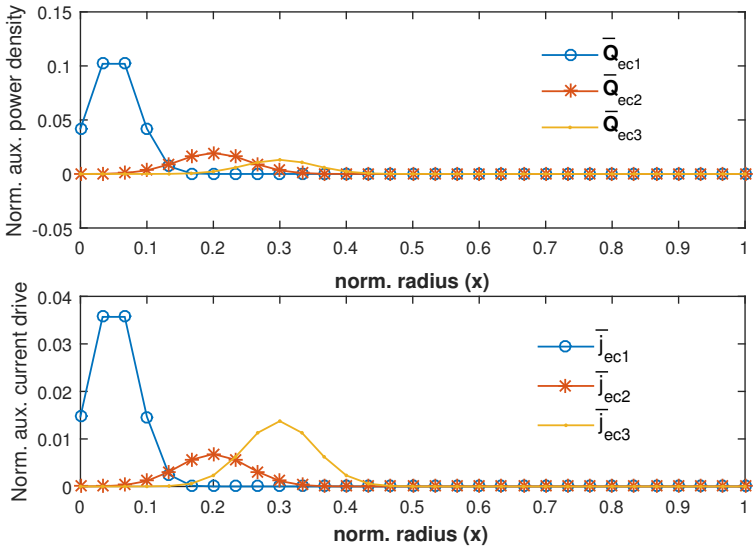


Figure 3.2: Normalized auxiliary electron cyclotron current-drive j_{dis} $(10^{20}\frac{m^{-5}A}{keVW})$ and Normalized auxiliary electron cyclotron power density Q_{dis} (m^{-3}) for the ITER configuration.

second one to find the optimal solution for the feedback control of the fast component (3.38). Thus, the following multi-objective optimization problem is formulated:

$$\begin{aligned} arg\ \min_{\tilde{u}}\ \ & \omega_1 f_s(\tilde{u}_s) + \omega_2 f_f(\tilde{u}_f) \\ \text{subject to}: & -\alpha_4 \mathcal{V}_s \leq f_s(\tilde{u}_s) \leq 0 \\ & -\alpha_6 \mathcal{V}_f \leq f_f(\tilde{u}_f) \leq 0 \\ & \tilde{u}_{min} \leq \tilde{u}_s + \tilde{u}_f \leq \tilde{u}_{max} \end{aligned} \tag{3.44}$$

where:

$$\begin{aligned} f_s(\tilde{u}_s) = & \int_0^1 x^2 p_s(x) \frac{\partial}{\partial x}\left(a_2(x)\tilde{T}_s + a_3(x)\frac{\partial \tilde{T}_s}{\partial x}\right)\tilde{z}dx \\ & + \int_0^1 x^2 p_s(x) \frac{\partial}{\partial x}\left(a_5(x)\tilde{j}_{aux}(\tilde{u}_s, x)\right)\tilde{z}dx \\ f_f(\tilde{u}_f) = & \int_0^1 x^2 p_f(x) b_5(x) \tilde{Q}_{aux,f}(\tilde{u}_f, x)\tilde{T}_f dx \end{aligned}$$

where the weights of the objectives $\omega_1, \omega_2 > 0$ are scaling parameters of the multi-objective optimization problem.

3.5 Results

3.5.1 TCV control

The control strategy presented in this chapter is tested using the nonlinear RAPTOR simulator with the parameters typical of the TCV tokamak. In the TCV configuration, the strategy presented in Section 3.1 is tested. Here the control strategy was based using only one control Lyapunov function without using singular perturbation theory. The control is calculated solving the optimization problem given in (3.43). In this configuration, the flat-top plasma current is set to a constant $I_p = 120kA$, while the EC antennas are used as control inputs. In the TCV simulations, the control inputs are represented by two EC heating and current drive antennas. One on-axis (P_{ec1}) and one off-axis (P_{ec2}), with current deposition width $\omega_{dep} = 0.35$ and location of the peak of the deposition $x_{dep} = 0$ for both clusters. The configuration of the reference values of $\overline{j}_{aux}$ and $\overline{Q}_{aux}$ is shown in Fig. 3.1. The linearized model is obtained by extracting the parameters of the model corresponding to a stationary state when a constant value of the powers of the antennas are applied with $P_{ec1} = 500kW$ and $P_{ec2} = 500kW$.
Using these plasma parameters, the Lyapunov function of the system was calculated using the method presented in Section 3 and the polynomials of the Lyapunov function were obtained as 5-th order Legendre polynomials. Their plots are presented in Fig. 3.3. The solver has been able to find the maximum value of $\alpha_1 = 0.03$ that provides some robustness margin. In Fig. 3.4a the evolution of the nominal system (zero inputs) is compared with the calculated exponential convergence rate $e^{-\beta_1 t}\mathcal{V}(0)$. In this plot we can see that the inequality is satisfied and that there is eventually another, larger value of the robustness margin, α_1 that can be found. With the calculation of the Lyapunov function, the stability of the dynamics of the system around the linearized point is proven and using the control Lyapunov strategy we can improve the performance by regulating the convergence rate.
To test the control approach, several reference profiles are extracted, with open-loop simulation, using different fixed values of the powers $\overline{P}_{ec1}$ and $\overline{P}_{ec2}$. The reference profiles are used as reference trajectories for the tracking control and the corresponding powers vector u are included as a feedforward input, e.g. $u = \overline{u} + \tilde{u}$.
Additionally, a third EC heating source was added with $x_{dep} = 0.2$ and $\omega_{dep} = 0.35$ that can be used as a source of disturbance in the system. When this input is activated, the robustness of the controller is tested with respect to deviations from the calculated equilibrium point. The power inputs are limited within the allowed range of: $0 \leq P_{ec1}(t) \leq 1MW$, $0 \leq P_{ec2}(t) \leq 1MW$.

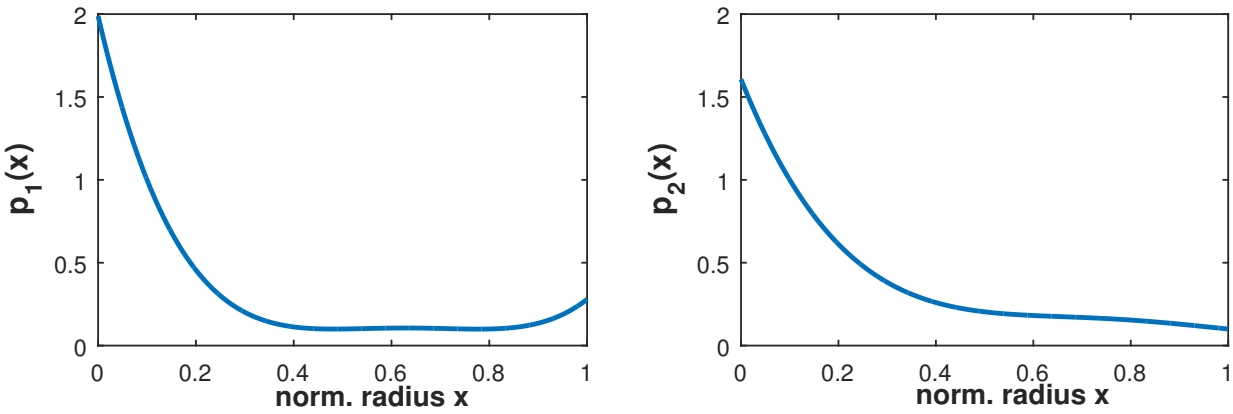
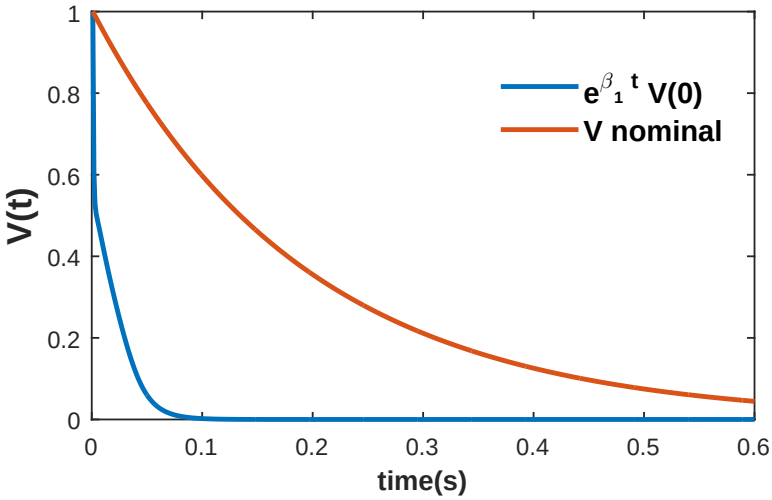
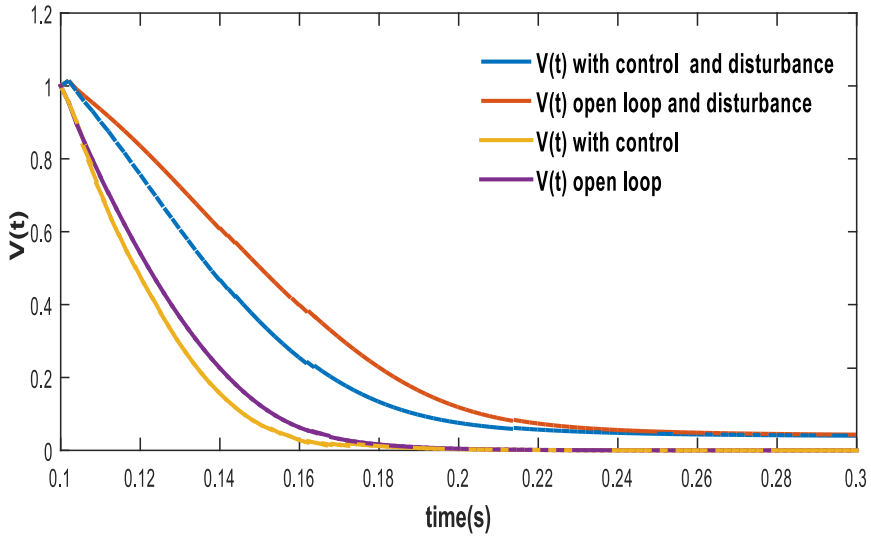


Figure 3.3: Numerical solution of $p_1(x)$ and $p_2(x)$ for TCV.



(a) Comparing the convergence rate of the nominal system with the calculated exponential convergence rate.



(b) Comparing the open loop and the closed loop convergence rates.

Figure 3.4: Time evolution of the normalized Lyapunov function in TCV simulations.

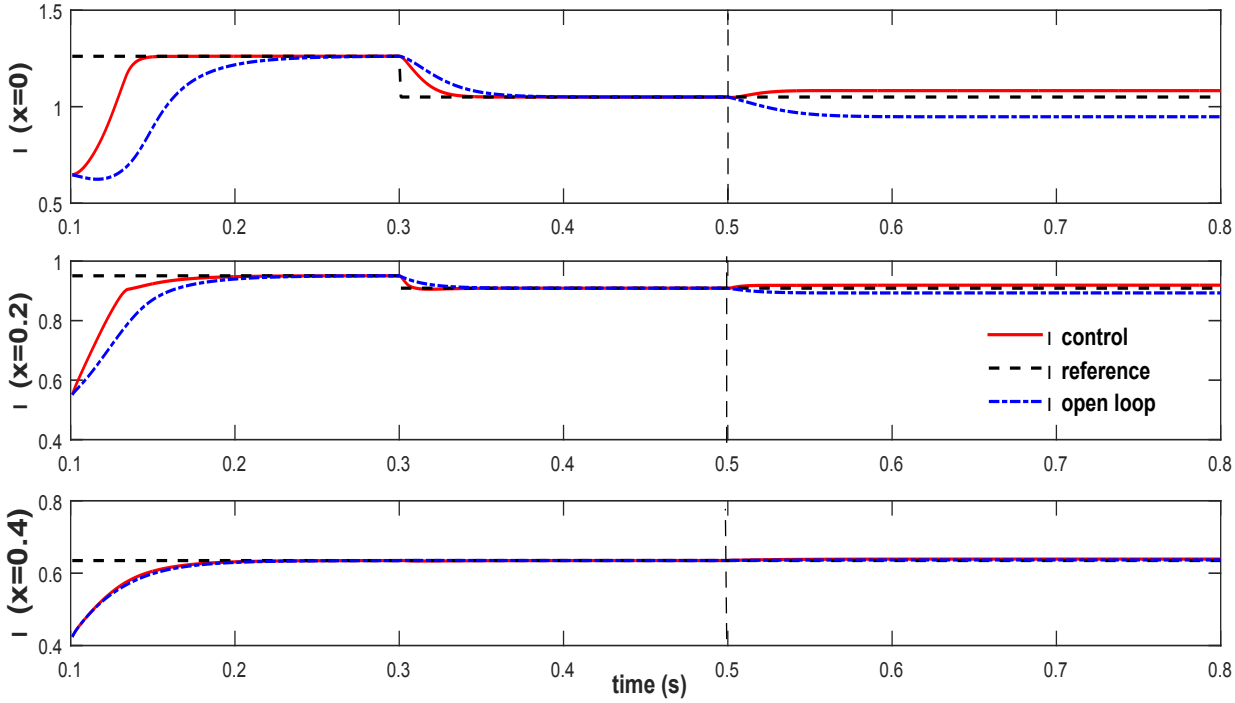


Figure 3.5: Evolution of ι on the TCV simulation. A disturbance is added at $t = 0.3$.

In Fig. 3.5 and Fig. 3.6 the results of one simulation are presented for ι and T_e tracking, respectively. Here the controller was tested starting from $0.1s$ and the results are compared with the performance of open-loop behavior of the system. The reference profile was changed at $0.3s$ to test the performance in the case where the values of the nonlinear plasma parameters are different from the values of the linearized model. Additionally, at $0.5s$ the third input representing the deviation from the equilibrium point was activated. The final values of the ι and T_e profiles are presented in Fig. 3.7. Comparing both performances it can be clearly seen that the feedback control gives better results and manages to attenuate better the offset that comes from the disturbances. The applied inputs of the controller are presented in Fig. 3.8. In Fig. 3.4b the time evolutions of the Lyapunov function for several cases are compared. In this figure, the convergence rates of the closed-loop and the open-loop system are compared in the cases with and without adding additional disturbance to the system. From this plot it can be concluded that in the both cases, the closed-loop system converges faster to the reference point than the open-loop system. The convergence rate of the closed-loop system is selected by tuning the value of α_2. Increasing the value of this parameter decreases the settling time and decreases the steady state error. However, if this gain is too large, the process variable will begin to oscillate and become unstable, also increasing this parameter leads to large input usage and larger overshoot of the fast-varying electron temperature.

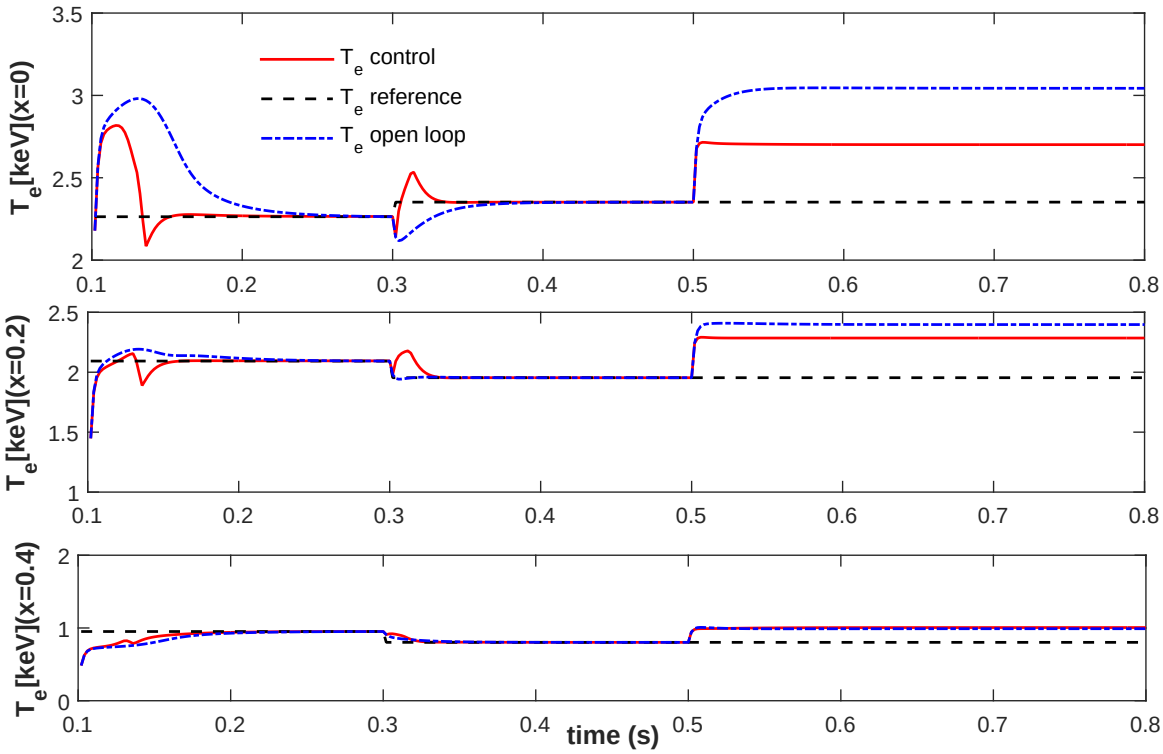


Figure 3.6: Evolution of T_e on the TCV simulation. A disturbance is added at $t = 0.3$.

3.5.2 ITER control

The control methods are evaluated and compared on a second tokamak by setting RAPTOR with a configuration based on the ITER machine in L-mode. Even though RAPTOR is not the most suitable simulator for ITER and the model is not as accurate as the one of TCV, this configuration is used to test the performance of the composite control in a large scale tokamak that has a larger difference in the time scales. In this configuration three EC antennas are used as actuators. The reference values of $\overline{j}_{aux}$ and $\overline{Q}_{aux}$ are presented in Fig. 3.2. The plasma current is set to a constant $I_p = 7\,\text{MA}$ and a linearized model is obtained by extracting the parameters corresponding to a stationary state when constant values of the powers of the EC antennas are $P_{ec1} = P_{ec2} = P_{ec3} = 7\,\text{MW}$. The input powers are limited in the range of 0 to 10 MW. As for the TCV simulations, several reference profiles are obtained to test the controller performance. An additional EC antenna is introduced to test the robustness with respect to deviations from the calculated equilibrium point.

Since both control methods necessitate a choice concerning the relative importance of the magnetic flux control with respect to the electrons heat control, we consider two control cases: Case 1 emphasizes the convergence rate of $\tilde{z}$ while $\tilde{T}_e$ is the priority for Case 2. Both

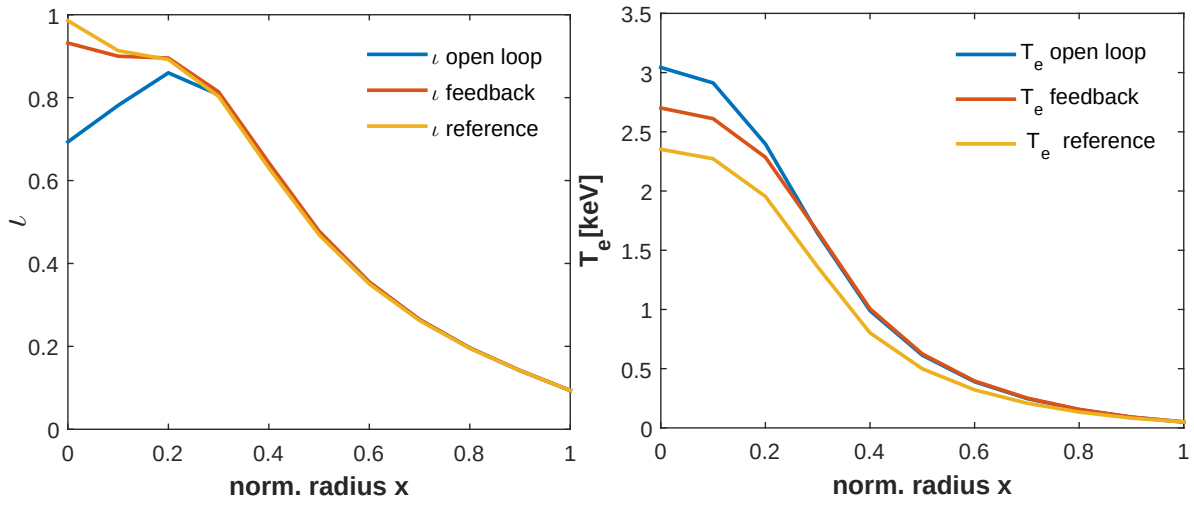


Figure 3.7: Comparison of the final values of ι and T_e obtained by open loop and using feedback control.

control methods are evaluated on each case.

We first implement the coupled control presented in Section 3.1. The convergence rate is set by the tuning parameter α_1 and the nature of the response depends highly on the choice of the scaling parameter γ (which multiplies $\tilde{T}_e$ in the Lyapunov function (3.2)). When γ is low (Case 1), the control is more effective for the performance of the slow variable $\tilde{z}$ while the convergence rate of T_e is difficult to tune (typically enduring high overshoots). When the value of γ is high (Case 2), the performance of the convergence rate of T_e can be tuned but the convergence rate of $\tilde{z}$ is free. To improve the convergence rate of $\tilde{z}$ we need in this case to increase the value of α_1, which induces oscillations in the T_e profile. The results from these simulations are presented in Fig. 3.9. While the convergence of ι and T_e is achieved in both control cases, the disparity in the convergence rates of the two dynamics renders the relative tuning particularly difficult to achieve, motivating the system decoupling approach.

We now apply the composite control presented in Section 3.2. The polynomials of the Lyapunov functions, presented in Fig. 3.12, are computed separately for the fast and the slow components. The maximum values of the convergence rate parameters are calculated numerically as $\alpha_4 = 0.01$ and $\alpha_7 = 9.3$. The difference between these two values was expected due to the difference in the time scales. The solution of the slow component of the temperature (3.17) is numerically calculated at each time instant and subtracted from $\tilde{T}_e$ to estimate the fast component of the temperature $\tilde{T}_f$. The output parameters $\iota(x,t)$ and $T_e(x,t)$ at several locations are presented in Fig. 3.10 (Case 1) and in Fig. 3.11 (Case 2) for the two control cases. For Case 1 a feedback control is applied only on the slow

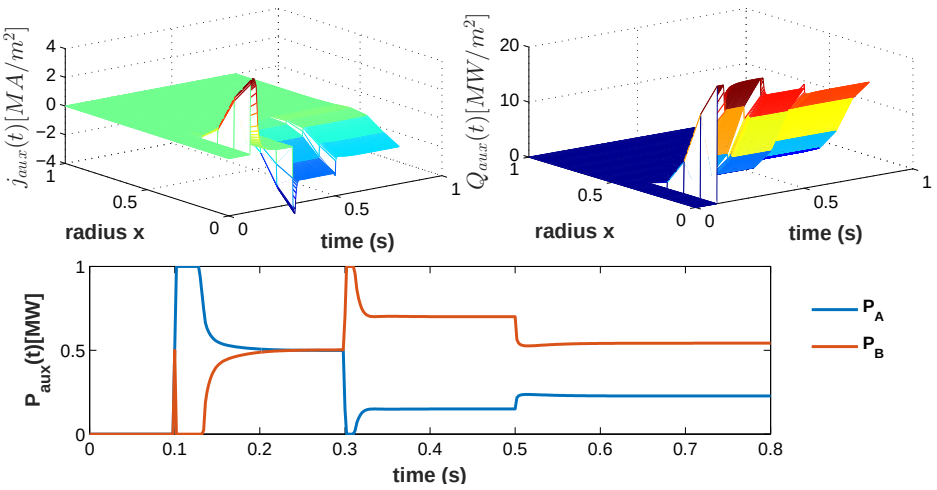


Figure 3.8: Evolution of the actual $j_{aux}(x,t)$ $[A/m^2]$ (top left) and $Q_{aux}(x,t)$ $[W/m^3]$ (top right) and $P_{aux}(t)$ (below) applied to the system in TCV.

component of the system. The results from this simulation have similar performance as in the case when the method presented in Section 3.1 is applied and low γ is used. For Case 2 the composite control combines the feedback control of the fast and slow components. The effect of the feedback control on the boundary layer system can be observed on $T_e(x,t)$: applying a control on the boundary layer system results in a reduced overshoot and a better convergence of the fast component at the cost of a slower convergence of the slow component. This behavior is also observed on the time-evolution of the slow and the fast Lyapunov functions starting from $t = 600s$ (when the reference profiles are changed) in Fig. 3.13. The controlled inputs for these simulations are presented in Fig. 3.15 (Case 1) and Fig. 3.14 (Case 2).

The tuning of the closed-loop performance with the composite control can be done by changing the values of the weighting parameters $\omega_{1,2}$ to obtain the desired balance between the two components. The convergence rate of the closed-loop system is selected by the choice of α_4 and α_6 for the performance of the slow and fast component, respectively. Increasing the value of α_4 decreases the settling time and decreases the steady state error of the slow component, but increases the overshoot of the electron temperature. By increasing the value of α_6 the convergence rate of the fast component is improved and the overshot of the electron temperature is decreased. If α_6 is increased further, it leads to high oscillations of the fast varying component. Note also that when the two control functions are calculated separately we can apply different sampling periods for the two parameters, which improves the computational efficiency and the performance of the feedback control.

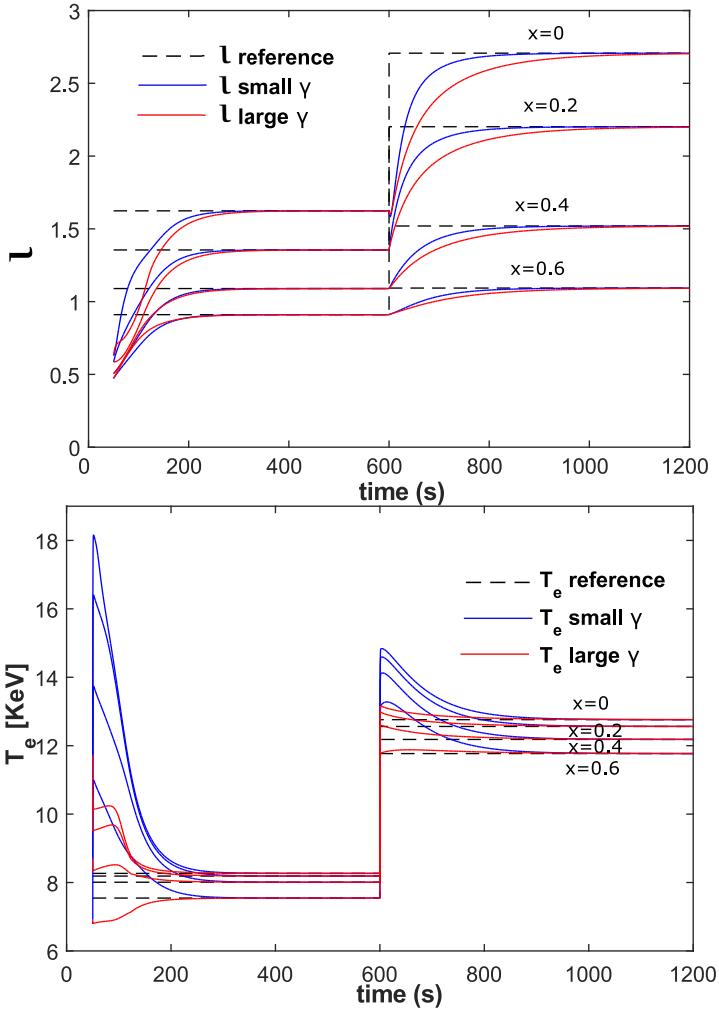


Figure 3.9: Evolution ι (top) and T_e (bottom) in the ITER simulation with the coupled controller and with convergence priority given to $\tilde{z}$ (Case 1, small γ) or $\tilde{T}_e$ (Case 2, large γ).

3.6 Conclusion of the chapter

An integrated feedback control algorithm for coupled current and electron temperature profiles was developed and tested in this chapter. The control is based on infinite dimensional settings by using a control Lyapunov strategy. The distributed control was applied on the two coupled 1D diffusion PDEs. The control-oriented model in this paper was developed using linearized simple models for the plasma evolution suitable for control applications. Because of the different time scales of the two parameters, a control strategy is developed by decoupling the two time scales of the system using singular perturbation theory. The control proposed in this chapter was tested using the non-linear RAPTOR

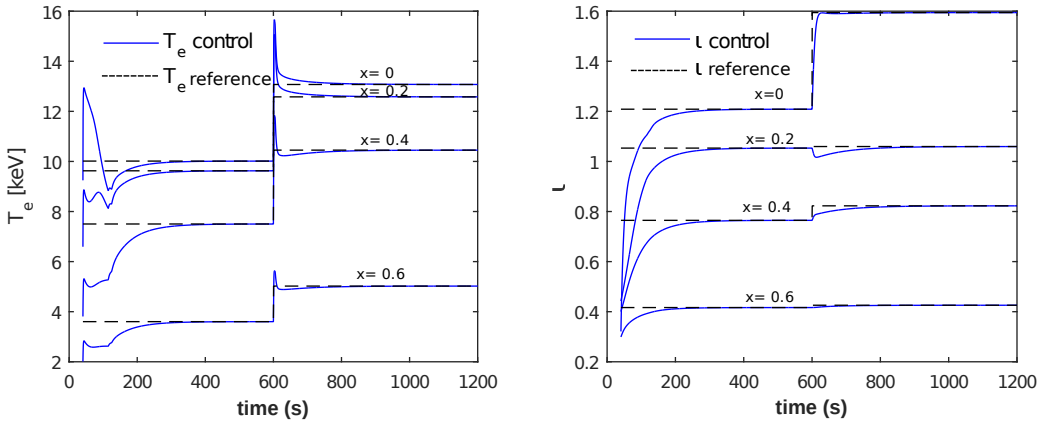


Figure 3.10: Evolution of T_e and ι in the ITER simulation (control case 1).

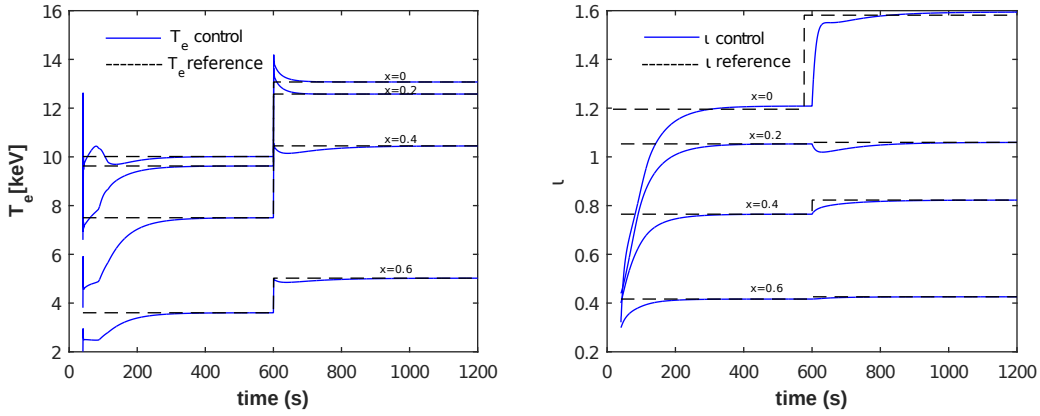


Figure 3.11: Evolution of T_e and ι in the ITER simulation (control case 2).

tokamak plasma simulator. The control was tested by using the configuration of the plasma parameters typical for the TCV and ITER tokamak machines. The different times scales in the two machines permit to test the two control strategies proposed in this work. In the future, these control strategies can be tested in a real tokamak. The state observer for the plasma profiles developed in (Felici, Baar, and Steinbuch, 2014) can be used to test the controller in TCV experiments. Additionally, the control strategy should consider the ohmic heating sources as a boundary input in some future work.

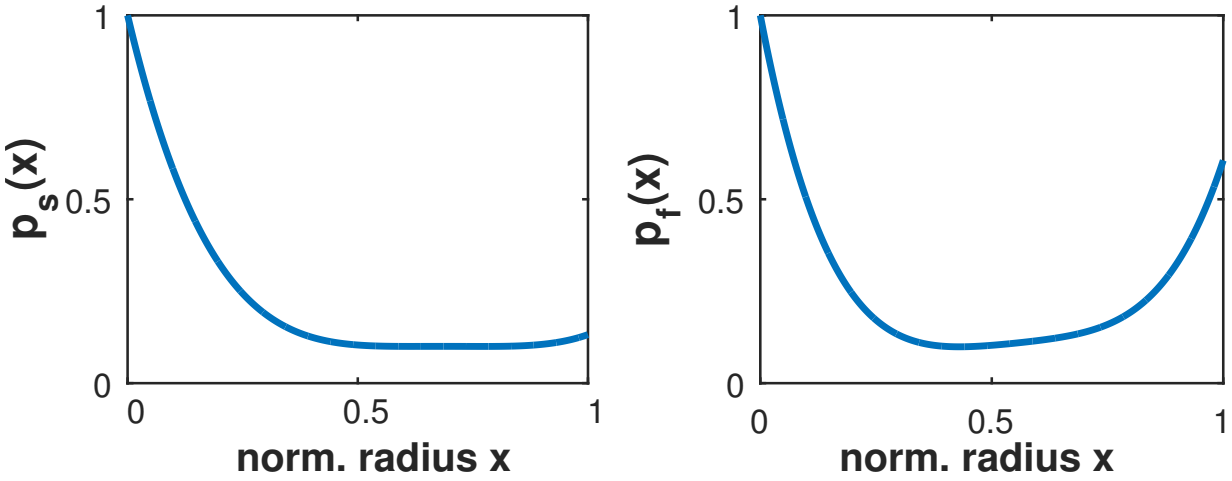


Figure 3.12: Numerical solution of p_s and $p_f(x)$.

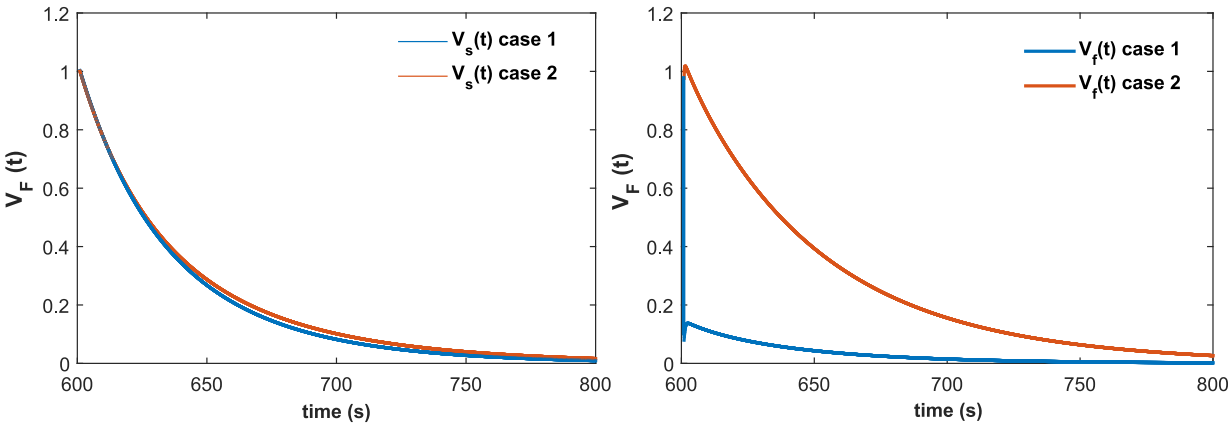


Figure 3.13: Time evolution of the two normalized Lyapunov functions V_s and V_f.

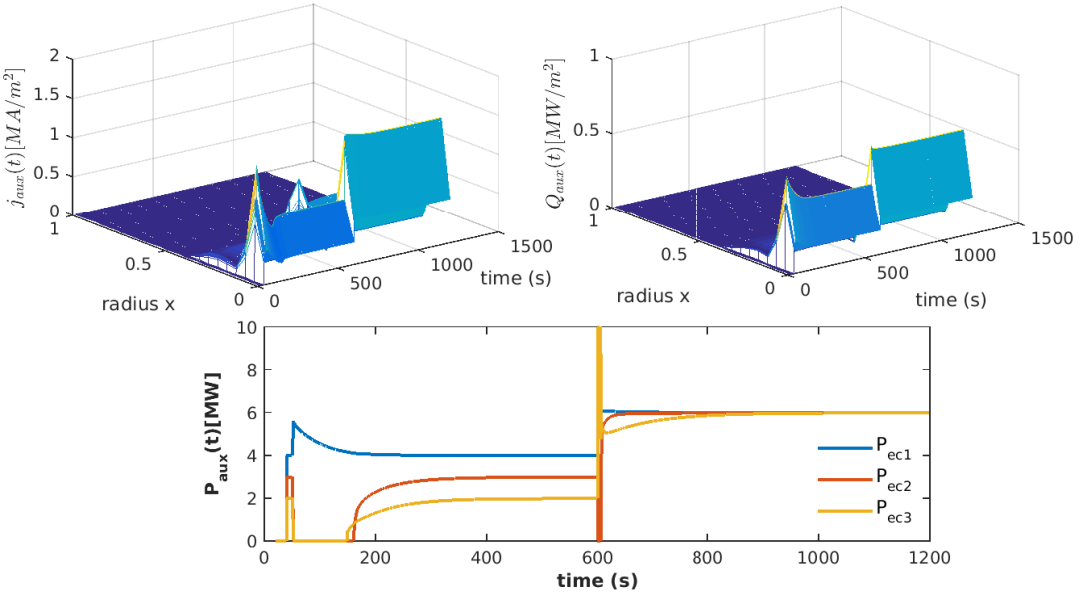


Figure 3.14: Evolution of the actual $j_{aux}(x,t)$ $[A/m^2]$ (top left) and $Q_{aux}(x,t)$ $[W/m^3]$ (top right) and $P_{aux}(t)$ (below) applied to the ITER configuration (Control case 1).

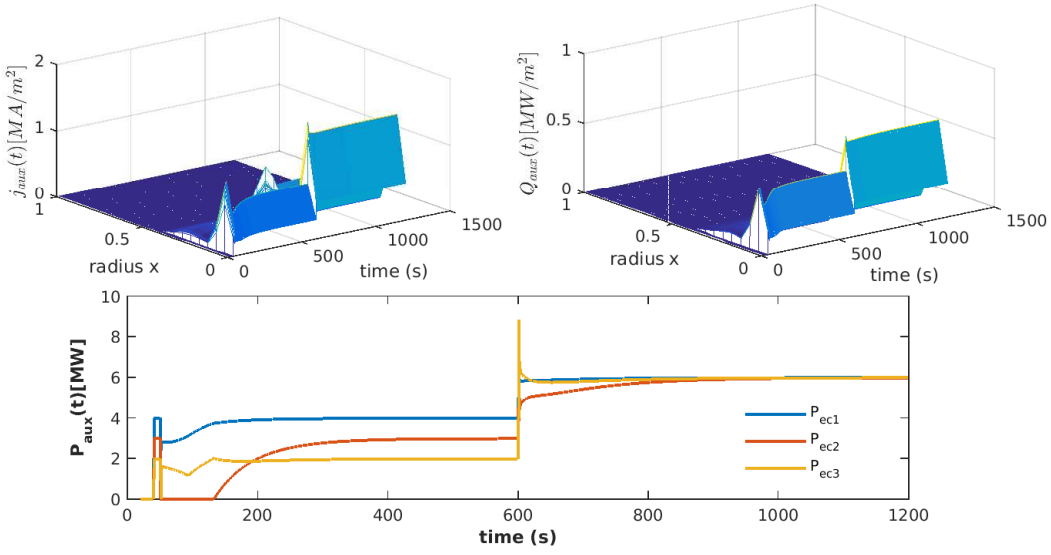


Figure 3.15: Evolution of the actual $j_{aux}(x,t)$ $[A/m^2]$ (top left) and $Q_{aux}(x,t)$ $[W/m^3]$ (top right) and $P_{aux}(t)$ (below) applied to the ITER confguration (Control case 2).

Chapter 4

Simultaneous control of the safety factor and the plasma β

Contents

4.1 Control problem and experimental settings 89

4.2 Distributed control 92

4.2.1 Stability of the closed loop system 93

4.2.2 Computation 95

4.3 Control of β 96

4.4 Anti-windup implementation 97

4.5 Control implementation 100

4.6 Results from the simulations 100

4.6.1 Presence of time delays 104

4.6.2 Change of the deposition location and width for P_{ec2} 106

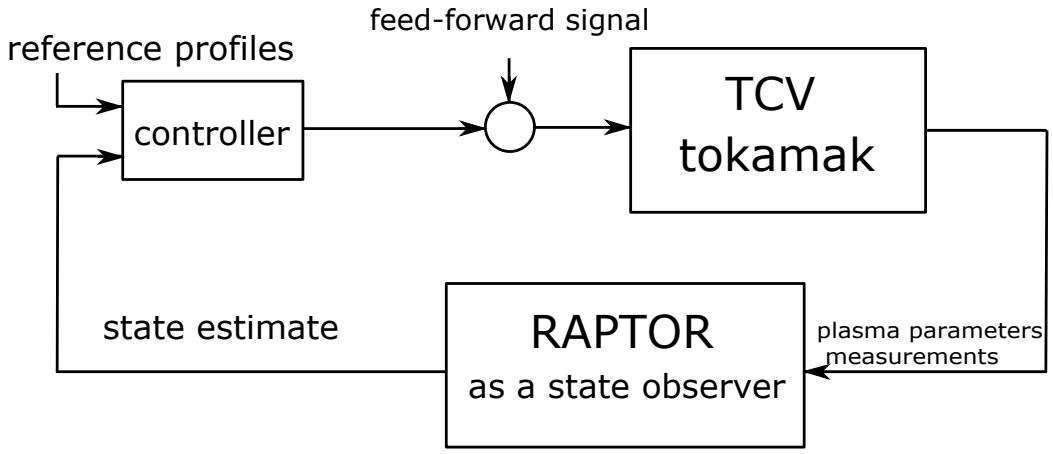
4.6.3 Disturbance attenuation 107

4.7 Conclusion on the chapter 110

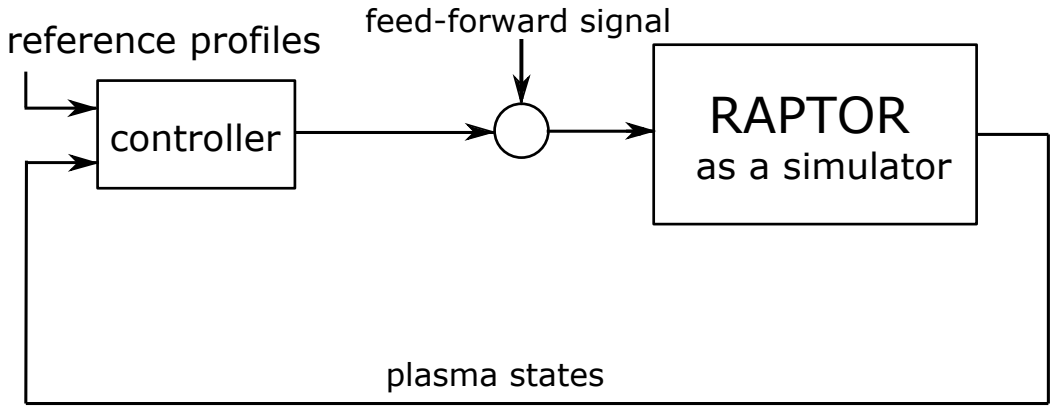
In this chapter model-based closed-loop algorithms are derived to control the inverse of the safety factor profile and the pressure parameter β. The control strategy presented in this chapter is applied to the configuration of the experimental setup for TCV tokamak. RAPTOR code is used as a state observer to estimate in real time the key plasma quantities. RAPTOR is developed to run in parallel with the TCV control system (Fig. 4.1a). This allows estimating the plasma profiles in many discretization points and also to estimate several unmeasurable quantities that are crucial for the control implementation. As it was demonstrated in the previous section, RAPTOR can also be used as a nonlinear plasma simulator (Fig. 4.1b). This enables to test the control algorithms before they are implemented in the real TCV experiments. The robustness and performance of the controller can be tested in simulations considering different scenarios that can affect the performance

of the control algorithms when they are applied in the real TCV control system.

There are several works already dedicated to the simultaneous control of the safety factor and the pressure parameters for advanced tokamak scenarios. In (Moreau et al., 2013) successful closed-loop experiments are performed for the simultaneous control of the relative internal poloidal flux profile Ψ_r together with the normalized pressure parameter, β_N. Here the control-oriented model is obtained from experimental data using a generic two time-scale method. Simultaneous control of q profile and β_N using first-principles-driven physics-based model is developed for DIII-D H-mode scenarios in (Barton et al., 2015a) and for ITER burning plasma H-mode scenarios in (Barton et al., 2013; Barton et al., 2015b). The infinite dimensional models used in this work are spatially discretized by employing a finite difference method. The control was developed using robust feedback control algorithms for finite dimensional systems.
The model used in this chapter is represented by a coupled system of one 1D resistive diffusion (ι control) and a nonlinear ordinary differential equation (β control). In contrast with the previous works dedicated to simultaneous control of the safety factor and the pressure parameters (Barton et al., 2015b; Barton et al., 2015a), here the control of the safety factor profile is based on infinite dimensional settings. Due to the different times scales of two quantities, the control was synthesized by designing separate control algorithms for the fast and the slow components. The control algorithm of the slow component represented by z-profile is similar to the proportional-integral controller proposed in (Gaye et al., 2013a) where the internal poloidal flux profile, Ψ_r, is used for control design. When integral action is presented in the control with a saturated actuator, it may cause the well-known phenomenon of integrator windup. To avoid the drawbacks from the actuator saturation in the system, an anti-windup compensator is added to the control design. Stability and anti-windup techniques for systems with saturated actuators are synthesized as in (Tarbouriech et al., 2011; Bohn and Atherton, 1995).
In the last section of this chapter the results from the control simulations using RAPTOR are presented. The robustness and performance of the control algorithms are tested using several scenarios. In these scenarios different plasma parameter uncertainties and disturbances are considered.



(a) A state observer based on RAPTOR is used for a real TCV tokamak control application. The plasma state is reconstructed from the available measurements.



(b) RAPTOR used as a plasma simulator. The simulated plasma state is obtained directly from RAPTOR.

Figure 4.1: Fast control oriented plasma profile evolution code RAPTOR.

4.1 Control problem and experimental settings

In the TCV experimental setup, two ECCD antennas are used to generate both the non-inductive current and the external heating source. The configuration of these two ECCD antennas is the same as the one presented in the TCV experiments in Chapter 3. Here $P_{aux,1}$ is used as a co-current source (to increase the total plasma current) and the second one $P_{aux,2}$ as a counter-current source (to decrease the total plasma current). The current deposition width and the location of the peak are as the one presented in Fig. 3.1. In the particular case when the two antennas are used with same deposition profile, the following

change of variables can be done:

$$\begin{aligned} u_\iota &= c_{dc,1}P_{aux,1} + c_{dc,2}P_{aux,2} \\ u_\beta &= P_{aux,1} + P_{aux,2} \end{aligned} \tag{4.1}$$

where $c_{dc,1}$ and $c_{dc,1}$ are parameters quantify the efficiency of current drive for $P_{aux,1}$ and $P_{aux,2}$, respectively. This change of variables permits to divide the control signals, u_ι for the non-inductive current deposition and the control of ι profile, and u_β as external heating source for the control of β.
The control of the inverse of the ι profile is performed by controlling the $\tilde{z}$ profile. The model used for the control is considered as the one presented with (1.26) and considering that the total plasma current is fixed to $I_p(t) = \overline{I}_p$:

$$\left\{ \frac{\partial \tilde{z}}{\partial t} = \frac{\partial}{\partial x}\left(\frac{\overline{\eta}_\parallel}{\mu_0 a^2 x} \frac{\partial}{\partial x}(x\tilde{z}) \right) + \frac{\partial}{\partial x}(\overline{\eta}_\parallel R_0 \tilde{j}_{ni}) \right. \tag{4.2}$$

with boundary conditions:

$$\begin{aligned} \tilde{z}(0,t) &= 0, \forall t \geq 0 \\ \tilde{z}(1,t) &= 0, \forall t \geq 0 \end{aligned} \tag{4.3}$$

with initial conditions:

$$\tilde{z}(x,0) = \tilde{z}_0, \forall x \in [0,1] \tag{4.4}$$

where $\tilde{j}_{ni} = \tilde{j}_{aux}(\tilde{u}_{\iota,x,t}) + \tilde{j}_{bs}(x,t)$. Here the profile of auxiliary current $\tilde{j}_{aux}(\tilde{u}_{\iota,x,t})$ is modeled by the weighted Gaussian distribution presented in subsection 3.4.1 and can be controlled by the power of the ECCD antennas, whereas for the sake of simplicity $\tilde{j}_{bs}(x,t)$ can be considered as an external disturbance to be attenuated/compensated.
The parameter $\eta_\parallel(x,t)$ highly depends on the electron temperature (1.7) and it varies in time. For control design purposes, the values of this parameter can be approximated to be in a given range:

$$\eta_\parallel(x,t) = \omega_\eta(t)\eta_{\parallel,min}(x) + (1 - \omega_\eta(t))\eta_{\parallel,max}(x), \text{ for all } t \geq 0 \tag{4.5}$$

where $\omega_\eta(t) \in [0,1]$ and $\eta_{\parallel,min}$ and $\eta_{\parallel,max}$ are the minimum and the maximum values of $\eta_\parallel$, respectively and are presented in Fig. 4.2.
The control of the plasma parameter β is done by using the simplified first order ODE of the approximate stored energy W. The plasma β and W are considered to be proportional and the relation between them is given in (1.31). The equation of evolution of W is given by:

$$\frac{dW}{dt} = -\frac{W}{\tau_{th}} + P_{tot} \tag{4.6}$$

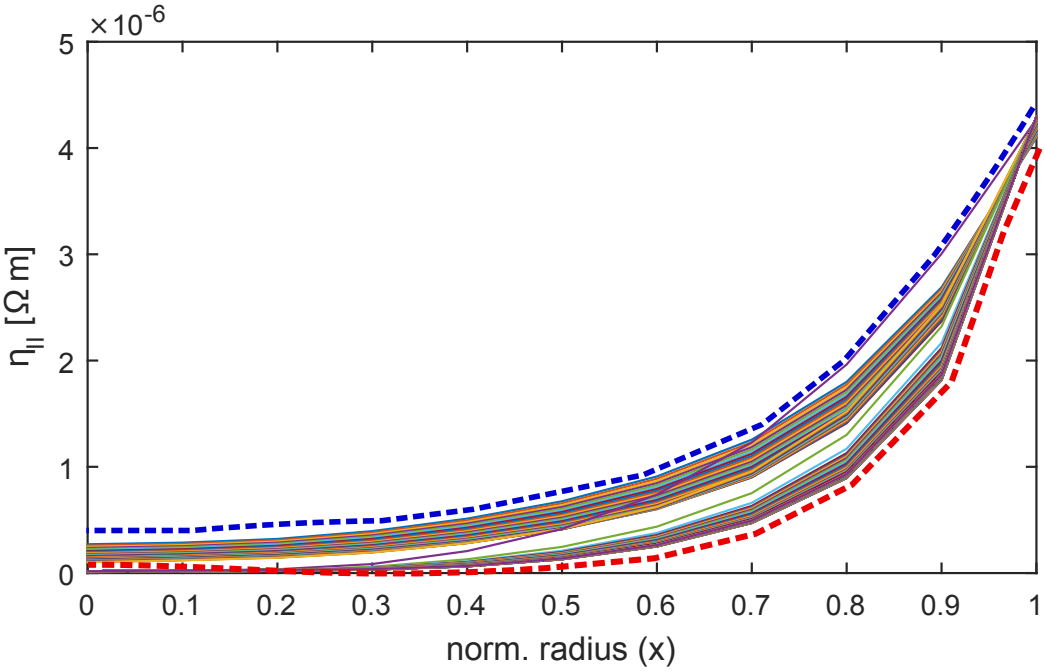


Figure 4.2: $\eta_{||}$ parameter ranges with the minimum value (red dash line) and the maximum value (blue dash line)

where τ_{th} is given in (1.35) and P_{tot} can be presented as a sum of several components:

$$P_{tot}(t) = P_{OH}(t) + P_{aux}(t) - P_{rad}(t) + P_{ei}(t) = P_{OH}(t) + u_\beta - P_{rad}(t) + P_{ei}(t) \tag{4.7}$$

where P_{OH} is the ohmic power, P_{ei} is electron-ion loss power and P_{rad} is radiation loss power. The control input in this equation is presented by u_β which is controlled by the two ECCD antennas. The other nonlinear parameters, $\tilde{P}_{ei}(t), \tilde{P}_{OH}(t), \tilde{P}_{rad}(t)$ and other non-modelled sources can be considered as disturbances in the system. For the evolution of the β we assume that only the fast dynamics is dominant. Thus, the control is computed using fast time scale $\tau = \epsilon t$, where ϵ represents the typical ratio between the energy confinement time and the characteristic resistive diffusion time in TCV (approximately $\varepsilon = 0.06$). The simplified linearized model of (4.6) around the steady state $(\overline{W}_{th}, \overline{z}, \overline{T}_e, \overline{u}_\beta, \overline{I}_p)$ is presented as :

$$\frac{d\tilde{W}}{d\tau} = -\frac{\tilde{W}}{\overline{\tau}_{th}} + \tilde{u}_\beta + k_{Ip}\tilde{I}_p + \omega \tag{4.8}$$

where $k_{Ip} = -\frac{\partial \overline{W}/\overline{\tau}_{th}}{\partial \overline{I}_p} + \frac{\partial \overline{P}_{tot}}{\partial \overline{I}_P}$ and ω represents the external disturbance in the system. The parameter $\overline{\tau}_{th}$ can be assumed to be bounded as $\overline{\tau}_{min} \leq \overline{\tau}_{th} \leq \overline{\tau}_{max}$.
Although there is a coupling between the dynamics of these two parameters ($\tilde{z}$ and $\tilde{\beta}$), the control action is computed separately. Because of the different time scales, the controller

synthesis for the two parameter is divided. Moreover, the change of variables presented in (4.1) permits to decouple the control signal and to compute the slow and the fast component separately.

Since T_e is not considered as a control output in this setup, the evolution of T_e is not included explicitly in the feedback control design and the stability analyses. The terms in the both equations that depend on T_e profile are considered to be uncertain or considered as a external disturbance to be attenuated/compensated by the feedback control algorithm. An proportional integral action is introduced in the controller design to reduce the steady state error and to improve the robustness.

4.2 Distributed control

The feedback-control of the z-profile is determined such that the control parameter $\tilde{j}_{ni,fb}$ is calculated as:

$$\tilde{j}_{ni,fb}(x,t) = \frac{1}{\overline{\eta}_{||} R_0}\left(-\int_0^x \alpha_p(x)\tilde{z}dr + \int_0^x \mathcal{I}dr \right) \tag{4.9}$$

where $\mathcal{I}$ is the integral action of the controller, and $\alpha_p(x)$ and $\alpha_I(x)$ correspond to the proportional and the integral gain of the control, respectively. The integral action of the control is calculated as:

$$\frac{\partial \mathcal{I}}{\partial t} = -\alpha_I(x)\tilde{z} - \lambda(t)\mathcal{I} \tag{4.10}$$

The parameter $\lambda_{max} \geq \lambda(t) \geq 0$ in the integral action is called a "forgetting factor" for the integrator (Bribiesca Argomedo et al., 2010). This parameter is used to cancel high overshoots that can appear as results of the integral action when the operation point is changed. This integral vanishes in finite time to avoid a steady-state error ($\lambda(t) \to 0$ when $t \to \infty$). In the simulations the value of this parameter is selected as $\lambda(t) = \kappa e^{-\sigma t^2}$, where κ and σ are chosen constant parameters.

The closed-loop system (4.2) when the feedback control (4.9) applies, has the dynamics:

$$\begin{cases} \dfrac{\partial \tilde{z}}{\partial t} = \dfrac{\partial}{\partial x}\left(\dfrac{\overline{\eta}_{||}}{\mu_0 a^2 x}\dfrac{\partial}{\partial x}(x\tilde{z}) \right) - \alpha_p(x)\tilde{z} + \mathcal{I} \\ \dfrac{\partial \mathcal{I}}{\partial t} = -\alpha_I(x)\tilde{z} - \lambda(t)\mathcal{I} \end{cases} \tag{4.11}$$

with boundary conditions:

$$\begin{aligned} \tilde{z}(0,t) &= 0, \ \forall t \geq 0 \\ \tilde{z}(1,t) &= 0, \ \forall t \geq 0 \end{aligned} \tag{4.12}$$

The parameters of the controller should be tuned such that the closed-loop system is asymptotically stable.

4.2.1 Stability of the closed loop system

To compute the stability of the closed-loop system (4.11), the following candidate Lyapunov function is chosen:

$$\mathcal{V} = \mathcal{V}_z + \mathcal{V}_I \tag{4.13}$$

where

$$\mathcal{V}_z = \frac{1}{2}\int_0^1 x^2 p_z(x)\tilde{z}^2 dx \tag{4.14}$$

and

$$\mathcal{V}_I = \frac{1}{2}\int_0^1 x^2 p_I(x)\mathcal{I}^2 dx \tag{4.15}$$

Theorem 5
Suppose that for a given positive value γ_1 and a time-varying positive numbers γ_1 and $\gamma_2(t)$ there exist polynomials $k_z, k_I, p_z, p_I \in \mathbb{R}$ such that $p_z(x) > 0$ and $p_I(x) > 0$ for all $x \in [0,1]$. If the following inequality is verified:

$$A(x) + A_1(x) \leq 0 \tag{4.16}$$

where

$$A(x) = \begin{bmatrix} a_{1,1}(x) & a_{1,2}(x) & a_{1,3}(x) \\ 0 & a_{2,2}(x) & 0 \\ a_{1,3}(x) & 0 & a_{3,3}(x) \end{bmatrix} \tag{4.17}$$

$$\begin{aligned} a_{1,1} &= -\frac{\overline{\eta}_{||}}{\mu_0 a^2}\Big(2p_z(x) + xp_z'(x)\Big) - k_z(x)x^2 \\ a_{2,2} &= -\frac{\overline{\eta}_{||}}{\mu_0 a^2}x^2 p_z(x) \\ a_{1,2} &= -\frac{1}{2}\frac{\overline{\eta}_{||}}{\mu_0 a^2}\Big(x^2 p_z'(x) + 3xp_z(x)\Big) \\ a_{1,3} &= \frac{1}{2}x^2\Big(p_z(x) - k_I(x)\Big) \\ a_{3,3} &= -x^2 p_I(x)\lambda(t) \end{aligned} \tag{4.18}$$

and

$$A_1(x) = \frac{1}{2}\begin{bmatrix} \gamma_1 x^2 & 0 & 0 \\ 0 & 0 & 0 \\ 0 & 0 & \gamma_2(t)x^2 \end{bmatrix} \tag{4.19}$$

then the time derivative $\dot{\mathcal{V}}$ *of* $\mathcal{V}$ *defined in (4.13) along the solutions (4.11) and (4.12) verifies:*

$$\dot{\mathcal{V}} \leq -\gamma(t)\mathcal{V} \tag{4.20}$$

where

$$\gamma(t) = \frac{min(\gamma_1, \gamma_2(t))}{\underset{x\in[0,1]}{min}(p_z(x), p_I(x))} \tag{4.21}$$

Proof. The time-derivative of the Lyapunov function is:

$$\dot{\mathcal{V}} = \dot{\mathcal{V}}_z + \dot{\mathcal{V}}_I \tag{4.22}$$

where

$$\begin{aligned}\dot{\mathcal{V}}_z(t) &= \int_0^1 x^2 p_z(x)\frac{\partial \tilde{z}}{\partial t}\tilde{z}dx \\ &= \int_0^1 x^2 p_z(x)\frac{\partial}{\partial x}\left(\frac{\overline{\eta}_{||}}{\mu_0 a^2 x}\frac{\partial}{\partial x}(x\tilde{z})\right)\tilde{z}dx \\ &\quad - \int_0^1 x^2 p_z(x)\alpha_p(x)\tilde{z}^2dx + \int_0^1 x^2 p(x)\tilde{z}\mathcal{I}dx\end{aligned} \tag{4.23}$$

Applying integration by parts in $\dot{\mathcal{V}}_z(t)$ and defining $k_z(x) = \alpha_p(x)p_z(x)$ we get:

$$\begin{aligned}\dot{\mathcal{V}}_z(t) =& xp_z(x)\tilde{z}\frac{\overline{\eta}_{||}}{\mu_0 a^2}\frac{\partial}{\partial x}\big(x\tilde{z}\big)\Big|_0^1 - \int_0^1 x^2 p_z(x)\frac{\overline{\eta}_{||}}{\mu_0 a^2}\left(\frac{\partial \tilde{z}}{\partial x}\right)^2 dx \\ &- \int_0^1 \left(2p_z(x) + xp_z'(x)\right)\frac{\overline{\eta}_{||}}{\mu_0 a^2}\tilde{z}^2dx - \int_0^1 \left(x^2p_z'(x) + 3xp_z(x)\right)\frac{\overline{\eta}_{||}}{\mu_0 a^2}\tilde{z}\frac{\partial \tilde{z}}{\partial x}dx \\ &- \int_0^1 x^2 k_z(x)\tilde{z}^2dx + \int_0^1 x^2 p_z(x)\tilde{z}\mathcal{I}dx\end{aligned} \tag{4.24}$$

Calculating the time derivative of $\dot{\mathcal{V}}_I = \int_0^1 x^2 p_I(x)\frac{\partial \mathcal{I}}{\partial t}\mathcal{I}dx$ and defining $k_I(x) = \alpha_I(x)p_I(x)$, we get:

$$\dot{\mathcal{V}}_I(t) = -\int_0^1 x^2 k_I(x)\tilde{z}\mathcal{I}dx - \int_0^1 x^2 p_I(x)\lambda(t)\mathcal{I}^2dx \tag{4.25}$$

Combining the equations (4.24) - (4.25), $\dot{\mathcal{V}}$ can be presented as:

$$\dot{\mathcal{V}}(t) = \int_0^1 \begin{bmatrix} \tilde{z} \\ \frac{\partial \tilde{z}}{\partial x} \\ \mathcal{I} \end{bmatrix}^T \begin{bmatrix} a_{1,1}(x) & a_{1,2}(x) & a_{1,3}(x) \\ 0 & a_{2,2}(x) & 0 \\ a_{1,3}(x) & 0 & a_{3,3}(x) \end{bmatrix} \begin{bmatrix} \tilde{z} \\ \frac{\partial \tilde{z}}{\partial x} \\ \mathcal{I} \end{bmatrix} \tag{4.26}$$

where $a_{1,1}, a_{2,2}, a_{1,2}, a_{1,3}, a_{3,3}$ are defined in the statement of Theorem 5. Considering (4.16), we get $\dot{\mathcal{V}} \leq -\frac{1}{2}\gamma_1 \int_0^1 x^2 \tilde{z}^2 dx - \frac{1}{2}\gamma_2(t) \int_0^1 x^2 \mathcal{I}^2 dx$. This concludes the proof of Theorem 5. □

The time-varying parameter, $\gamma(t)$ decreases in time, $\gamma(t) \to 0$ when $t \to \infty$. In our analysis it is chosen to be equal to $\lambda(t)$, $\gamma_2(t) = \lambda(t) = \kappa e^{-\sigma t^2}$.

Corollary 5
Under the conditions of Theorem 5 and using the definition of $\gamma(t)$, the closed-loop system (4.11) with boundary condition (4.12) and initial conditions (4.4) is globally exponentially stable. The convergence rate of the system satisfies:

$$\mathcal{V}(t) \leq e^{-\int_0^t \gamma(r)dr} \mathcal{V}(\tilde{z}_0) \tag{4.27}$$

where $\gamma(t)$ is given in (4.21).

4.2.2 Computation

The exponential stability of the system is verified by solving inequality (4.16) in this theorem. The solution of this inequality is found as in section 3.1.1 by transforming the inequality in to an LMI problem by representing the weights of the Lyapunov functions, $p_z(x)$, $p_I(x)$ and the control gains $k_z(x), k_I(x)$ as Legendre polynomials. The LMI problem is formulated as follows:
For given parameters γ_1 and γ_2, find $p_z(x), p_I(x), k_z(x)$ and $k_I(x)$ such that:

- $A(x) + A_1(x) \leq 0, \forall x \in [0, 1]$;
- $0 < p_z(x) \leq p_{z,max}$ and $0 < p_I(x) \leq p_{I,max}, \forall x \in [0, 1]$;
- $\eta_{\|}(x) = \omega_\eta \eta_{\|,min}(x) + (1 - \omega_\eta)\eta_{\|,max}(x), \forall \omega_\eta \in [0, 1]$.

The LMI is solved to guarantee the stability of the closed-loop system for different values of $\lambda_{max} \geq \lambda(t) > 0$. The LMI solver is used to find the unknown constant polynomial coefficients in $p_z(x), p_I(x), k_z(x)$ and $k_I(x)$.

4.3 Control of β

The control synthesis for β parameter is developed using only the auxiliary heating sources as system input, given by $\tilde{u}_\beta$. The value of the plasma current during the experiments is considered as: $I_p(t) = \overline{I}_p$. If this quantity changes, it can be calculated and added to the value of ω. The dynamics equation used for β control thus corresponds to a single-input single-output (SISO) system. The transfer function representation of the SISO systems is most commonly used in control theory. Most of the control design of the SISO LTI systems is done by frequency domain mathematical techniques. The transfer function $g(s)$ of the system is the linear mapping of the Laplace transform of the input, $\mathcal{L}\{u_\beta(t)\} = u_\beta(s)$, to the Laplace transform of the output $\mathcal{L}\{\beta(t)\} = \beta(s)$. The transfer function of β parameter combining (4.8) with the relation (1.31) is calculated as:

$$g(s) = \frac{\tilde{\beta}(s)}{\tilde{u}_\beta} = \frac{k_\beta}{\overline{\tau}_{th}s + 1} e^{-\theta s} + \omega \tag{4.28}$$

where:

$$k_\beta = \overline{\tau}_{th} \frac{\beta}{W_{th}} = \frac{2\overline{\tau}_{th}}{3VB_0^2/(2\mu_0)} \tag{4.29}$$

and θ stands for the effective time delay, that is present in the real tokamak experiments and can affect the performance of the control of the fast variable. The effective delay in the TCV experiments can be up to 5 ms. The most common controllers used for SISO systems in the industrial application are the Proportional–Integral-Derivative PID controllers. These types of controllers are easy to be implemented. There are many works dedicated to the tuning of the parameters of the PID controllers for optimal performance of the closed-loop system. Such methods can be found in (Åström and Hägglund, 2006; Ziegler and Nichols, 1942). In this section the simple rule for PID tuning presented in (Skogestad, 2001) is used. This simple PID tuning rule is called Simple Internal Model Control (SIMC). In our application only P and I components are set since the dynamic of the system is presented by a first order Ordinary Differential Equation (ODE). The transfer function of the PI controller equation is given in cascade form as:

$$c(s) = \frac{\tilde{u}_{\beta,fb}}{\tilde{\beta}(s)} = -K_c \frac{\tau_I s + 1}{\tau_I s} \tag{4.30}$$

or presented in time domain:

$$\tilde{u}_{\beta,fb}(\tau) = -K_c\tilde{\beta}(\tau) - \int_0^1 \frac{K_c}{\tau_I}\tilde{\beta}(\sigma)d\sigma = -K_{\beta,p}\tilde{\beta}(\tau) - \int_0^t K_{\beta,i}\tilde{\beta}(\sigma)d\sigma \tag{4.31}$$

where $K_{\beta,p}$ is the proportional gain and $K_{\beta,i}$ is the integral gain of the controller. The coefficients of the controller are calculated as:

$$\begin{aligned} K_c &= \frac{1}{k_{beta}} \frac{\overline{\tau}_{th}}{\tau_c + \theta} = \frac{1}{k'_\beta} \frac{1}{\tau_c + \theta} \\ \tau_I &= \min\{\overline{\tau}_{th}, \frac{4}{k'_\beta K_c}\} = \min\{\overline{\tau}_{th}, 4(\tau_c + \theta)\} \end{aligned} \tag{4.32}$$

The SIMC PI-rule has one tuning parameter τ_c which can be used as a trade off between performance ("tight" control) and robustness ("smooth" control). The optimal tuning of this parameter and the performance of the PI SIMC method is discussed in (Grimholt and Skogestad, 2012).

4.4 Anti-windup implementation

The powers of auxiliary antennas used in the tokamak machines are subject to saturation. The saturation for the i-th actuator can be presented as:

$$sat(P_{aux,i}) = \begin{cases} P_{aux,i,min} & \text{if } P_{aux,i} < P_{aux,i,min} \\ P_{aux,i} & \text{if } P_{aux,i,min} \leq P_{aux,i} \leq P_{aux,i,max} \\ P_{aux,i,max} & \text{if } P_{aux,i} \geq P_{aux,i,max} \end{cases} \tag{4.33}$$

Integral windup can occur in loops where the actuator saturates and the controller has integral action. If the error remains positive for some time subsequent to saturation, the integrator continues to accumulate the error. When this happens, the controller output does not drive the plant and as a result, the states of the controller are wrongly updated. This effect is called controller windup. This can lead to large overshoots and undesirable transients.
To avoid windup, an extra feedback path is provided in the controller by measuring the actuator output and forming an error signal as the difference between the output of the controller and the actuator output. In the linear range, the error is integrated and the difference between the saturated and the unsaturated control signals is used to generate a feedback signal to properly control the integral state in the saturation range. Applying a tracking back calculation method (Visioli, 2003) on the control of the z component presented in (4.9), the integral component $\tilde{\mathcal{I}}$ is modified as:

$$\frac{\partial \tilde{\mathcal{I}}}{\partial t} = -\gamma_2(x)\tilde{z} - \lambda(t)\mathcal{I} + \gamma_3(x)\big(\tilde{j}_{ni} - \text{sat}(\tilde{j}_{ni})\big) \tag{4.34}$$

where the gain $\gamma_3(x)$ determines the rate at which the integral term is reset and its choice determines the performances of the overall control scheme.

In the case of the control of β, the feedback signal is presented as:

$$\tilde{u}_{\beta,fb} = -K_{\beta,p}\tilde{\beta} - \tilde{\mathcal{I}}_{\beta} \tag{4.35}$$

where the integral term is modified as:

$$\frac{d\tilde{\mathcal{I}}_{\beta}}{dt} = K_{\beta,i}\tilde{\beta} + K_{aw}\left(\tilde{P}_{\beta} - \text{sat}(\tilde{P}_{\beta})\right) \tag{4.36}$$

The gain K_{aw} determines the rate at which the integral term is reset, and its choice determines the performances of the overall control scheme.
Another way to apply anti-windup is by using the conditional integration (CI) technique that is presented in (Hanus, Kinnaert, and Henrotte, 1987; Hall, Hodel, and Hung, 1999). In the case where there is *a priori* knowledge of saturation levels of the signals and when a digital controller is used, this method can be effectively and easily implemented in the controller. In this technique, the integral term is increased only when certain conditions are satisfied; otherwise it is kept constant. In the case of the auxiliary heating sources in tokamak plasma, the CI is applied such that the integral action is suspended when the control inputs are saturated. In this case, the CI is calculated for each actuator separately. For the z component, the integral term $\tilde{\mathcal{I}}$ is frozen when the actuators saturate as:

$$\frac{\partial\tilde{\mathcal{I}}}{\partial t} = \begin{cases} 0 \ \text{ if } e(\tilde{u}_{\iota} - \tilde{u}_{\iota,des}) > 0 \\ \gamma_2(x)\tilde{z} \ \text{ otherwise} \end{cases} \tag{4.37}$$

where $e(\tilde{u}_{\iota} - \tilde{u}_{\iota,des})$ is the error between the desired control command $u_{\iota,des}$ and the actuators output $\tilde{u}_{\iota}$.
In the case of the controller of β, the integral term $\tilde{\mathcal{I}}_{\beta}$ is frozen when the actuators is being driven into saturation:

$$\frac{d\tilde{\mathcal{I}}_{\beta}}{d\tau} = \begin{cases} 0 \ \text{ if } e(\tilde{u}_{\beta} - \tilde{u}_{\beta,des}) > 0 \\ K_{\beta,i}\tilde{\beta} \ \text{ otherwise} \end{cases} \tag{4.38}$$

where $e(\tilde{u}_{\beta} - \tilde{u}_{\beta,des})$ is the error between the desired control command $\tilde{u}_{\beta,des}$ and the actuators output $\tilde{u}_{\beta}$.
Fig. 4.3 and Fig. 4.4 present the closed-loop simulations of the outputs β and ι, respectively. The tracked outputs of these parameters are compared with and without CI anti-windup applied. In the time interval $t \leq 0.3\ s$ the reference values of the outputs were selected such that the system actuators are forced to reach a saturation level. During this interval the integrator continues to accumulate the error if no anti-windup scheme is applied. After $t = 0.3\ s$ the target values are changed and the performance of the anti-windup technique can be tested. In the case when the anti-windup technique is not applied, there are delays in the controllers response to the change of the reference signal. From these results it can be concluded that the simple CI technique deals effectively with the controller windup problem.

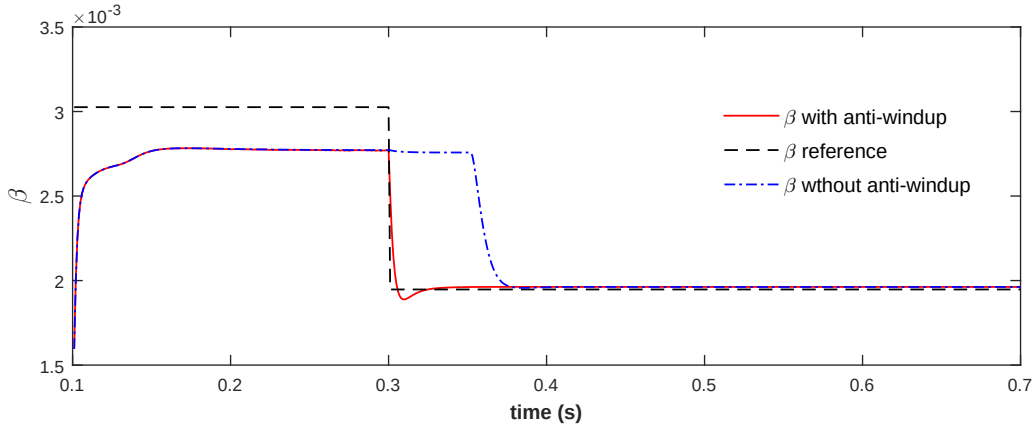


Figure 4.3: Comparison of the performance of the control of β without (blue dash line) and with (red line) the application of an anti-windup scheme.

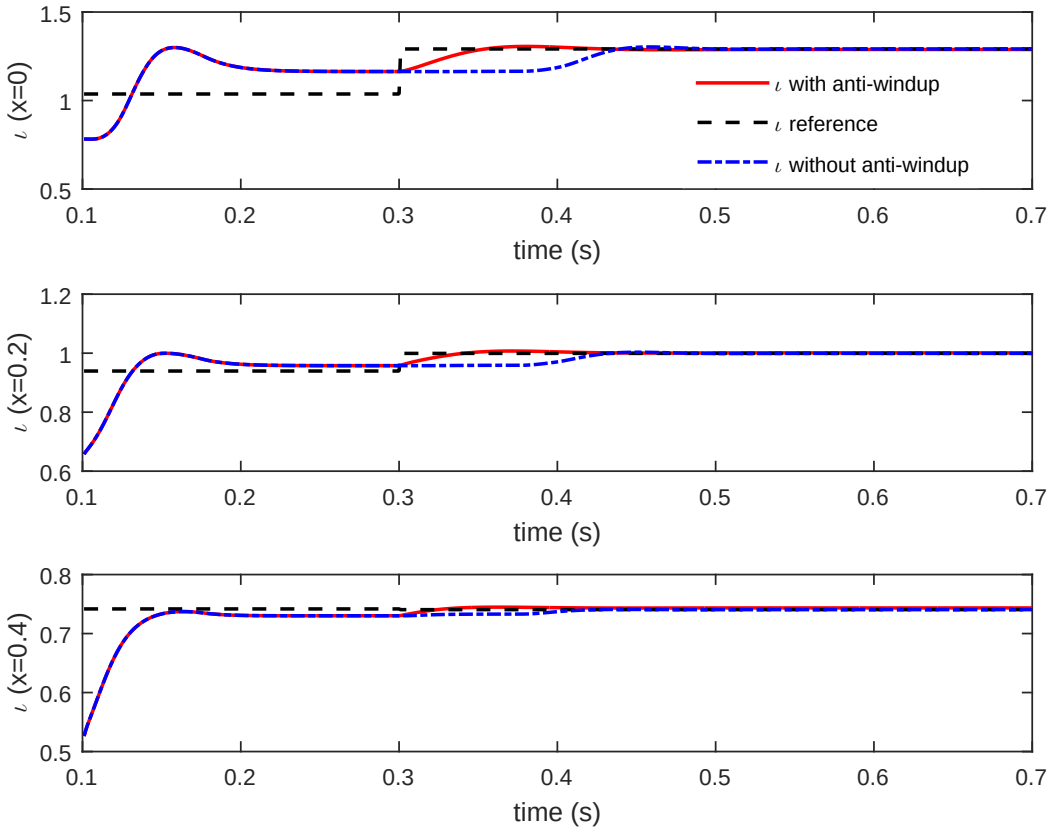


Figure 4.4: Comparison of the performance of the control of ι with (blue dash line) and without (red line) the application of an anti-windup scheme.

4.5 Control implementation

As in the previous chapter, only the auxiliary powers P_{aux} are used as control input in the system. This leads to limited shapes of the current density profile due to the limited degrees of freedom of the actuators. An optimization problem should be formulated to fit the desired current density control calculated in this section with the achievable current density profile. Similarly to the previous chapter, the control is solved such that a multi-objective optimization problem is formulated to deal with the simultaneous control of several parameters. The control inputs $\tilde{u} = [\tilde{P}_{aux,1}\ \tilde{P}_{aux,2}]$ are calculated using an optimization algorithm to minimize the criterion (Gaye et al., 2013a):

$$arg\ \min_{\tilde{u}}\ \ \omega_1 f_z(\tilde{u}_\iota) + \omega_2 \tilde{u}_\beta \tag{4.39}$$

subject to

$$\begin{aligned} \tilde{P}_{1,min} \leq \tilde{P}_{aux,1} \leq \tilde{P}_{1,max} \\ \tilde{P}_{2,min} \leq \tilde{P}_{aux,2} \leq \tilde{P}_{2,max} \end{aligned} \tag{4.40}$$

where:

$$f_z(\tilde{u}_\iota) = \int_0^1 \left(\tilde{\tilde{j}}_{ni,des} - \tilde{\tilde{j}}_{ni,mod}(\tilde{u}_\iota) \right)^2 \tag{4.41}$$

here $\tilde{\tilde{j}}_{ni,des}$ is the desired control calculated in (4.9) and $\tilde{\tilde{j}}_{ni,mod}(\tilde{u}_\iota)$ is the current profile that can be achieved by using the available actuators in this experimental setup. The model presented in (3.39) and (3.40) is used for modeling the current densities of the ECCD antennas, $\tilde{\tilde{j}}_{aux,mod}(\tilde{u}_\iota)$ that are used as control inputs. The parameters ω_1 and ω_2 are used as weighting parameters in the multi-objective optimization. They can be used to tune the priority of the control of one of the plasma parameters. The nominal values of these parameter are set as $\omega_1 = \omega_2 = 0.5$ to give equal priority to both plasma parameters. There weighting parameters can be changed according to the different control objectives. In (4.39), $\tilde{u}_\beta$ is the desired control of the β component calculated in (4.31).

4.6 Results from the simulations

The control strategy presented in this chapter is developed for the parameters of the TCV tokamak machine. The control algorithm should be tested using the rapid nonlinear plasma RAPTOR simulator before applying the control in the real TCV experiments. Several control scenarios are considered to examine the robustness and the performance of the controller. The configuration of the ECCD antennas that are used as control inputs are

similar to the ones that were used in Chapter 3. To test the performances of the controller, the ECCD antennas were considered to have broad power limits of $0 \leq P_{ec1}(t), P_{ec2}(t) \leq 1MW$. These values may change in the real TCV experiment where some cluster may have narrower power limitations. The configuration of the reference values of the current and power distribution are the same as in the previous chapter and are presented in Fig. 3.1. The flat-top value of the plasma current is fixed to $I_p = 120\ kA$. The bounds of the $\eta_{\|}$ parameter in Fig. 4.2 are calculated by extracting the values by modulating the ECCD clusters with different power variations. The simplified model used to represent the ECCD current and power distributions permits the optimization problem (4.39) to be solved as a linear least squares problem. This optimization technique is relatively simple and can be implemented with a fast execution time. The extracted feedforward stationary values $\overline{P}_{ec1}$, $\overline{P}_{ec2}$ and $\overline{I}_p$ of the inputs that correspond to the desired reference profiles are extracted using RAPTOR and added to the feedback control. The control scheme used in this chapter is presented as a block diagram in Fig. 4.5.

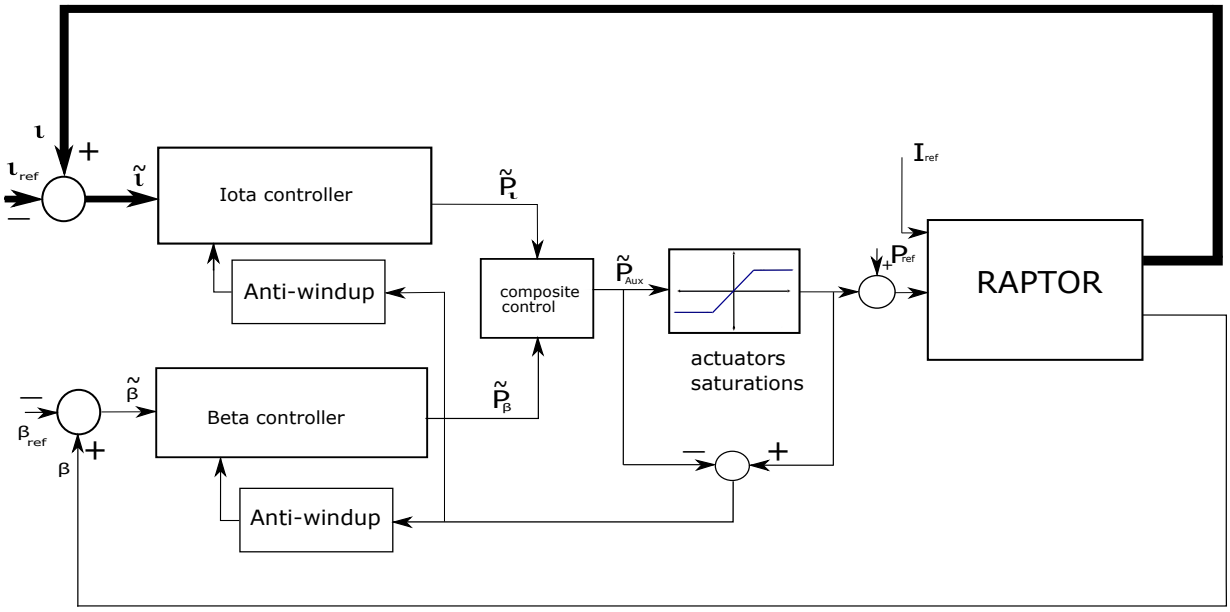


Figure 4.5: Control scheme

The polynomial functions $p_z(x),\ p_I(x),\ k_z(x)$ and $k_I(x)$, are presented in Fig. 4.6. They are calculated by solving the optimization problem in subsection 4.2.2 using parameters typical for the TCV configuration and using $\lambda = \gamma_2 = 0.01$ and $\gamma_1 = 5$. The control gain parameters can be additionally tuned in order to set the robustness and performance of the closed-loop behavior according to the performance requirements.
The PI feedback control of the β parameter is calculated using fixed values for the global energy confinement time $\tau_{th} = 4.4\ ms$ and the effective time delay is chosen to be $\theta \approx 5\ ms$. The optimal value of the free parameter was fixed to $\tau_c = 0.1$ after tuning, using simulation testing and choosing the best tracking performance. Moreover, the value of this parameter

can be changed according to the control requirements. For a robust performance of the tracking, this parameter should be $\tau_c \geq \theta$. If this parameter is decreased the convergence speed and the disturbance rejection are improved. For better stability, robustness and small input usage the value of this parameter should be increased.

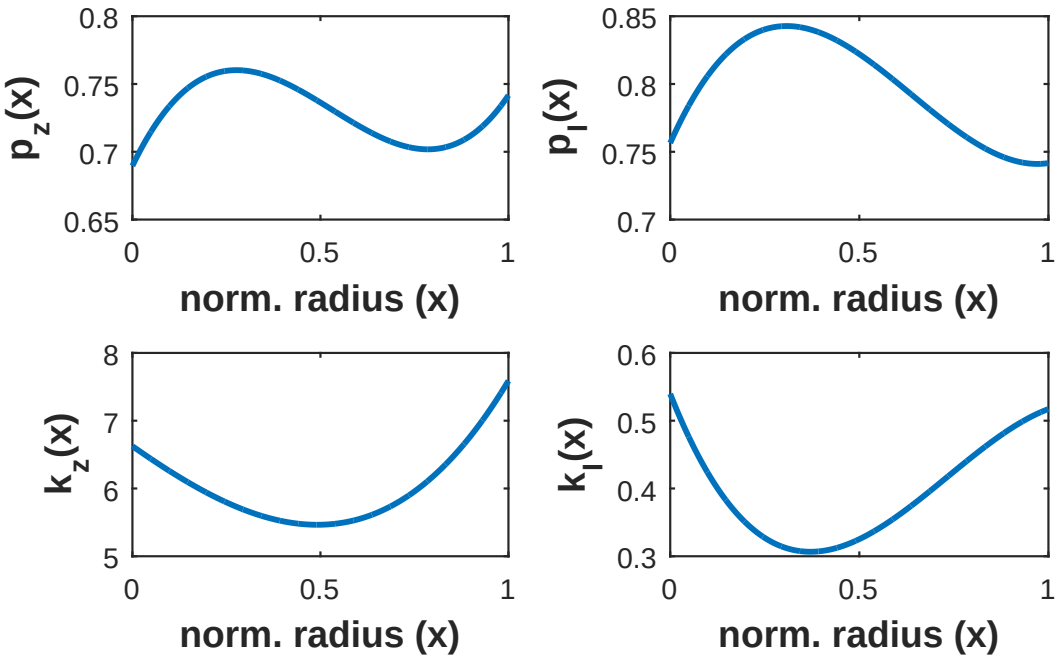


Figure 4.6: Plot of the numerical solutions of the optimization problem presented in subsection 4.2.2 as polynomial functions $p_z(x), p_I(x), k_z(x)$ and $k_I(x)$ using an LMI solver.

In Fig. 4.7, the ι profile of the closed-loop system is presented. The feedback control is activated at $t = 0.1\ s$ and the forgetting factor $\lambda(t)$ is added to the integral action. The tracking of ι is compared with the case in which only pure integration is applied. The forgetting factor is set to have a high value only when the control is activated and when the reference profiles are changed. In these transition intervals, the plasma profiles are far from the reference point and the integral action can accumulate significant amount of error that leads to overshoot in the closed-loop tracking. From this figure, it can be concluded that the forgetting factor is useful for the reduction of these overshoots.

The controller performance is tested considering several scenarios:

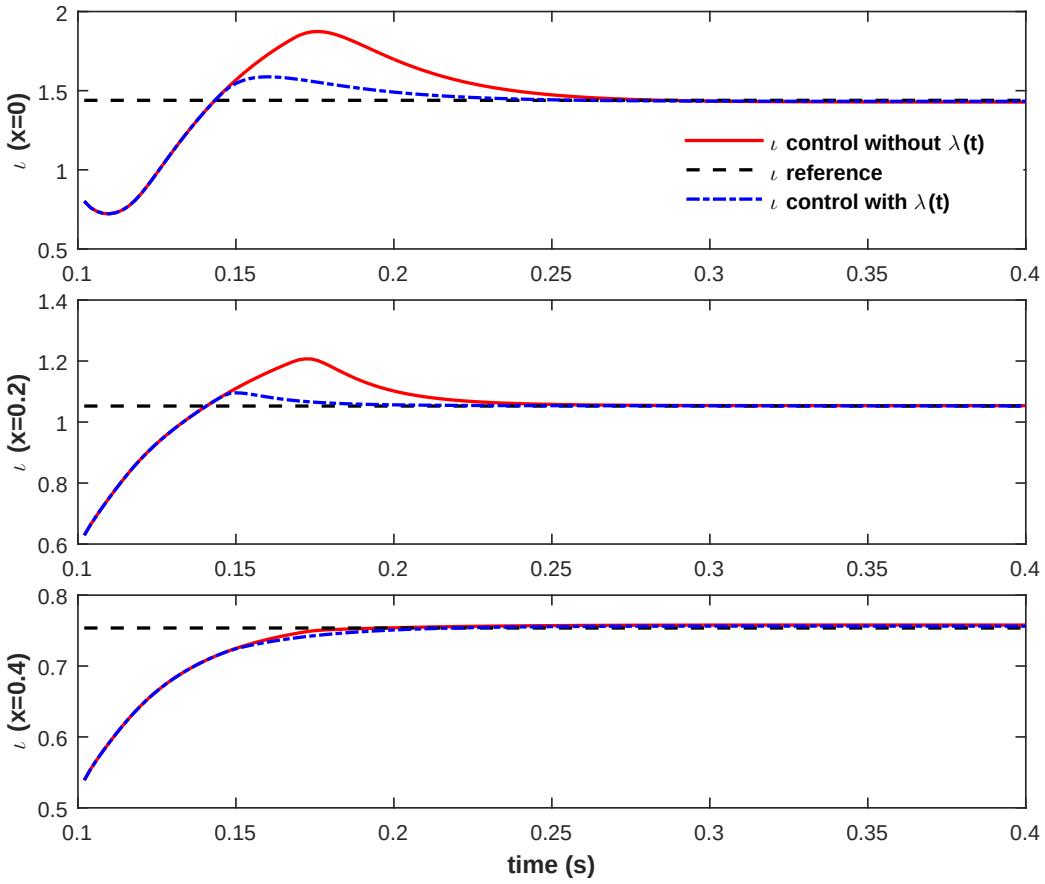


Figure 4.7: Response of ι with a pure integrator (red line) compared with the response when a forgetting factor $\lambda(t)$ is added to the integral action (blue dashed line) at several discretized locations.

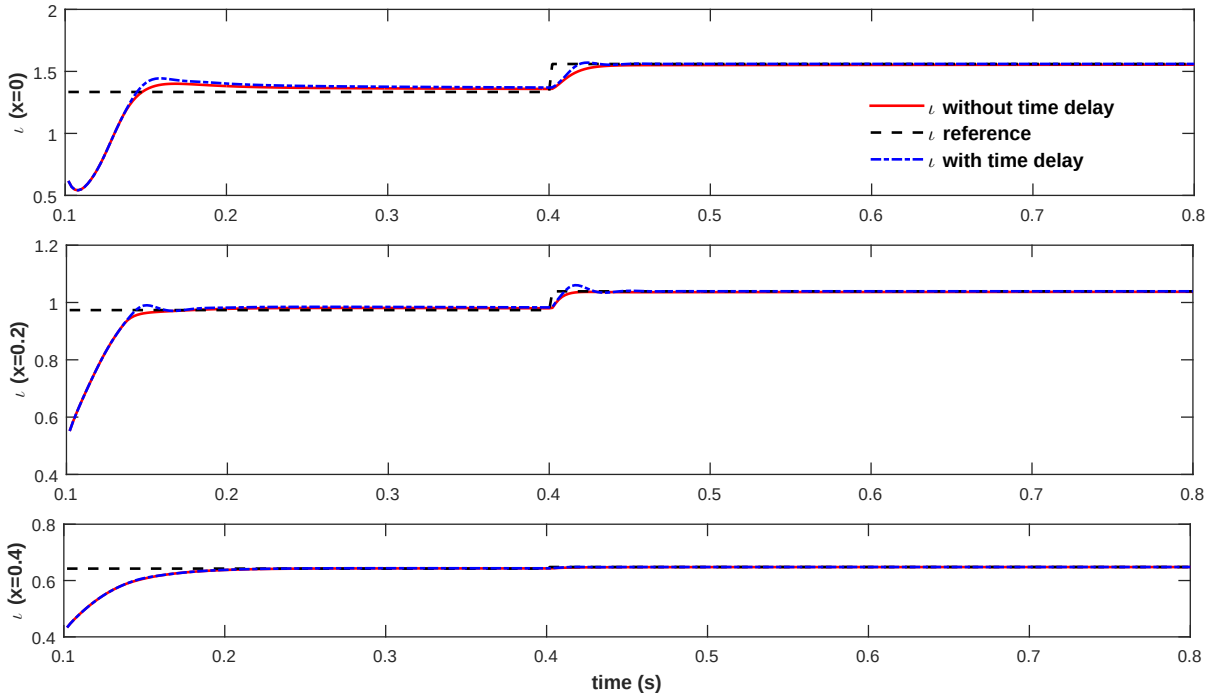
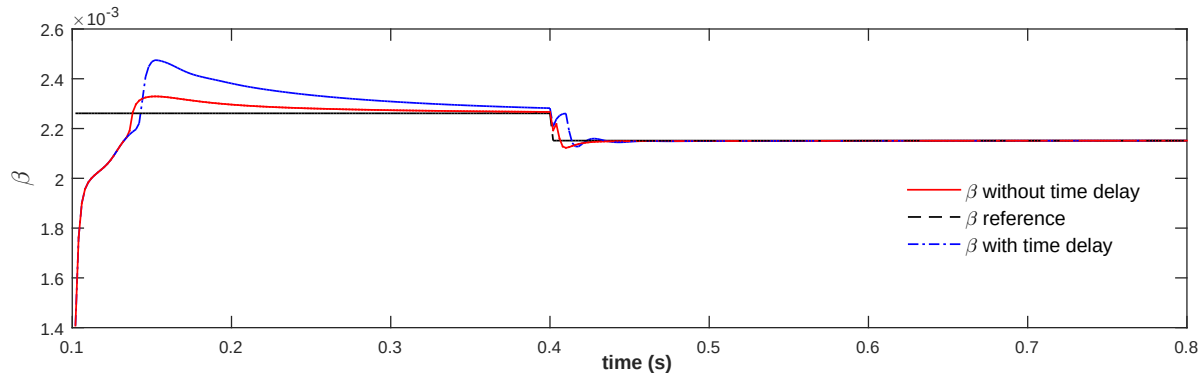


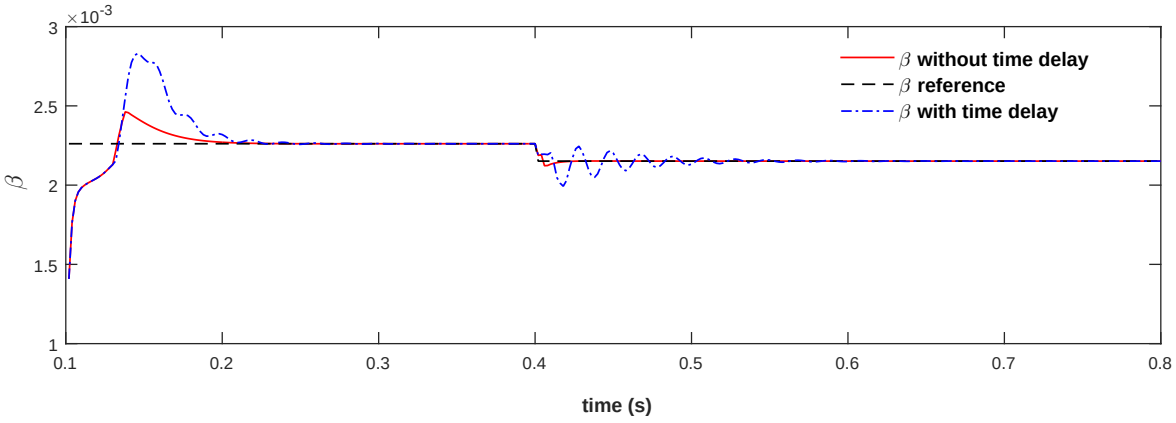
Figure 4.8: ι tracking evolution is presence of a time delay in the feedback loop.

4.6.1 Presence of time delays

Transportation of the control signals and their transition in the control systems can generate delays. Sometimes the effect of these delays cannot be neglected. For this reason, the performance of the control algorithm should be tested and adapted to these delays, which can be present when the control is applied in the real TCV control system. The control performance is tested by adding a 6 ms time delay in the control action based on the possible time delays in the control action. In Fig. 4.8 the results for the slow component ι are presented. In this figure it can be seen that the time delays of small scales do not affect significantly the control of this component. Larger time delays, of 100 ms and higher, can affect the performance of this parameter. In the case of a larger time delay some extra tuning of the control parameters should be considered as discussed in (Bribiesca Argomedo et al., 2013b). The time delays in the system are affecting more the performance of the fast varying β parameter. In Fig. 4.9a and Fig. 4.9b the results of control are presented for β with $\tau_c = 0.1$ and $\tau_c = 0.01$, respectively. In Fig. 4.9a using an increased value $\tau_c = 0.1$ the robustness is increased and the speed of response is decreased. In this case the high overshoots and osculations are effectively attenuated even when a time delay of 6 ms is present. In the case when $\tau_c = 0.01$ is used the speed of the convergence is improved. On the other hand, when the time delay is introduced there are higher overshoots and osculations in the closed loop tracking.



(a) β tracking with $\tau_c = 0.1$.



(b) β tracking with $\tau_c = 0.01$.

Figure 4.9: β tracking evolution with a time delay in the feedback loop.

4.6.2 Change of the deposition location and width for P_{ec2}

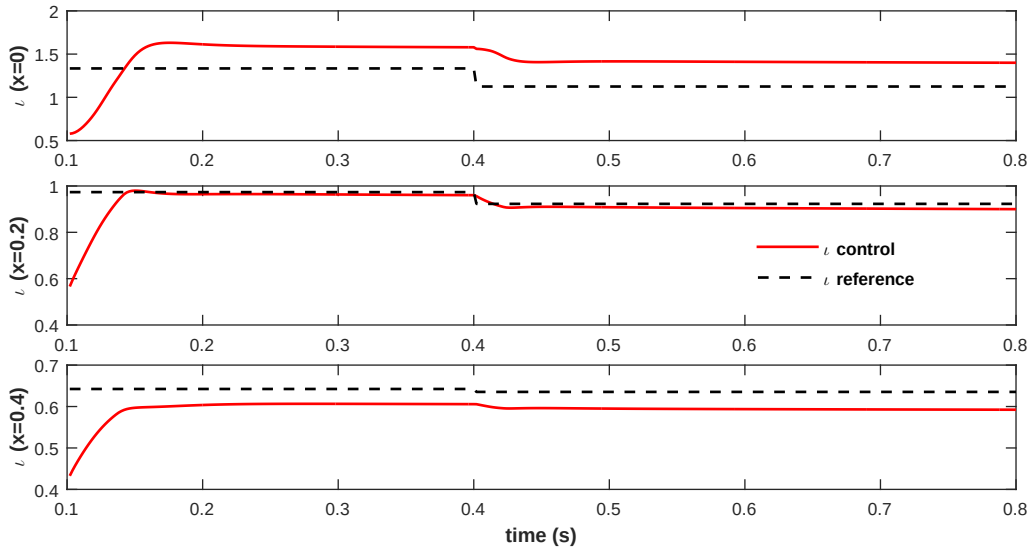


Figure 4.10: ι tracking with changed deposition location and width for P_{ec2}.

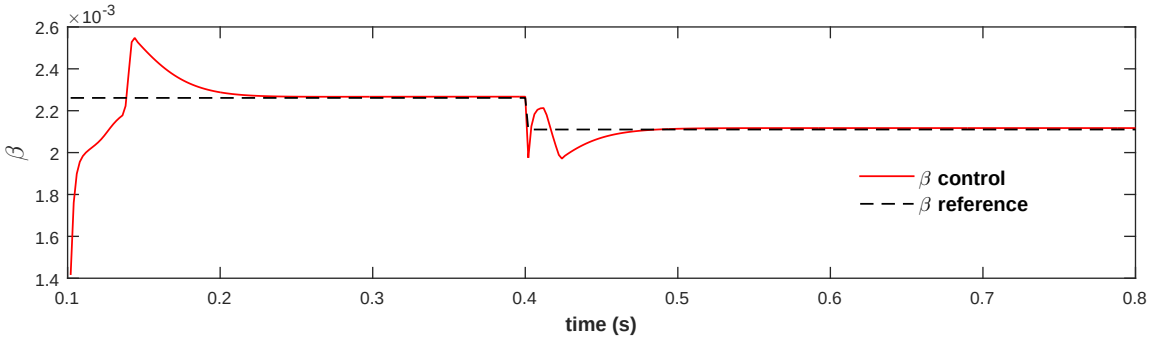


Figure 4.11: β tracking with changed deposition location and width for P_{ec2}.

The control performance is tested in a scenario where the deposition location and width are changed in one of the clusters. The deposition in the second ECCD cluster is changed in these simulations, such that the width is $\omega_{dep} = 0.44$ and the location of the peak of the deposition is $x_{dep} = 0.2$. After the configuration of the cluster is changed, the desirable reference profile may be not reachable using the new configuration of the clusters. Using RAPTOR as an observer, the current deposition that results from the configuration of the clusters in the real experiments can be directly monitored. This can be updated online in the controller while the experiments are running and adopt the control algorithm to the changes of the system configuration. The simulation results for the tracking of ι profile and β are presented in Fig. 4.10 and Fig. 4.11, respectively. The control is activated at

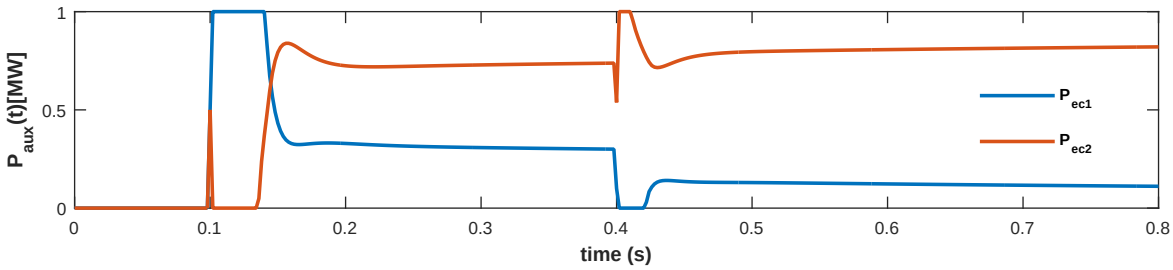
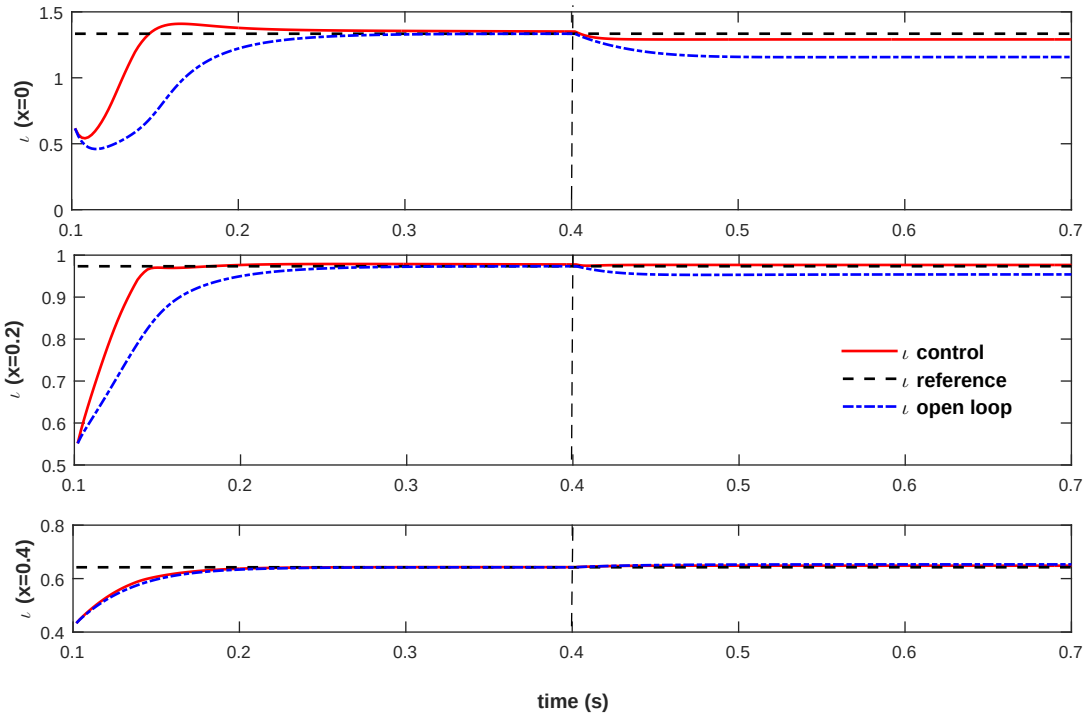


Figure 4.12: Applied ECCD power evolution with changed deposition location and width for P_{ec2}.

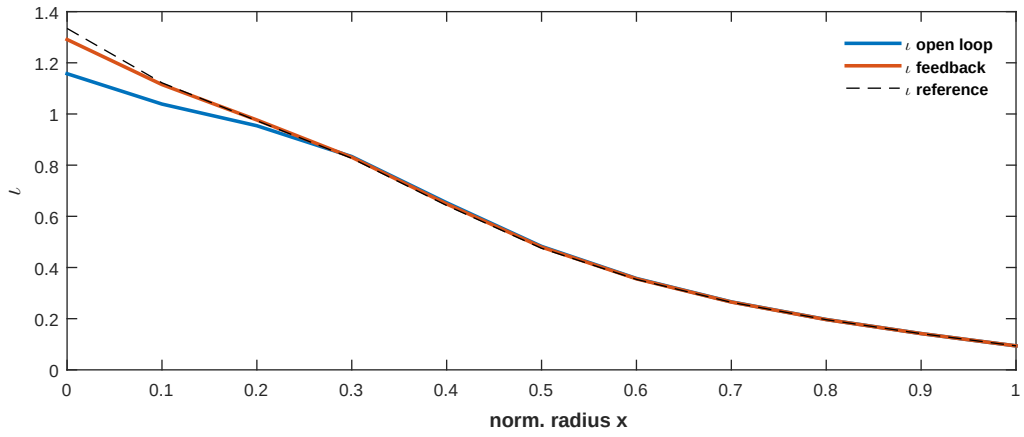
0.1 s and there is a change in the reference at 0.4 s. The target profiles extracted with the initial system configuration are not reachable when the parameters of the cluster are changed. This causes some offset between the achieved profile and the target ι profile. The values of the auxiliary powers used as control inputs are presented in Fig. 4.12.

4.6.3 Disturbance attenuation

The sensitivity of the control algorithm to disturbances and their rejection is one of the most important features that should be tested before the controller is applied. In a complex system like the tokamak, where the model of the system depends on numerous parameters, there exists many sources of disturbances. To test the disturbance attenuation of the controller, an additional ECCD antenna was added to the simulations and acts a source of external disturbances. This additional antenna was added with a deposition width $\omega_{dep} = 0.44$ and with location of the peak of the deposition at $x_{dep} = 0.2$. The control of the system was activated at $t = 0.1$ s and this antenna was activated at $t = 0.4$ s with a power of 450 kW. In Fig. 4.13a the time evolution of the ι tracking control is presented and in Fig. 4.13b is presented the ι profile at 0.7 s. In Fig. 4.14 the results of the tracking of the β component are presented. In these figures the feedback tracking of the system is compared with the open-loop output of the system. It is clear that the feedback control is reducing the offset error between the reference profiles and the plasma quantities. High gains were used for the controller parameters in this case, which led to a faster convergence to the reference point. This leads to a more "aggressive" control action with a large control signal that can be observed in Fig. 4.15.



(a) ι profile tracking evolution.



(b) ι profile tracking at $t = 0.7\ s$.

Figure 4.13: ι profile evolution with external disturbance added with $\omega_{dep} = 0.4$ and $x_{dep} = 0.2$.

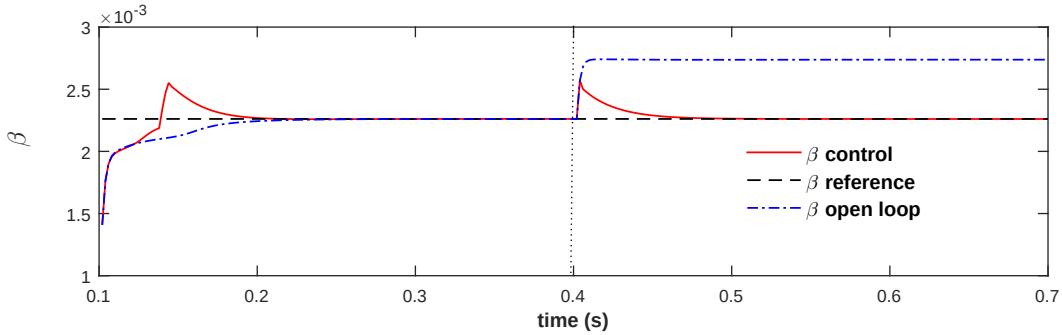


Figure 4.14: β evolution with added external disturbance at $t = 0.4\ s$.

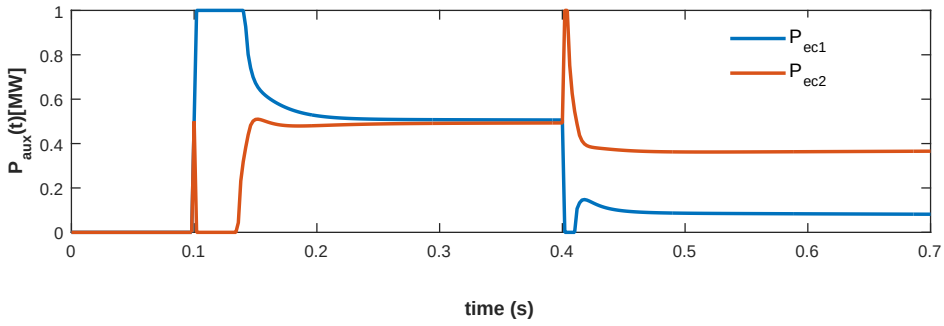


Figure 4.15: Applied ECCD power evolution with added external disturbance at $t = 0.4\ s$.

4.7 Conclusion on the chapter

In this chapter a control strategy for the simultaneous control of the safety factor and the plasma β parameter is presented. The control strategy in this chapter is adapted to simplified control oriented equations that are based on the TCV experiment configuration. The control system in this chapter was represented by coupled PDE and ODE equations. The control was performed using first-principles driven models where some of the parameters were simplified and uncertain. The control design was calculated separately for the two quantities taking into advantage the difference in the time scales. To solve the tracking problem, we used a combination of proportional and integral components for the control of the both parameters. Adding an integral action enables the controllers to eliminate offset from the target profile and the proportional term speeds up the convergence to the reference profiles. The control was calculated such that the exponential stability of the closed-loop system is guaranteed. To prepare the implementation of the control strategy on the real TCV facility, the simulation tests were performed using RAPTOR simulator and the performance and robustness of the controller were tested considering several scenarios. Time delay in the control action was considered and the control performance was tested for this case. The robustness of the controller was tested using different system configurations and control scenarios. Once the simulation results are successful, the controller implemented in RAPTOR and can be built easily and tested in real TCV experiments.

Conclusion and Perspectives

In this thesis, the simultaneous control of several plasma quantities in a tokamak plasma has been presented. The main goal was to investigate the internal couplings using identification methods and to develop control methods using using an infinite-dimensional approach that can deal with the complex coupling between the magnetic and the kinetic parameters. The main plasma parameters that were the focus of this thesis were the safety factor, electron temperature and the plasma β. The goal of these control strategies is to guarantee stability and confinement, which are crucial for the performance of the plasma.

Several aspects, that are important for successful control strategies for advanced plasma scenarios were elaborated. The first part of this thesis was dedicated to suitable control models that are crucial for successful feedback control strategies. Two kinds of control models were obtained in the second chapter. The first kind is the first-principle model that is obtained using directly the plasma evolution equations. In contrast to previous works that develop control oriented models for the same problem, in this thesis, the model was linearized and presented in a form that can be used to develop a control strategy based on PDE control theory. The second kind of model that was presented in this chapter is the data-driven model obtained by using system identification methods. The model identification techniques that were used to calculate the model are developed for state-space models. The technique used in this chapter was a combination of the MOESP subspace identification method and the output-error method. The identification and the validation data were extracted using the METIS simulator configured with the parameters of the DIII-D tokamak.

The second part of the thesis was dedicated to the development of control algorithms for coupled plasma parameters using infinite dimensional control theory. In the third chapter, the control problem of coupled plasma safety factor and electron temperature was synthesized using infinite dimensional control theory. Infinite dimensional control techniques were used to control simultaneously several plasma parameter for the first time in this thesis. First, the stability and the convergence rate of the system was examined using a candidate Lyapunov function. The Lyapunov functions were found by transforming the problem as an LMI inequality and presenting the weighting functions as Legendre polynomials. Lyapunov control technique was proposed and successfully implemented for the control of the coupled system. The algorithm was modified and extended to deal with the two different time scales in the system. Later on, the system was decoupled using singular perturbation theory and composite control was applied to the system. This approach was shown to be beneficial when applied to large scale tokamaks, where the timescale differences between the kinetic and the magnetic parameters is large. This control strategy was applied to ITER simulations.

In the last chapter, control algorithms for simultaneous control of the safety factor and the plasma β were presented, motivated by a scheduled campaign of TCV experiments. The system to be controlled in this chapter is given by two coupled PDE and ODE equations. The control signals are computed separately for each parameter as a result of the two time scales difference. Simplified control models were used, that are easy and practical to be implemented in the real TCV experiments. The feedback control was designed by considering proportional-integral feedback for both components. Adding an integral anti-windup component was crucial to improve the performance and to eliminate the controller windup that appears due to the limitations of the actuators. The robustness and the performance of the algorithms presented in this chapter were successfully tested using RAPTOR before they are applied in real TCV control experiments.

There are many remaining challenges that may be considered in future works dedicated to the infinite dimensional control approaches in advanced plasma scenarios. Some of these challenges are:

- A boundary control algorithm that includes the boundary input I_P controlled directly by V_{loop} could eventually improve the performance of the system. For a boundary control of a parabolic PDEs there are already developed techniques. One known technique for boundary control is the backstepping designs for PDEs (Krstic and Smyshlyaev, 2008). Another method is the optimal boundary control of parabolic PDEs via weak variations presented in (Moura and Fathy, 2013). The complexity of the parabolic equation used in this thesis that comes from the cylindrical representation and the space varying coefficients makes direct application of these methods difficult. The adaptation of some of these methods for this particular system can be challenging for some future works.

- There are many other plasma parameters that are important for the advanced tokamak scenarios control. For example, the ion temperature, toroidal velocity, and plasma density are other plasma varying quantities that are also very important for the plasma performance and stability. In future works the control models could be extended to consider these quantities as additional controlled outputs.

- Linearized models around an equilibrium point were used in this thesis. These equilibrium points can be easily extracted using a plasma simulator. The equilibrium point can be extracted if the plasma simulator is executed for sufficiently long time. However, this is not the case when real a tokamak machine is used. In real tokamak experiment the calculation of equilibrium points using online numerical methods to solve the static plasma equations should be considered, for example as the one used in (Vu et al., 2016).

- The feedback control can be used in a combination with some optimally computed feed-forward control signals. This can significantly improve the plasma performance (Barton et al., 2015a; Felici and Sauter, 2012). The feed-forward commands can be computed off-line to find the optimal trajectory. The computation of the feed-forward inputs can be done by substantial number of trial-and-error attempts and based on experience gained during operation of a particular device. Another way is to use some model based techniques as for example extremum-seeking open-loop optimal control presented in (Ou et al., 2008).

- In this thesis only linear models were used to calculate the control algorithm. Because of the high nonlinear nature of the original model, some nonlinear control strategies may give some improved performances. Developing a control based on nonlinear PDEs is a huge challenge for this kind of PDEs because of their high complexity.

- The control simulations were performed by using only the RAPTOR simulator with the configuration based on TCV and ITER experimental setup. In future works the application of the proposed algorithms should be extended to other tokamak machines with different experimental settings. The control model should be extended to include the models of the other external heating and current drive sources.

Bibliography

Artaud, JF et al. (2005). "Predictive integrated modelling for ITER scenarios." In: *32nd EPS Conference on Plasma Physics*. Vol. 29 (cit. on p. 27).

Artaud, JF et al. (2010). "The CRONOS suite of codes for integrated tokamak modelling." In: *Nuclear Fusion* 50.4, p. 043001 (cit. on pp. 6, 18, 40).

Åström, Karl Johan and Tore Hägglund (2006). *Advanced PID control*. ISA-The Instrumentation, Systems and Automation Society (cit. on p. 96).

Barton, JE et al. (2015a). "Physics-model-based nonlinear actuator trajectory optimization and safety factor profile feedback control for advanced scenario development in DIII-D." In: *Nuclear Fusion* 55.9, p. 093005 (cit. on pp. 6, 10, 18, 88, 113).

Barton, Justin E et al. (2013). "Robust control of the safety factor profile and stored energy evolutions in high performance burning plasma scenarios in the ITER tokamak." In: *52nd Conference on Decision and Control*. IEEE. Florence, Italy, pp. 4194–4199 (cit. on pp. 10, 88).

— (2015b). "Physics-based control-oriented modeling and robust feedback control of the plasma safety factor profile and stored energy dynamics in ITER." In: *Plasma Physics and Controlled Fusion* 57.11, p. 115003 (cit. on pp. 6, 10, 18, 88).

Barton, Justin E et al. (2015c). "Simultaneous closed-loop control of the current profile and the electron temperature profile in the TCV tokamak." In: *American Control Conference, Chicago, USA*, pp. 3316–3321 (cit. on pp. 6, 9, 18, 62).

Basiuk, V et al. (2003). "Simulations of steady-state scenarios for Tore Supra using the CRONOS code." In: *Nuclear Fusion* 43.9, p. 822 (cit. on pp. 6, 18).

Bauer, Dietmar (2000). "On data preprocessing for subspace methods." In: *39th IEEE Conference on Decision and Control*. Vol. 3. Sydney, Australia, pp. 2403–2408 (cit. on p. 44).

Blum, Jacques (1989). *Numerical Simulation and Optimal Control in Plasma Physics: With Applications to Tokamaks (Wiley Gauthier-Villars Series in Modern Applied Mathemat)* (cit. on pp. 23, 24).

Bohn, C and DP Atherton (1995). "An analysis package comparing PID anti-windup strategies." In: *IEEE Control Systems* 15.2, pp. 34–40 (cit. on pp. 11, 88).

Bondarenko, Boris Dmitrievich (2001). "Role played by OA Lavrent'ev in the formulation of the problem and the initiation of research into controlled nuclear fusion in the USSR." In: *Physics-Uspekhi* 44.8, pp. 844–851 (cit. on p. 14).

Boyer, Mark D et al. (2013). "First-principles-driven model-based current profile control for the DIII-D tokamak via LQI optimal control." In: *Plasma Physics and Controlled Fusion* 55.10, p. 105007 (cit. on pp. 5, 17).

Boyer, Mark D et al. (2014). "Backstepping control of the toroidal plasma current profile in the DIII-D tokamak." In: *IEEE Transactions on Control Systems Technology* 22.5, pp. 1725–1739 (cit. on pp. 5, 17).

Bribiesca Argomedo, F et al. (2010). "Model-based control of the magnetic flux profile in a tokamak plasma." In: *Decision and Control (CDC), 2010 49th IEEE Conference on*. IEEE, pp. 6926–6931 (cit. on p. 92).

Bribiesca Argomedo, F et al. (2013a). "A Strict Control Lyapunov Function for a Diffusion Equation With Time-Varying Distributed Coefficients." In: *IEEE Transactions on Automatic Control* 58.2, pp. 290–303 (cit. on pp. 5, 8, 17, 62, 74).

Bribiesca Argomedo, Federico et al. (2013b). "Lyapunov-based distributed control of the safety factor profile in a tokamak plasma." In: *Nuclear Fusion* 53, p. 033005 (cit. on p. 104).

Chilali, Mahmoud and Pascal Gahinet (1996). "H∞ design with pole placement constraints: an LMI approach." In: *IEEE Transactions on Automatic Control* 41.3, pp. 358–367 (cit. on p. 48).

Di Ruscio, David (1997). "Subspace System Identification: Theory and applications." In: *Lecture notes, Telemark University College, Porsgrunn, Norway* (cit. on pp. 8, 37, 45).

Duchesne, Laurent et al. (1996). "Subspace identification with multiple data sets." In: *Proceedings of the 1996 AIAA Guidance, Navigation, and Control Conference*. San Diego (CA), USA (cit. on p. 44).

Erba, M et al. (1998). "Validation of a new mixed Bohm/gyro-Bohm model for electron and ion heat transport against the ITER, Tore Supra and START database discharges." In: *Nuclear Fusion* 38.7, p. 1013 (cit. on p. 27).

Felici, F., M. de Baar, and M. Steinbuch (2014). "A dynamic state observer for real-time reconstruction of the tokamak plasma profile state and disturbances." In: *American Control Conference*. Portland,USA, pp. 4816–4823 (cit. on p. 84).

Felici, F and O Sauter (2012). "Non-linear model-based optimization of actuator trajectories for tokamak plasma profile control." In: *Plasma Physics and Controlled Fusion* 54.2, p. 025002 (cit. on pp. 6, 9, 18, 27, 62, 113).

Felici, F et al. (2011). "Real-time physics-model-based simulation of the current density profile in tokamak plasmas." In: *Nuclear Fusion* 51.8, p. 083052 (cit. on pp. 6, 18, 25, 30, 74).

Felici, Federico (2011). "Real-time control of tokamak plasmas: from control of physics to physics-based control." In: (cit. on pp. 5, 17, 18).

Gahlawat, Aditya et al. (2012). "Bootstrap current optimization in tokamaks using sum-of-squares polynomials." In: *51st Annual Conference on Decision and Control*. IEEE, pp. 4359–4365 (cit. on pp. 5, 9, 17, 62).

Gajic, Zoran (2001). *Optimal control of singularly perturbed linear systems and applications*. CRC Press (cit. on pp. 9, 62).

Gaye, Oumar et al. (2013a). "H∞ stabilization of the current profile in tokamak plasmas via an LMI approach." In: *Automatica* 49.9, pp. 2795–2804 (cit. on pp. 5, 9, 11, 17, 62, 88, 100).

Gaye, Oumar et al. (2013b). "Robust stabilization of the current profile in tokamak plasmas using sliding mode approach in infinite dimension." In: *Control Engineering Practice* 21.10, pp. 1350–1358 (cit. on pp. 5, 17).

Geelen, P et al. (2015). "Parameter estimation for a nonlinear control-oriented tokamak profile evolution model." In: *Plasma Physics and Controlled Fusion* 57.12, p. 125008 (cit. on pp. 5, 17).

Gormezano, C et al. (2007). "Steady state operation." In: *Nuclear Fusion* 47.6, S285 (cit. on pp. 3, 15).

Grimholt, Chriss and Sigurd Skogestad (2012). "Optimal PI-control and verification of the SIMC tuning rule." In: *IFAC Proceedings Volumes* 45.3, pp. 11–22 (cit. on p. 97).

Hall, CE, AS Hodel, and JY Hung (1999). "Variable structure PID control to prevent integrator windup." In: (cit. on p. 98).

Hanus, Raymond, Michel Kinnaert, and J-L Henrotte (1987). "Conditioning technique, a general anti-windup and bumpless transfer method." In: *Automatica* 23.6, pp. 729–739 (cit. on p. 98).

Haverkamp, Bert (2000). "Subspace method identification, theory and practice." PhD thesis. Ph. D. thesis, TU Delft, Delft, The Netherlands (cit. on p. 41).

Hawryluk, RJ (1980). "An empirical approach to tokamak transport." In: *Physics of plasmas close to thermonuclear conditions* 1, pp. 19–46 (cit. on pp. 6, 18).

Hinton, FL and RD Hazeltine (1976). "Theory of plasma transport in toroidal confinement systems." In: *Reviews of Modern Physics* 48.2, p. 239 (cit. on pp. 25, 26).

Hirshman, SP, RJ Hawryluk, and B Birge (1977). "Neoclassical conductivity of a tokamak plasma." In: *Nuclear Fusion* 17.3, p. 611 (cit. on p. 24).

Kaplan, Wilfred (2002). *Advanced calculus*. Addison Wesley (cit. on p. 67).

Katayama, Tohru (2006). *Subspace methods for system identification*. Springer Science & Business Media (cit. on pp. 8, 37, 46, 48).

Khalil, Hassan K and JW Grizzle (1996). *Nonlinear systems*. Vol. 3. Prentice hall New Jersey (cit. on pp. 9, 62).

Kim, D et al. (2016). "Simple predictive electron transport models applied to sawtoothing plasmas." In: *Plasma Physics and Controlled Fusion* 58.5, p. 055002 (cit. on pp. 5, 17, 27).

Kim, SH and JB Lister (2012). "A potentially robust plasma profile control approach for ITER using real-time estimation of linearized profile response models." In: *Nuclear Fusion* 52.7, p. 074002 (cit. on pp. 5, 6, 9, 17, 18, 62).

Kokotovic, Petar, Hassan K Khalil, and John O'reilly (1999). *Singular perturbation methods in control: analysis and design*. Vol. 25. Siam (cit. on pp. 9, 62).

Kokotovic, PK and RA Freeman (1996). *Robust nonlinear control design* (cit. on pp. 8, 61).

Krstic, Miroslav and Andrey Smyshlyaev (2008). *Boundary control of PDEs: A course on backstepping designs*. Vol. 16. Siam (cit. on p. 112).

Laborde, L et al. (2004). "A model-based technique for integrated real-time profile control in the JET tokamak." In: *Plasma Physics and Controlled Fusion* 47.1, p. 155 (cit. on pp. 4, 16).

— (2005). "A model-based technique for integrated real-time profile control in the JET tokamak." In: *Plasma Physics and Controlled Fusion* 47.1, p. 155 (cit. on pp. 5, 17).

Lawson, John D (1957). "Some criteria for a power producing thermonuclear reactor." In: *Proceedings of the Physical Society. Section B* 70.1, p. 6 (cit. on pp. 2, 13).

Leith, DJ, DJ Murray-Smith, and R Bradley (1993). "Combination of data sets for system identification." In: *IEE Proceedings D-Control Theory and Applications*. Vol. 140. 1. IET, pp. 11–18 (cit. on p. 50).

Ljung, Lennart (1998). *System identification*. Springer (cit. on pp. 8, 37, 43, 50).

Löfberg, Johan (2004). "YALMIP: A toolbox for modeling and optimization in MATLAB." In: *IEEE International Symposium on Computer Aided Control Systems Design*. Taipei, Taiwan, pp. 284–289 (cit. on pp. 48, 67).

Maljaars, Bert et al. (2015). "Model Predictive Control of the Current Density Distribution and Stored Energy in Tokamak Fusion Experiments using Trajectory Linearizations." In: *IFAC-PapersOnLine* 48.23, pp. 314–321 (cit. on p. 18).

Mazon, D et al. (2003). "Active control of the current density profile in JET." In: *Plasma physics and controlled fusion* 45.7, p. L47 (cit. on pp. 4, 16).

Miller, Daniel N and Raymond A De Callafon (2013). "Subspace identification with eigenvalue constraints." In: *Automatica* 49.8, pp. 2468–2473 (cit. on pp. 47, 48).

Moreau, D et al. (2003). "Real-time control of the q-profile in JET for steady state advanced tokamak operation." In: *Nuclear fusion* 43.9, p. 870 (cit. on pp. 4, 16).

Moreau, D et al. (2008). "A two-time-scale dynamic-model approach for magnetic and kinetic profile control in advanced tokamak scenarios on JET." In: *Nuclear Fusion* 48.10, p. 106001 (cit. on pp. 4, 16, 37, 39, 41, 51, 56, 57, 68).

Moreau, D et al. (2011). "Plasma models for real-time control of advanced tokamak scenarios." In: *Nuclear Fusion* 51.6, p. 063009 (cit. on pp. 4, 16, 37, 39, 50, 56, 57).

Moreau, D et al. (2013). "Integrated magnetic and kinetic control of advanced tokamak plasmas on DIII-D based on data-driven models." In: *Nuclear Fusion* 53.6, p. 063020 (cit. on pp. 4, 10, 16, 50, 52, 56, 88).

Moura, Scott J and Hosam K Fathy (2013). "Optimal Boundary Control of Reaction–Diffusion Partial Differential Equations via Weak Variations." In: *Journal of Dynamic Systems, Measurement, and Control* 135.3, p. 034501 (cit. on p. 112).

Ou, Y et al. (2008). "Design and simulation of extremum-seeking open-loop optimal control of current profile in the DIII-D tokamak." In: *Plasma Physics and Controlled Fusion* 50.11, p. 115001 (cit. on p. 113).

Peeters, AG (2000). "The bootstrap current and its consequences." In: *Plasma Physics and Controlled Fusion* 42.12B, B231 (cit. on p. 24).

Pereverzev, GV and PN Yushmanov (2002). *ASTRA Automated system for transport analysis in a Tokamak Report IPP 5/98, Max-Planck-Institut für Plasmaphysik, Garching* (cit. on pp. 6, 18).

Polevoi, AR, S Medvedev, Pustovitov YU, et al. (2002). "Possibility of Q$>$ 5 stable, steady-state operation in ITER with moderate βN and H-factor." In: *Fusion Energy* (cit. on p. 27).

Ramos, JI (1987). "Hermitian operator methods for reaction-diffusion equations." In: *Numerical Methods for Partial Differential Equations* 3.4, pp. 241–287 (cit. on p. 47).

Sauter, Olivier, Clemente Angioni, and YR Lin-Liu (1999). "Neoclassical conductivity and bootstrap current formulas for general axisymmetric equilibria and arbitrary collisionality regime." In: *Physics of Plasmas (1994-present)* 6.7, pp. 2834–2839 (cit. on p. 24).

Sautera, O, C Angioni, and YR Lin-Liub (1999). "Erratum:"Neoclassical conductivity and bootstrap current formulas for general axisymmetric equilibria and arbitrary collisionality regime"† Phys. Plasmas 6, 2834 „1999…" In: *Phys. Plasmas* 6, p. 2834 (cit. on p. 24).

Skogestad, Sigurd (2001). "Probably the best simple PID tuning rules in the world." In: *AIChE Annual Meeting, Reno, Nevada*. Citeseer (cit. on p. 96).

Spitzer, Lyman (2013). *Physics of fully ionized gases*. Courier Corporation (cit. on p. 24).

Suleiman, Wael and André Monin (2007). "Linear multivariable system identification: multi-experiments case." In: *Conference on Systems and Control*. Marrakech, Morocco (cit. on pp. 41, 44, 45).

Tang, Ying, Christophe Prieur, and Antoine Girard (2014). "Boundary control synthesis for hyperbolic systems: a singular perturbation approach." In: *53rd IEEE Conference on Decision and Control*. IEEE, pp. 2840–2845 (cit. on pp. 9, 62).

Tarbouriech, Sophie et al. (2011). *Stability and stabilization of linear systems with saturating actuators*. Springer Science & Business Media (cit. on pp. 11, 88).

Taroni, A et al. (1994). "Global and local energy confinement properties of simple transport coefficients of the Bohm type." In: *Plasma physics and controlled fusion* 36.10, p. 1629 (cit. on p. 27).

Taylor, TS (1997). "Physics of advanced tokamaks." In: *Plasma Physics and Controlled Fusion* 39.12B, B47 (cit. on pp. 3, 15).

Troyon, F et al. (1984). "MHD-limits to plasma confinement." In: *Plasma physics and controlled fusion* 26.1A, p. 209 (cit. on p. 28).

Vazquez, Rafael and Miroslav Krstic (2008). *Control of turbulent and magnetohydrodynamic channel flows: boundary stabilization and state estimation*. Springer Science & Business Media (cit. on pp. 9, 62).

Verhaegen, Michel and Patrick Dewilde (1992). "Subspace model identification part 1. The output-error state-space model identification class of algorithms." In: *International Journal of Control* 56.5, pp. 1187–1210 (cit. on pp. 8, 37, 41).

Verhaegen, Michel and Vincent Verdult (2007). *Filtering and system identification: a least squares approach*. Cambridge university press (cit. on pp. 41, 49).

Visioli, Antonio (2003). "Modified anti-windup scheme for PID controllers." In: *IEE Proceedings-Control Theory and Applications* 150.1, pp. 49–54 (cit. on p. 97).

Vu, Ngoc Minh Trang et al. (2016). "Plasma q-profile control in tokamaks using a damping assignment passivity-based approach." In: *Control Engineering Practice* 54, pp. 34–45 (cit. on pp. 5, 17, 112).

Wesson, John and DJ Campbell (2011). *Tokamaks*. Vol. 149. Oxford University Press (cit. on pp. 1, 2, 13, 14, 26, 28).

Witrant, Emmanuel and Sylvain Brémond (2011). "Shape identification for distributed parameter systems and temperature profiles in tokamaks." In: *50th IEEE Conference on Decision and Control and European Control Conference*. Orlando (FL),USA, pp. 2626–2631 (cit. on p. 29).

Witrant, Emmanuel et al. (2007). "A control-oriented model of the current profile in tokamak plasma." In: *Plasma Physics and Controlled Fusion* 49.7, p. 1075 (cit. on pp. 5, 17, 24).

Ziegler, John G and Nathaniel B Nichols (1942). "Optimum settings for automatic controllers." In: *trans. ASME* 64.11 (cit. on p. 96).

Résumé — L'objectif de cette thèse est le développement de nouvelles méthodes d'analyse et de commande pour une classe d'équations aux dérivées partielles couplées permettant de modéliser le transport combiné du flux magnétique et de la pression (produit de la densité et de la température) dans les plasmas tokamak. Le système couplé est représenté par deux équations 1D de diffusion résistive. Dans cette thèse, on a obtenu deux types de modèles: le premier repose sur des principes physiques et le second exploite les données obtenues en utilisant des techniques d'identification des systèmes. La conception de commande est basée sur l'etude en dimension infinie en utilisant l'analyse de Lyapunov. Le contrôle composite est synthétisé en utilisant la théorie des perturbations singulières pour isoler la composante rapide de la composante lente. Tout le travail théorique est implémenté et testé dans des simulations basées sur la physique avancée en utilisant le simulateur de plasma pour les tokamaks DIII-D, ITER et TCV.

Mots clés : Plasmas Tokamak, Équation aux Dérivées Partielles, Contrôle des Plasmas, Modélisation, Fonction de Lyapunov, Perturbations singulières, Identification de système

---

Abstract — The objective of this thesis is to propose new methods for analysis and control of partial differential equations that describe the coupling between the transport models of the electron pressure (density multiplied by the temperature) and the magnetic flux in the tokamak plasma. The coupled system is presented by two 1D resistive diffusion equations. In this thesis two kinds of control models are obtained. The first is a first-principle driven model and the second one is the data-driven model obtained using system identification techniques. The control design is based on an infinite dimensional setting using Lyapunov analysis. Composite control is designed using singular perturbation theory to divide the fast from the slow component. All the theoretical work is implemented and benchmarked in advanced physics based on simulations using plasma simulator for DIII-D, ITER and TCV tokamaks.

Keywords: Tokamak Plasmas, Partial Differential Equations, Advanced Plasma Scenarios, Modeling, Lyapunov Control Functions, Singular Perturbations, System Identification

---

GIPSA-lab, 11 rue des Mathématiques, Grenoble Campus BP46, F-38402
Saint-Martin-d'Hères, FRANCE